



저작자표시-비영리-변경금지 2.0 대한민국

이용자는 아래의 조건을 따르는 경우에 한하여 자유롭게

- 이 저작물을 복제, 배포, 전송, 전시, 공연 및 방송할 수 있습니다.

다음과 같은 조건을 따라야 합니다:



저작자표시. 귀하는 원 저작자를 표시하여야 합니다.



비영리. 귀하는 이 저작물을 영리 목적으로 이용할 수 없습니다.



변경금지. 귀하는 이 저작물을 개작, 변형 또는 가공할 수 없습니다.

- 귀하는, 이 저작물의 재이용이나 배포의 경우, 이 저작물에 적용된 이용허락조건을 명확하게 나타내어야 합니다.
- 저작권자로부터 별도의 허가를 받으면 이러한 조건들은 적용되지 않습니다.

저작권법에 따른 이용자의 권리와 책임은 위의 내용에 의하여 영향을 받지 않습니다.

이것은 [이용허락규약\(Legal Code\)](#)을 이해하기 쉽게 요약한 것입니다.

[Disclaimer](#)



공학박사 학위논문

**Novel Soft Lithography Technologies
for Wearable Light Emitting Diodes
and Biosensors**

웨어러블 발광소자와 바이오 센서를 위한
새로운 소프트리소그래피 기술

2016년 8월

서울대학교 대학원

화학생물공학부

최문기

Abstract

Novel Soft Lithography Technologies for Wearable Light Emitting Diodes and Biosensors

Moon Kee Choi

Chemical and Biological Engineering

The Graduate School

Seoul National University

Soft electronic devices, in particular healthcare-related ones, have been intensively studied over the past decade due to their unique advantages in biomedical applications over the conventional rigid electronics, including conformal contacts on human skin and high deformability that minimizes unwanted inflammatory responses. To achieve the soft nature in high performance electronics and to apply this technology to wearable biomedical electronics/optoelectronics, several strategies have been employed, such as the designed assembly of high quality nanomaterials, combination of

unconventional manufacturing processes with existing microprocessing technologies, new design of individual devices with deformable structures, and disease-specific system-level integration of diverse soft electronics. Here, we describe 3 types of noble soft lithography technologies for the wearable electronic/optoelectronic devices.

First, alignment of red-green-blue micro pixels with high resolutions up to 2,460 pixels per inch was developed by intaglio transfer printing. This technique is readily scalable and adaptable for low voltage-driven pixelated white LEDs and ultrathin, wearable electronic tattoos, showing the best electroluminescence performance (14,000 cd m⁻² at 7 V) among the wearable light-emitting diodes reported up to date.

Second, a thermally controlled transfer printing method that is specially designed for the multiple aligned transfer of patterned graphene is developed. Through this approach, accurate and high-yield transfer printing of patterned graphene onto diverse substances is achieved, allowing a transparent, stretchable, and wearable all-graphene electronic/optoelectronic system to be fabricated.

Third, biomimetic miniaturized suction cups are designed for the patient-friendly, dry adhesives of smart medical skin. Both strong van der Waals

force and induced negative pressure by the ultrasoft mSCs facilitate tight skin coupling without discomfort or irritations, improve sensitivities of the embedded stretchable electronics for continuous vital sign monitoring, and enable multiple drug reloading without loss of the adhesion.

Keywords: Unconventional patterning, wearable devices, electronic/optoelectronic devices, flexible electronics, nanomaterial patterning.

Student Number: 2010-24105

Contents

Abstract

Chapter 1 Reviews on various assembly/patterning methods for nanomaterial assembled wearable electronics/optoelectronics 1

1.1 Assembly and Patterning for Wearable Devices	1
1.2 Various Assembly/Patterning Method.....	6
1.2.1 Langmuir-Blodgett Deposition	6
1.2.2 Doctor Blading.....	10
1.2.3 Nanoimprint Lithography	13
1.2.4 Screen Printing.....	15
1.2.5 Inkjet Printing	18
1.2.6 Micro-Contact Printing	22
1.3 Nanomaterial Assembled Electronics/Optoelectronics	26
1.3.1 Overview.....	26
1.3.2 Electrode/Conductor	28
1.3.3 Semiconductor Active Material	33

1.3.4	Transdermal Drug Carrier	38
1.3.5	Adhesive Patch.....	41
	References.....	43

Chapter 2 Wearable Red-Green-Blue Quantum Dot Light-Emitting Diode Array Using High Resolution Intaglio Transfer-Printing..... 49

2.1	Introduction	49
2.2	Experimental Section	52
2.3	Result and Discussion	66
2.4	Conclusion	90
	References.....	91

Chapter 3 Temperature controlled, patterned graphene transfer printing for transparent and wearable electronic/optoelectronic system..... 97

3.1	Introduction	97
3.2	Experimental Section	100
3.3	Result and Discussion	107
3.4	Conclusion	140

References	141
Chapter 4 Cephalopod-inspired Miniaturized Suction Cups for Smart Medical Skin	147
4.1 Introduction.....	147
4.2 Experimental Section	155
4.3 Result and Discussion	174
4.4 Conclusion	196
References.....	197
Bibliography	202
국문 초록 (Abstract in Korean)	209

List of Figures

Figure 1.1 Nanomaterials, assembly, deformable design, and device integration for wearable electronics/optoelectronics	5
Figure 1.2 Langmuir-Blodgett (LB) deposition	9
Figure 1.3 Doctor blading method	12
Figure 1.4 Nanoimprint lithography	14
Figure 1.5 Screen printing process.....	17
Figure 1.6 Inkjet printing process	21
Figure 1.7 Microcontact printing process	25
Figure 1.8 Components of the wearable electronics/optoelectronics which needs micro-/nano-patterning technique	27

Figure 1.9 Electrodes and conductors32

Figure 1.10 Semiconductor nanomembranes36

Figure 1.11 Colloidal nanomaterials and CNT for the active material of soft electronics.....37

Figure 1.12 Transdermal drug delivery system.....40

Figure 1.13 Adhesive patch42

Figure 2.1 Intaglio transfer-printing for high resolution RGB QLEDs.....70

Figure 2.2 The PL images showing aligned RGB pixels whose resolution is 2,460 pixels per inch (ppi).....71

Figure 2.3 Experimental and theoretical analysis of the intaglio transfer-printing72

Figure 2.4 Schematic illustration of the structured stamping method.....73

Figure 2.5 Circular pattern-size effect on the yield of transfer printing

QDs.....74

Figure 2.6 Finite-element method (FEM) simulations of the structured

stamping and intaglio printing method.....75

Figure 2.7 Intaglio transfer printing demonstrations of various QDs76

Figure 2.8 Effect of pattern spacing on the transfer-printing yield77

Figure 2.9 True white light emission based on pixelated RGB QLEDs81

Figure 2.10 Characteristics of CdSe-based R/G/B QDs82

Figure 2.11 FTIR characterization of CdSe/ZnS alloyed QDs83

Figure 2.12 UV photoelectron spectra of layer materials employed in

QLEDs.....84

Figure 2.13 Electronic tattoo demonstrations using ultrathin wearable

QLEDs.....	87
------------	----

Figure 2.14 Device characteristics of wearable electronic tattoo.....88

Figure 2.15 Ultrathin QLEDs on various curvilinear substrates.....89

Figure 3.1 Schematic illustrations of the wearable and transparent graphene electronic/optoelectronic system109

Figure 3.2 Schematic illustration of the thermally controlled transfer printing process112

Figure 3.3 Experimental evaluation of “heating and cooling” sequences..115

Figure 3.4 Large-area transfer printing of graphene patterns.....116

Figure 3.5 Graphene patterns transferred on the (a) hydrophilic and (b) superhydrophobic surface.....117

Figure 3.6 Simulation of the elastic and viscoelastic behaviors of PDMS, PIB,

and PET layers during the thermal treatment	122
Figure 3.7 Peel test of PIB/PDMS, PIB/PET interfaces	124
Figure 3.8 Electrical and optical properties of transferred graphene patterns	127
Figure 3.9 Large scale 2D Raman mapping analysis	128
Figure 3.10 Optic images of high resolution graphene patterns transferred by our thermally controlled transfer printing technique	129
Figure 3.11 Integrated wearable sensors and actuators	132
Figure 3.12 Optical camera image of a custom-made smart band which consists of a Bluetooth unit, power source (lithium-ion battery), and controller unit	133
Figure 3.13 Wearable QLED with the graphene anode	136

Figure 3.14 Feedback thermal and electrical actuators 139

Figure 4.1 Overview of the electronic patch with bio-inspired dry adhesives 150

Figure 4.2 Exploded view of mSC electronic patch 152

Figure 4.3 Deformable mSCs electronic patch 153

Figure 4.4 Smart band that consists of a Bluetooth unit, a battery, and a controller unit 154

Figure 4.5 Modeling of mSC structures 158

Figure 4.6 Animal scratching behavior test for the measuring of comfortness 161

Figure 4.7 Peel-off test of mSC patch 172

Figure 4.8 Schematic diagram for the fabrication of mSCs mold 175

Figure 4.9 Mechanical characteristics of gradual mSC structures176

Figure 4.10 Bio-inspired suction cups as comfortable dry adhesives180

Figure 4.11 Measurement of vital signs, detection of acute medical conditions,
and wireless communications.....188

Figure 4.12 Continuous monitoring of vital signs (e.g. heartbeat and body
temperature) in a mouse disease model of hypothermia induced
by ethanol tap and treated with warming.....190

Figure 4.13 Controlled transdermal drug delivery via iontophoresis.....194

Figure 4.14 Drug reloading procedure onto the electrode of the mSC
patch195

List of Table

Table 3.1 Young's modulus of PIB and PDMS123

Chapter 1. Reviews on various assembly/patterning methods for nanomaterial assembled wearable electronics/optoelectronics

1.1 Assembly and Patterning for Wearable Devices

Since the development of the field effect transistor in 1920s, the electronics industry has focused on the research of high speed and large capacity devices such as microprocessors and random access memory. However, the recent rise of personalized and mobile electronics changed this research trend from the performance-oriented research to human-friendly one. Therefore, flexible and stretchable electronics whose mechanical properties are similar with human tissues but performances are similar with conventional electronics have been highlighted. Amongst this change, nanomaterials-based electronics/optoelectronics have attracted huge attention because of its unique features such as the mechanical deformability and high performances.

These biomedical devices based on soft-electronics have been developed as a wearable form. Synthesized and/or processed nanomaterials are seamlessly integrated for the multi-functionality and/or enhanced performances of the soft electronic devices.

Various nanomaterials, from 0D nanocrystals to 2D nanomembranes, have been used in soft bio-electronics for improving device performances and mechanical deformability (Figure 1a). Nanomaterials have distinctive physical/chemical/electrical characteristics, superior to those of bulk materials: the quantum confinement effect of 0D quantum dots, superparamagnetic of magnetic NCs (Figure 1.1a; top left),^[1] unidirectional carrier transport of 1D nanowires (Figure 1.1a; top right),^[2] distinctive transparency and conductance of graphene (Figure 1.1a; bottom left),^[3] and mechanical flexibility of 2D silicon nanomembranes (Figure 1.1a; bottom right).^[4]

To achieve a high performance in arrayed nanomaterial-based soft electronics, a uniform and large-scale assembly of the nanomaterials is essential. Several assembly techniques such as spin casting, the Langmuir Blodgett (LB) method, mechanical molding, dry transfer printing, and lithography have been used to integrate the nanomaterials into soft-electronics (Figure 1.1b). The LB method is an easy process for manufacturing large-area, self-assembled monolayers of nanocrystals (Figure 1.1b; top left).^[5] Molding the composites of polymers and nanomaterial fillers by applying external heat/photon/pressure enables the fabrication of uniform and high aspect ratio micro-/nano-structures (Figure 1.1b; top right).^[6] The transfer printing technique is another powerful tool for assigning nanomaterials in a 2D plane of micro-/nano-configurations at

the desired locations. Additive transfer printing with a structured stamp is widely used for transferring 2D semiconductor nanomembranes (Figure 1.1b; bottom left).^[7,8] Meanwhile, the intaglio transfer printing can be utilized for transferring the assembled colloidal nanocrystal layer as a high resolution pattern (Figure 1.1b; bottom right).^[9]

Along with the intrinsic flexibility of the nanomaterials, advanced design strategies have been applied to increase the device deformability (Figure 1.1c). Decreasing the thickness of the electronics is important for enhancing the flexibility and for reducing the induced strain on the devices that is proportional to the system thickness and inversely proportional to the bending radius (Figure 1.1c; top left).^[10] Buckled structures can provide bendability and 1D stretchability following the wrinkled direction (Figure 1.1c; top right),^[11] and serpentine-structured interconnections can afford 2D large-scale deformations (Figure 1.1c; bottom left).^[12] In addition, the percolated structure of the 1D nanowires helps the composition of the stretchable electronic sheet to have uniform electrical/mechanical properties over the large area even under mechanical deformations (Figure 1.1c; bottom right).^[13]

The integration of the individual soft-electronics (i.e., sensors, actuators, memory, and display) is important for performing multifunctional tasks for the diagnosis and therapy of a specific disease. For instance,

graphene/Au mesh-based biosensors (i.e., the glucose, pH, humidity, and tremor sensor) and drug-loaded microneedles were assembled on a thin elastomer film for monitoring and treating diabetes (Figure 1.1d; top left).^[14] A conductive elastomer composited of Ag nanowires/styrene-butadiene-styrene (SBS) was used in treating the pain around the joints and for performing articular thermotherapy (Figure 1.1d; top right).^[2] Quantum dot based flexible transistor array can be utilized to the next-generation wearable electronics (Figure 1.1d; bottom left).^[15] Moreover, ultrathin epidermal polymer light emitting diodes (LEDs) were integrated with wearable electronics to serve as a visual display for healthcare-related data and as an user interface to medical devices (Figure 1.1d; bottom right).^[16]

In this chapter, various patterning methods for assembled nanomaterials are described. Moreover, diverse applications of assembled nanomaterials for wearable electronics/optoelectronics are discussed.

* Some contents of this chapter were published in **Advanced Materials** (2016, 28, 1176).

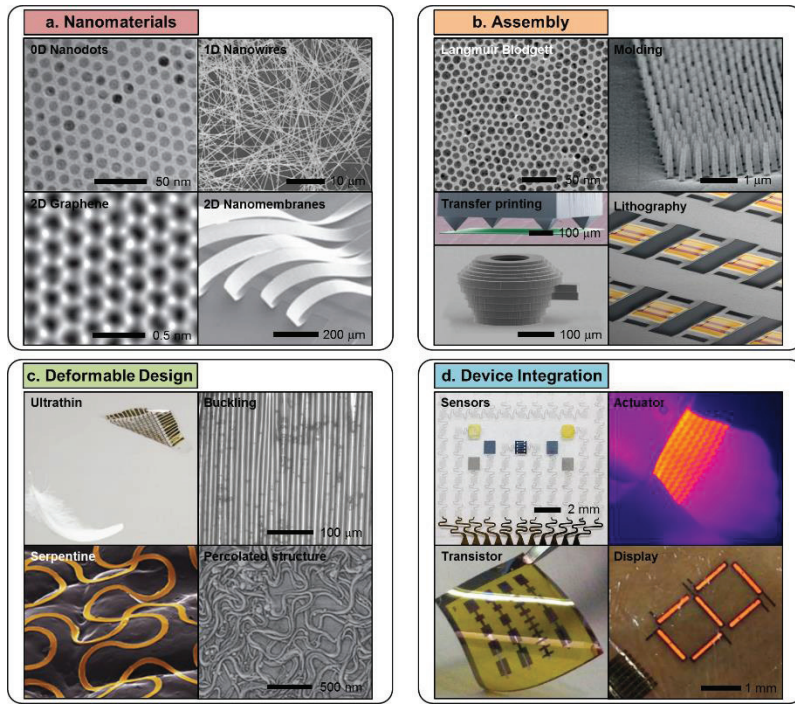


Figure 1.1. Nanomaterials, assembly, deformable design, and device integration for wearable electronics/optoelectronics. **(a)** Fe_3O_4 nanoparticles (0D, left top), Ag nanowires (1D, right top), graphene (2D, left bottom), and Si nanomembrane (2D, right bottom). **(b)** Diverse assembly methods. Langmuir-Blodgett assembly of nanoparticles (left top), molding of photo-curable polymer (right top), transfer printing of Si nanomembranes (left bottom), and lithography for integration of nanomembranes (right bottom). **(c)** Deformable design for flexible and stretchable soft-electronics. Ultrathin (left top), buckling (right top), serpentine (left bottom), and percolated (right bottom) structures improve the system-level deformability. **(d)** Diverse device integration. Sensors (pH, glucose, humidity, and tremor sensor; left top), actuator (heater, right top), transistor (left bottom), and display (polymer LED; right bottom).

1.2 Various Assembly/Patterning Method

1.2.1 Langmuir-Blodgett Deposition

Langmuir-Blodgett (LB) deposition, which was initially devised for amphiphilic organic molecules, is a powerful method for obtaining self-assembled monolayers of NCs or CNTs. NC films can be fabricated by the successive deposition of individual NC LB layers on a target substrate. The presence of organic ligands at the surfaces of the colloidal NCs makes them appropriate for the LB process.

Figure 1.2a shows the process of LB deposition. First, the NC layer is formed by spreading the NCs on a liquid surface. The surface pressure, which can be adjusted by moving one or two sliding barriers on the liquid surface, is one of the most important parameters in controlling the morphology of the final film. Figure 1.2b shows a typical surface pressure versus area isotherm (π - A) for zero-dimensional NCs.^[17] The NCs are very loosely packed initially (Region I). At a certain point, the surface pressure starts to rise more rapidly, indicating a phase transition and the formation of a complete monolayer (Region II, A_1). Further compression results in a small pressure increase (the plateau in Region III). This indicates the collapse of the monolayer and formation of a double layer (Region IV, $A_1/2$). A similar isotherm and phase transition are observed again for the formation of the triple layer (Region V,

$A_1/3$). After the formation of NC layers with the desired packing density and thickness, they can be transferred to a target substrate through a vertical dipping-pulling process. Sometimes, the NC layer is transferred through a horizontal contacting/lifting process, known as the Langmuir-Schaefer technique.

To obtain a uniform NC layer and control the packing density (or coverage), the surface pressure must be precisely controlled by installments, LB trough (Figure 1.2c). Many groups have successfully applied this technique to generate NC films of various materials and shapes such as nanodots,^[18] nanocubes,^[19] nanorods,^[20] and NWs (Figure 1.2d,e).^[21] Further delicate control can be achieved by incorporating charged molecules, such as DNA.^[22] Sometimes, NCs can be synthesized *in situ* on ligand films deposited by the LB process. Precursors can be selectively attached to a surfactant layer at the air/water interface, and converted into NCs upon the subsequent exposure to reaction gases.

There are several limitations of the LB technique. The NCs and substrates need to be typically exposed to the water, because the assembly process is usually conducted at a water/air interface. This can cause serious problems, particularly in moisture-sensitive materials. Many materials (*e.g.*, conductive polymers and organic molecules) employed in NC-based devices as

well as NCs themselves are easily damaged by the water. Another limitation is the difficulty of the large-scale production due to narrow and sensitive processing conditions associated with ultrathin LB films floating on liquids.

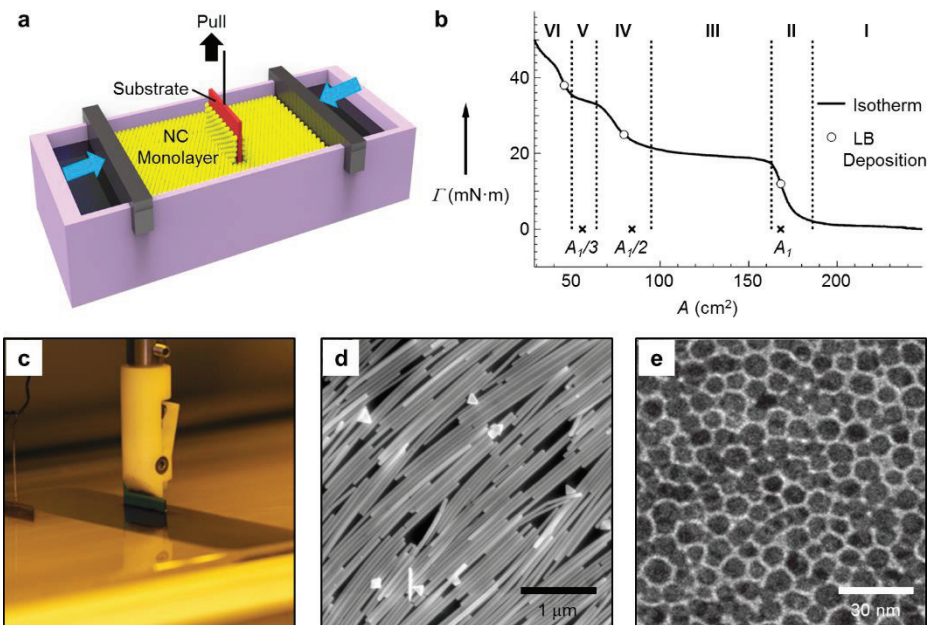


Figure 1.2. Langmuir-Blodgett (LB) deposition. **(a)** A schematic showing the LB deposition process. An LB monolayer of NCs is coated on the substrate at the water/air interface. **(b)** A typical pressure-area isotherm of CdSe QDs spread on a water surface. Various regions (I, II, III, *etc.*) show different phase stages. A_1 represents the area in which the initial full monolayer forms. **(c)** A photograph showing the LB trough. **(d)** A scanning electron microscopy image of monolayer silver NWs acquired by LB deposition. **(e)** A transmission electron microscopy image of monolayer gold NPs acquired by the LB deposition.

1.2.2 Doctor Blading

Doctor blading is a representative film fabrication method for NC films in a relatively thick thickness range (**Figure 1.3a**). A sharp plate (or a blade) moves over the NC solution on a substrate, which leaves a NC film of uniform thickness. The final thickness of the NC film is determined by the gap between the blade and the substrate. The shape of the meniscus between the blade and the coating solution affects the morphology of the film. The final thickness of the film, d , is expressed by **Equation 1**:^[23]

$$d = \frac{1}{2} \left(g \frac{c}{\rho} \right) \quad (1)$$

where g is the gap between the blade and the substrate, c is the concentration of NCs in the solution (g cm^{-3}), and ρ is the density of the material (g cm^{-3}).

As shown in Figure 1.3b, doctor blading produces relatively thick NC films (up to several μm).^[24] For example, the process has been employed to obtain several- μm -thick TiO_2 NC layers in dye- or QD-sensitized solar cells, or electrodes made by conducting NCs (Figure 1.3c).^[25] Another benefit of the doctor blading is its compatibility with roll-to-roll processes. One example is the knife-over-edge coating method, which is similar to the normal doctor blading except the fact that the position of the blade is fixed while the substrate moves (Figure 1.3d). One limitation of the doctor blading is that it cannot produce an ultrathin NC film with only a few NC layers (*i.e.*, ultrathin

thickness), since the thickness of the NC film is determined by the physical gap between the blade and the substrate that cannot be precisely controlled at the nanometer scale. Furthermore, NCs sometimes can be inhomogeneously aggregated or crystallized during the process, since a slow evaporation of the solvent takes place after the blading.

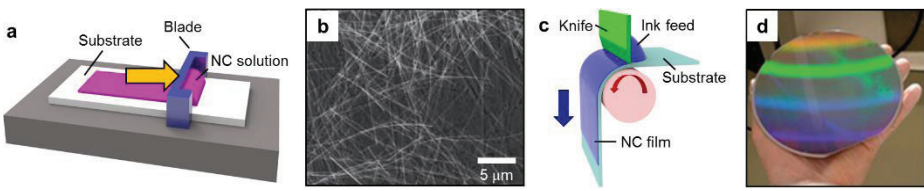


Figure 1.3. Doctor blading method. **(a)** A schematic illustrating the doctor blading process. **(b)** A photograph showing a SiO₂ NC layer coated on a Si wafer by the doctor-blading method. **(c)** A scanning electron microscopy image of Ag NW network on brass. **(d)** A schematic illustration showing the knife-over-edge process, which is a modified version of doctor blading that is compatible with the roll-to-roll process.

1.2.3 Nanoimprint Lithography

Nanoimprint lithography (NIL) is widely utilized method for the low cost, large area micro/nano patterning. NIL is categorized to two groups: thermal NIL and UV NIL (**Figure 1.4a and b**). Stamp acts as mask pattern in photolithography that has embossed designed patterns. In thermal NIL, the resist coated substrate is contacted with nano-patterned stamp and the high temperature (above the transition temperature of resist) and pressure is applied to mold the resist. To supplement the disadvantages of thermal NIL (i.e. thermal expansion of stamp/substrate and fracture due to high applied pressure), UV NIL is introduced which utilizes UV light instead of heat and pressure to cure the resist. As UV radiation rapidly cures the UV curable resin in arbitrary temperature, UV NIL is efficient in multi-stacking process. For instance, K. Y. Suh group demonstrated unique micro/nano hierarchical structures for the dry adhesives. Figure 1.4c shows stooped nanohairs which are manufactured by UV NIL and e-beam radiation.^[26] This nanostructures enormously increased surface area which dramatically increase the adhesion force (1 kg/cm^2). Figure 1.4d demonstrated hierarchical structured dry adhesive.^[27] The slanted nanostructures are stacked on the partially cured micropillar to mimic the Gecko's foot.

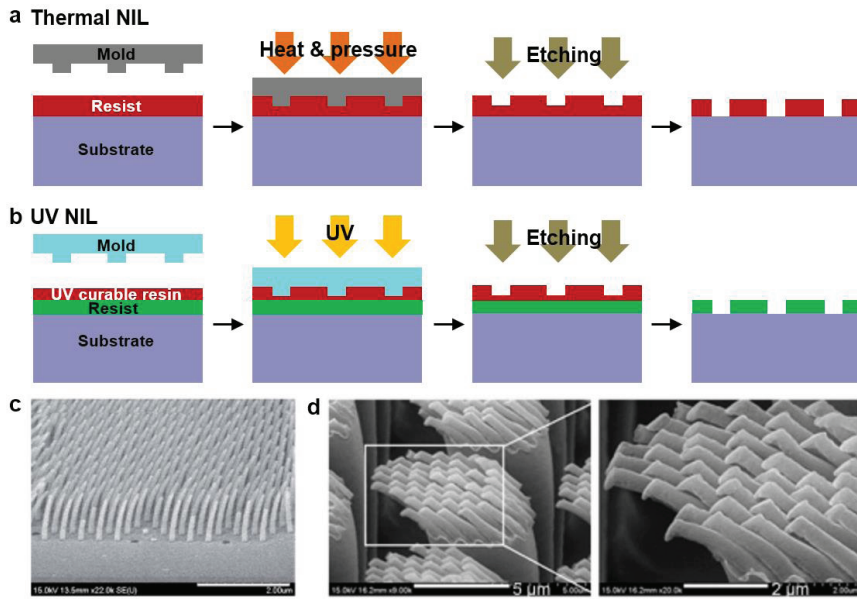


Figure 1.4. Nanoimprint Lithography. (a, b) Schematic illustration of thermal NIL (nanoimprint lithography) (a), and UV NIL (b). (c) Gecko-foot like stooped nanohairs made by UV curable polymer. (d) A SEM image of micro-/nano-hierarchical polymer nanohairs.

1.2.4 Screen Printing

Screen printing is a very simple but fast and efficient patterning technique that has been successfully applied to colloidal NCs (**Figure 1.5a**). It can produce a large number of nearly identical patterns in a single printing step under ambient conditions at low cost. In some aspects, the process is similar to the doctor blading except that a patterned screen is introduced. The ink penetrates the open windows/patterns of the screen and is laminated on the target substrate. To prevent any leakages crossing the designed pattern, the ink for the screen printing must have a certain viscosity. Polymers such as poly(methylmethacrylate) are often used as binders with the NCs in the ink to better adhere them with each other and to the substrate.^[28] For the screen printing, the film thickness is expressed by **Equation 2**:

$$d = k_d \left(\frac{V}{A} \right) \left(\frac{c}{\rho} \right) \quad (2)$$

where k_d is the deposition yield, V is the volume of the solution (cm³), A is the open area of the screen (cm²), c is the concentration of the NCs in the solution (g cm⁻³), and ρ is the density of the material in the NC film (g cm⁻³). The deposition yield (k_d) is affected by many factors, including the distance, the speed of the blade, the viscosity of the solution, and the force against the screen.

The advantages and limitations of the screen printing are similar to those

of the doctor blading. The screen printing is economical and compatible with roll-to-roll processes. For example, roll-to-roll rotary screen printing has been developed. Due to the requirement for relatively high viscosity of the inks, the films are generally thick (> hundreds of nanometers). Thus, the technique is suitable for making interconnections or electrodes based on conducting metal NCs^[29,30] (Figure 1.5b) and thick TiO₂ NC layers in the electronic circuits and the dye-sensitized solar cells, respectively. Sometimes, binders, usually organic materials, cause the increase of resistance and should be treated properly. The resolution of the final pattern is determined by that of the screen.

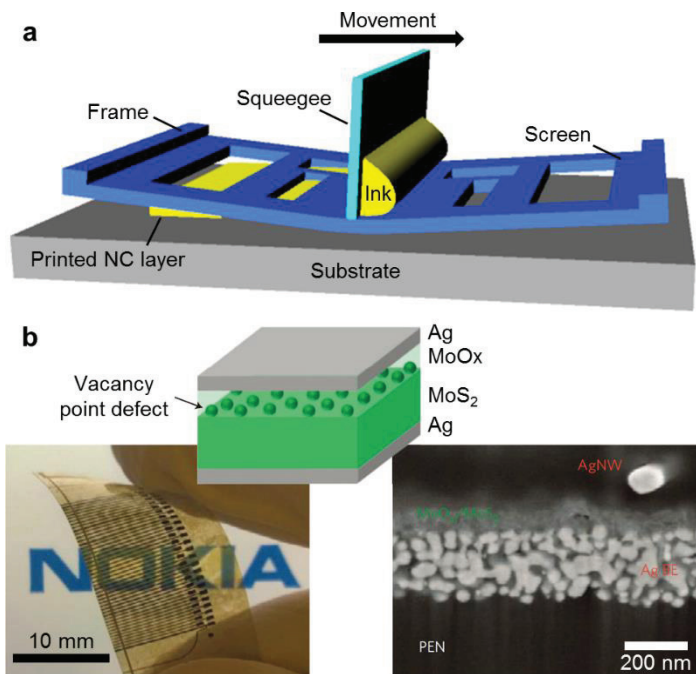


Figure 1.5. Screen printing process. (a) A schematic illustrating the screen printing process. The screen is used to obtain patterns. (b) Solution-processed $\text{MoO}_x/\text{MoS}_2$ memristors on a plastic foil. The bottom and top electrodes were fabricated, respectively, by inkjet printing and screen printing of silver NP ink on a poly(ethylene naphthalate) (PEN) foil. The MoS_2 film was deposited by a spreading technique. The right picture shows a photograph of a cross-point memristor array on PEN with high visual transparency. The left image shows the cross-sectional scanning electron microscopy image of the Ag NWs/ $\text{MoO}_x/\text{MoS}_2$ switching device.

1.2.5 Inkjet Printing

Inkjet printing is an attractive technique for the microscale patterning of various materials. A schematic inkjet printing procedure is shown in **Figure 1.6a**. The ink (homogeneously dispersed NCs in a solvent) is ejected as tiny droplets (with micrometer-scale diameters) by an applied electric field and backside pressure and is directly deposited at the desired substrate locations. This is the most economical printing method among the various NC patterning processes due to its minimal material loss. Because inkjet printing is a non-contact technique, NC inks can be deposited on diverse substrates such as polymers, metals, oxides, and biomaterials. Additional benefits of inkjet printing are that patterns can be easily changed and that printing over large areas is relatively easy.

The use of colloidal NCs as suspensions overcomes the solubility limitations of the inks, leading to more stable printing. However, suspension-based inks have short shelf-lives due to their easy precipitation or aggregation. Moreover, if the ink volatility and viscosity are not precisely controlled, “coffee-fringe” or central “mountaintop” effects tend to form non-flat films due to capillary or Marangoni flows during the drying of the inks. Coffee-fringe edges often appear when NCs accumulate at the rim of the drying droplet due to the inhomogeneous evaporation of the solvent (Figure 1.6b).^[31] This uneven

morphology leads to electrical defects.

To overcome these issues, the evaporation rate has been controlled by introducing additives having the high boiling point and low surface tension. The mixed solvents (original solvent and additive agent) afford a gradient of the surface tension during drying (Marangoni flow). The main solvent, having a lower boiling point and higher surface tension, preferentially evaporates at the contact line, resulting in an outward flow. On the other hand, the Marangoni flow developed by the solvent gradient retards the outward flow. These cause the formation of a surface tension gradient over the whole droplet during drying, which develops an inward flow. The outward and inward flows consecutively circulate the NCs suspended in the ink and lead to a uniform thickness film. Figure 1.6c presents the uniform surface profile of Al₂O₃ NCs resulting from the use of a co-solvent ink.^[32]

Inkjet printing is easily applied to the fabrication of various kinds of devices, such as LEDs, solar cells, and field-effect transistors (FETs), as well as in the formation of interconnections in electronic circuits. Figure 1.6d and e shows the photoluminescence (PL) images of line^[33] and areal patterns of QDs. These QD patterns can be utilized to fabricate QLEDs. One advantage of this technique is the capability of multiple printings, which can be exploited to print multicolor LEDs in 3D configurations. For example, Figure 1.6f shows a

representative 3D pattern produced by stacking multiple ink patterns.^[34] The height of each patterned structure is proportional to the number of stacked layers. Stretchable electrodes can be patterned by printing a mixture of elastomer and conducting NCs.^[35] Vertically wrinkled, inkjet-printed stretchable interconnections are shown in Figure 1.6g. Inkjet printing allows the formation of stacks of elastomeric inks in a single step without any complex patterning procedures. The substrates are not limited to flat surfaces. By controlling the ink density and solvent volatility, omnidirectional printing can be introduced to realize 3D electrical structures.^[36] Figure 1.6h presents antenna patterns that were inkjet-printed onto the spherical surface of a glass bowl. The metallic Ag NC inks were conformally laminated onto the curvilinear surface to create the conductive lines of the antenna. Figure 1.6i presents the scanned pattern of the antenna obtained by optical profilometry, and the inset shows the scanning electron microscopy (SEM) image. The 20 μm -thick conductive lines with 100 μm widths were successfully formed on the concave structure.

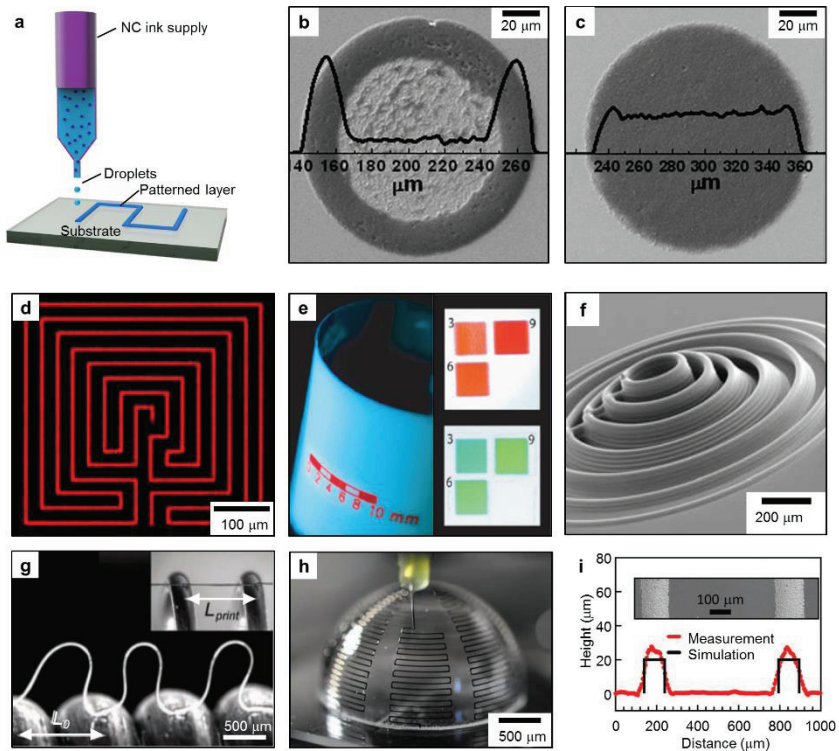


Figure 1.6. Inkjet printing process. (a) A schematic depicting the inkjet printing process. (b,c) SEM images and thickness profiles of Al₂O₃ NP ink patterns. A water single-solvent ink results in a pattern of inhomogeneous thickness (b) whereas a DMF/water co-solvent ink results in a pattern of uniform thickness (c). (d) A fluorescence image of the line pattern acquired by the inkjet printing of CdSe/CdS/ZnS red QDs in dichlorobenzene. (e) A photograph of QLEDs on a flexible substrate under illumination (365 nm). The pattern was inkjet-printed with a red QDs–polyisobutylene composite solution. (f) SEM image of silver microelectrodes patterned with 30 μm nozzles using silver NP ink. (g) An optical image of stretchable silver arches inkjet-printed onto a spring. (h) A photograph of the antenna during printing *via* a silver meander line. The conformal printing of silver NP inks on the curvilinear surface created conductive meander lines. (i) Thickness profiles of the meander lines shown in (h) determined by optical profilometry.

1.2.6 Micro-Contact Printing

Contact printing is a powerful method for the transfer of NCs in micro-/nano-configurations using stamps at desired locations. Soft, elastomeric polymers are utilized as stamps to pick up and place the NC “ink” on the target substrate. This room-temperature, low-cost procedure is simple yet powerful due to the versatile processability of various NCs on different kinds of target substrates. Contact printing techniques are categorized into two types: additive transfer and subtractive transfer (**Figure 1.7a and b**).

In additive transfer printing, the NC layer is directly coated on an elastomeric stamp using spin casting or spray-coating techniques. To transfer this coated “ink” onto the target substrate, the relationship between the surface energies of the receiving substrate and PDMS stamp must meet certain conditions. If the surface energy of the PDMS stamp ($19.8 \text{ mJ}\cdot\text{m}^{-2}$) is substantially lower than that of the target substrate (*e.g.*, $>200 \text{ mJ}\cdot\text{m}^{-2}$ for glass and silicon), the NC layer is easily transferred from the stamp to the target. In additive transfer printing, therefore, the quality of the inking process determines the quality of the resulting pattern.

Conventionally, the NC layer is spin-casted on the PDMS stamp. However, due to the possibly poor chemical compatibility between the elastomeric stamp and the organic solvent of the NC solution, the types of

solvents are limited, and it is difficult to obtain an evenly coated NC layer. Applying an ultrathin coating on the surface of the PDMS partially solves this problem. Coating layers include parylene, SU-8, and self-assembled monolayers, which change the surface energy as well as increase the chemical compatibility of the stamps. For example, coating with Parylene-C, which contains aromatic groups, decreases the surface energy difference between the QD monolayer and the stamp.^[37] Consequently, the contact angle between the PDMS stamp and a QD solution in chloroform decreases from 28° to 6°. This modified surface energy facilitates the wetting of the QD layer on the stamp as well as its release from the stamp. Figure 1.7c shows the image of two different QD layers cross-transferred using this additive transfer printing technique.

Another contact printing method is the subtractive transfer printing. Figure 1.7d presents the cross-sectional TEM image of the transfer printed QD monolayer. As shown in Figure 1.7b, the subtractive transfer printing process consists of two steps in which the NC layer is picked up from the donor substrate and released from the elastomeric stamp. In contrast to the additive transfer, NCs are inked on the stamp by picking up the NC layer from a donor substrate. Therefore, the surface energy of the donor substrate must be similar to or lower than that of the stamp. The surface energy of a silicon wafer as the donor substrate can be lowered by coating it with a self-assembled monolayer

of octadecyltrichlorosiloxane (ODTS).^[38] The wetting of the QDs on the donor substrate is also promoted by the aliphatic ligands of ODTs. As the surface energy of the donor substrate is similar to that of the elastomer stamp, dynamic parameters such as the retrieval rate and time-dependent application of pressure must be controlled to maximize the transfer printing yield. Figure 1.7e shows the relationship between the pick-up rate and the resulting yield. The separation energy at the QD/stamp interface, $G^{\text{QD/stamp}}$, depends strongly on the peeling rate, as described in **Equation 3**:

$$G^{\text{QD/Stamp}} = G^{\text{QD/donor substrate}}[1 + \phi(v)] \quad (3)$$

where ϕ is a function of the velocity (v) and $G^{\text{QD/donor substrate}}$ is the separation energy at the interface of the QD and donor substrate. The graph shows that nearly perfect transfer of the QDs (over 90%) can be achieved at the critical peeling rate, for instance, of 60 mm s^{-1} , with an applied pressure of 196 kPa, or 80 mm s^{-1} at 98 kPa (Figure 1.7e). The QDs are quickly picked up by the stamp and slowly released on the target substrate. This technique has been used to fabricate red, green, and blue (RGB) pixelated active-matrix QLEDs. Tightly packed, subtractively transferred, and defect-free QD layers lead to QLEDs with more efficient electroluminescence (EL) properties than those fabricated by the spin coating process (Figure 1.7f).

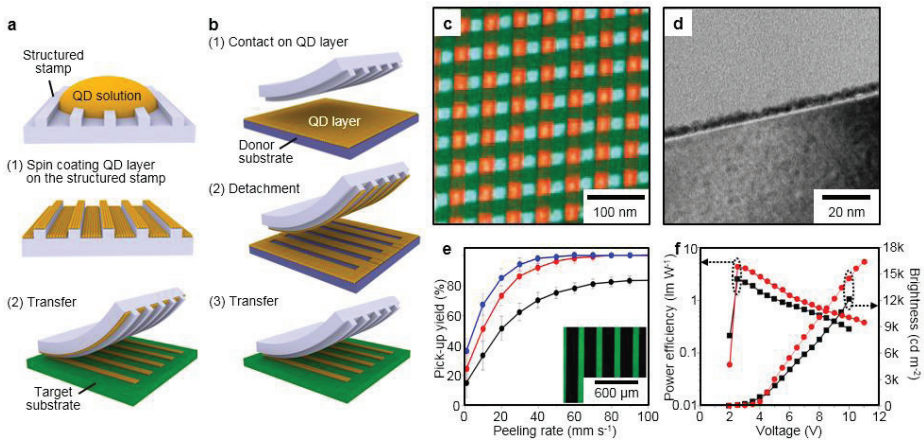


Figure 1.7. Microcontact printing process. (a) Schematic showing the additive transfer printing method. Colloidal NCs are directly coated on the patterned stamp and then transferred onto the final substrate. (b) Schematic showing the subtractive transfer printing method. Some part of the coated NC film is selectively detached by the structured stamp. The detached part is transferred onto the final substrate. (c) EL of QLEDs with an emissive layer consisting of 25 μm wide lines of green and red QD monolayers at an applied bias of 7 V. QD layers are subtractive transfer printed. (d) A cross-sectional TEM image of a QD monolayer on a Si substrate. (e) Pick-up yield of QD layers according to the peeling velocity during lift-off of the stamp in the subtractive transfer process. (f) Comparisons of the luminous efficiency and brightness versus voltage characteristics of QLEDs fabricated by the subtractive transfer printing (red circles) and the spin coating (black squares) of red QDs.

1.3. Nanomaterial Assembled Electronics/Optoelectronics

1.3.1 Overview

By virtue of the various coating and printing methods highlighted in this chapter, diverse nanomaterials ranging from metal NWs to QDs have been prepared and used in electronic and optoelectronic devices. Nanomaterials serve diverse roles in these devices: as conducting layers or electrodes, semiconducting channels, electron- or hole-transporting layers, and light-emitting or light absorbing layers. They can be categorized into four different groups: 1) electrodes/conductor, 2) active material of electronics, 3) transdermal drug carrier, and 4) adhesive patch. Synthesized and/or processed nanomaterials are seamlessly integrated for the multi-functionality and/or enhanced performances of the soft electronic devices in each group. In this section, specific applications of the assembled NCs for various electronic devices are reviewed.

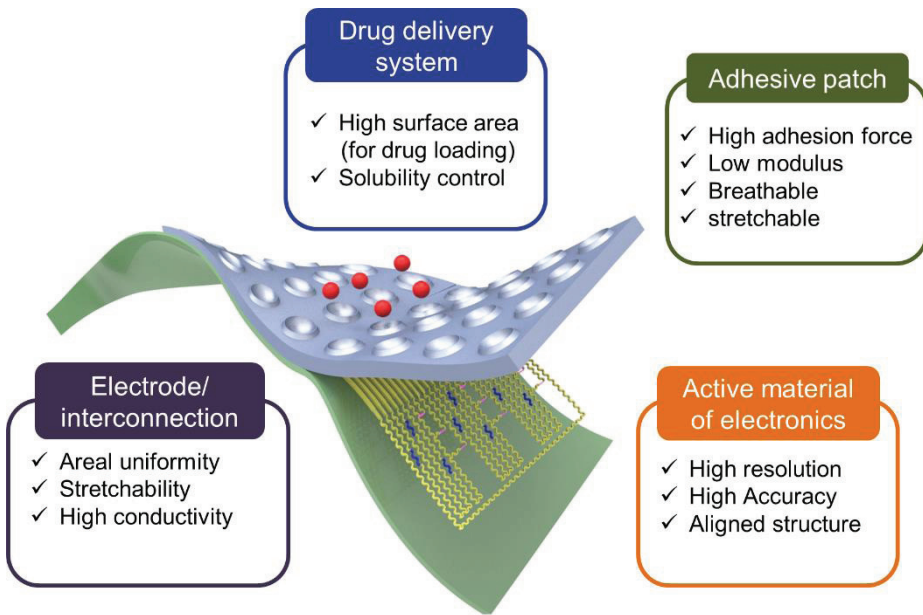


Figure 1.8. Components of the wearable electronics/optoelectronics which needs micro-/nano-patterning technique.

1.3.2 Electrode/Conductor

Colloidal metallic NCs have been widely employed to make transparent electrodes, typically in the form of metal NPs dispersed in the ink. Solution processes using the NC solutions have advantages over conventional vacuum evaporation processes, such as low equipment and processing costs, mild operating conditions, and compatibility with large-area electronics. In many optoelectronic devices such as LEDs, solar cells, and photodetectors, a transparent electrode through which photons can pass without the absorption, scattering, and/or reflection is an important component. Various nanomaterials have been investigated as promising alternatives to the foregoing conventional electrodes. ITO NCs, Ag NPs, and Ag NWs are good examples. In particular, highly percolated Ag NW networks, which exhibit high transparency (~ 90%) and low resistance (~ $10 \Omega \text{ sq}^{-1}$), are close to be commercially applied in displays, touch panels, and solar cells.

To prepare transparent conducting films of Ag NWs, various processes have been used, including spin coating, spray printing, blading with a Mayer rod, or transfer printing with stamps. The thickness of the NW films is usually limited to less than ~100 nm to guarantee sufficient light penetration. One disadvantage of conventional NW networks is the disconnection of junctions between the NWs that occurs under repetitive applied strains. The Cui group

reported large-scale transparent electrodes with Au-bridged Ag NWs (**Figure 1.9a**).^[39] Doctor blading of a Ag NW solution with a Mayer rod generated high quality electrodes that showed stable bending characteristics, which could be scaled up for a continuous roll-to-roll process (Figure 1.9b). To form robust inter-wire junctions, the Ag NW film was alloyed with Au through the galvanic replacement reaction of Ag by Au. The Au alloy effectively bridged the Ag NWs at their junctions (Figure 1.9c).

Hybrid Ag NW structures that form strong NW junctions with various organic/inorganic/carbon materials can further enhance the flexibility, conductivity, and processability of Ag NW films. For example, micro-Ag flakes have been mixed with Ag NWs to improve the conductivity and graphene flakes were introduced to connect the junctions. Park *et al.* suggested a graphene-metal NW hybrid structure for transparent and stretchable electrodes (Figure 1.9d).^[40] High density Ag NWs were sandwiched between graphene layers. This hybrid electrode exhibited synergetic performance enhancement in terms of the mechanical flexibility, high conductivity, and uniform resistance. The graphene films also prevented the oxidation of the Ag NWs. The resulting hybrid electrode together with inorganic LEDs on a contact lens was turned on a rabbit's eye (Figure 1.9e,f).

Another important fabrication process is the inkjet printing using

conductive inks that are usually composed of concentrated Ag NCs solutions. By controlling the type and ratio of the NCs, surfactants, stabilizers, and solvents, various patterns with controlled electrical properties could be formed on different substrates. Krebs *et al.* reported transparent Ag grid electrodes using the roll-to-roll printing of Ag NC inks. This pattern is potentially applicable to touch sensors. The same NC ink can be applied to fabricate interconnections in unconventional macroelectronics. The NC inks can be printed on substrates with various surface energies from hydrophilic to superhydrophobic, curvilinear surfaces^[37] with concave to convex structures, and 3D structured surfaces.^[41] The interconnecting electrodes were demonstrated for antennas on 3D bowl structures, as described above, and as 3D interconnections for electronic circuits.

In addition, graphene is attracted as next-generation transparent electrode. Due to the intrinsic ultrathin, ultralight characteristics, the graphene layer is widely employed to the wearable and deformable electronic/optoelectronic systems. To transfer graphene interconnections onto the desired substrate, various transfer techniques are demonstrated. Figure 1.9g shows the patterned graphene transfer using elastomeric stamp.^[42] B. Hong group suggests new method to transfer large area patterned graphene layer utilizing roll-to-roll technique (Figure 1.9h).^[43] By using this method,

continuous fabrication of graphene interconnection can be obtained which is essential for the mass production. Figure 1.9i present graphene based transparent wearable electronics.^[44] Ag nanowire combined graphene layer acts as transparent electrode and graphene sandwiched with pressure sensitive polymer performs as strain gauge.

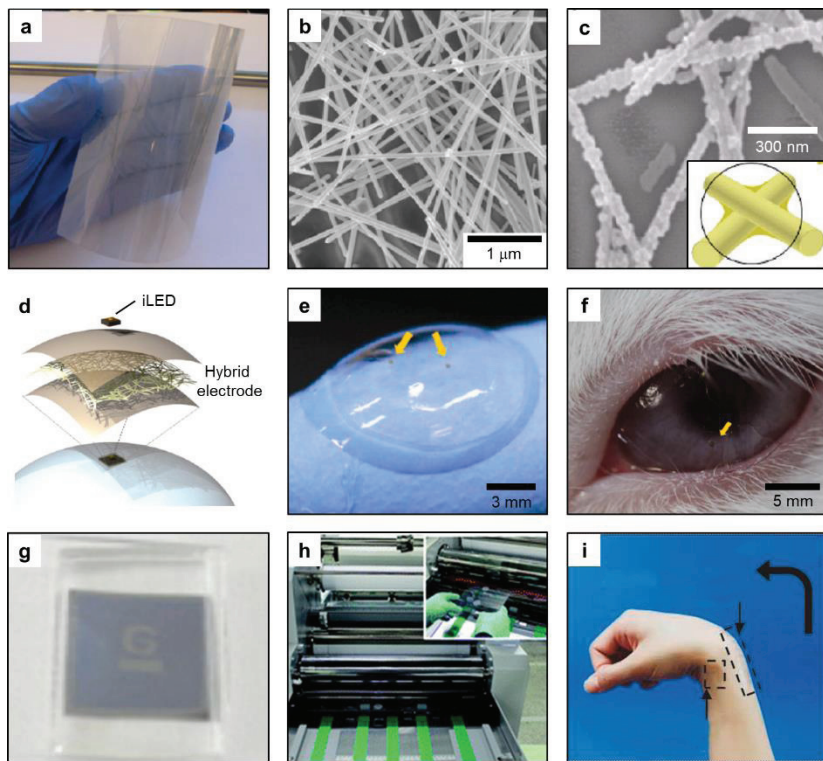


Figure 1.9. Electrodes and conductors. (a) A photograph showing an Ag NW film uniformly coated on a PET substrate. (b) A SEM image of the Ag NW film shown in panel (a). The sheet resistance of the film is $50 \Omega \text{ sq}^{-1}$. (c) A SEM image of the Ag NW film after formation of an Au–Ag alloy network by galvanic displacement reaction. The inset is a schematic of the Au–Ag alloy network. (d) A schematic illustration of a single-pixel contact lens display employing an inorganic LED and an Ag NW/graphene hybrid electrode. (e) A photograph of the contact lens device described in panel (d). (f) A photograph of the contact lens device on the eye of a rabbit. (g) Patterned graphene transfer using PDMS stamp. (h) A roll-to-roll process of continuous patterned graphene transfer printing. (i) Transparent graphene electronics for human-machine interface.

1.3.3 Semiconductor Active Materials

Diverse semiconductor nanomaterials are employed to the active materials of flexible/stretchable electronics. To assemble the nanomaterials into the soft-electronic devices, various patterning techniques are introduced.

2D semiconductor nanomembranes are widely utilized to the flexible/stretchable electronics. By reducing thickness of the bulk materials to the nanometer scale, the electronic characteristics of the Si nanomembranes remain the original characteristics of Si wafer and mechanical flexibility is enormously enhanced. **Figure 1.10a** shows the Si nanomembrane based pressure sensor.^[45] This ultrathin Si nanomembrane endure over the 20% external strain, and can be applied as artificial skin (Figure 1.10b). Inorganic LEDs are fabricated with GaAs, GaP nanomembranes. By stacking these units with the Co coils and NFC die, sticker type wearable LEDs were demonstrated which operated by wireless power supply (Figure 1.10 c and d).^[46] Moreover, the commercial ultrathin electronic kits can be integrated on the wearable electronics. J. A. Rogers group presented wirelessly communicated film type epidermal NFC electronics (Figure 1.10e).^[47] By combining serpentine-like structured coils, the epidermal electronics tightly attached on the skin without delamination even under compressive, stretched deformation (Figure 1.10f).

NC-based memory devices have received a great attention as next-

generation non-volatile memories due to their scalability, small size, reliability, and high write/read/erase speeds. Various NCs of metals, semiconductors, and oxides have been proposed as charge-trap sites in the floating gates of flash memories and as switchable resistive materials in resistive random-access memories. To fabricate high performance memory devices, NCs can be carefully assembled by various processes. Spin casting is widely used to fabricate NC films, but it is difficult to precisely control the NC thickness and orientation. LB techniques are widely used to produce self-assembled high density NC monolayers.^[48] For instance, metallic colloidal nanoparticles are inserted between TiO₂ nanomembranes to fabricate high performance resistive random access memory (**Figure 1.11 a-c**).

QD films have been employed as emissive electroluminescent layers in QLEDs. The applications of QLEDs can be classified into two major categories: white QLEDs for the backlight or the lighting devices and multicolor QLEDs for full color displays. Recently, deformable multicolor QLED arrays have received tremendous attention for next-generation displays. Microcontact printing is a powerful tool for realizing coplanar RGB QD patterns. Samsung manufactured an active matrix, full-color QD display on a flexible substrate (Figure 1.11 d-f).^[38] To realize multi-color displays, RGB QDs were spatially patterned using a structured elastomer stamp. Figure 1.11e shows the EL image

of a 4-inch QLED with a 320×240 pixel array.

Moreover, carbon nanotubes (CNTs) have been utilized to the organic semiconductor matters for electronics or pressure sensitive rubber combined with elastomer layer. Figure 1.11g shows SEM image of the spray coated CNT film.^[49] As CNTs have unique optical/electrical properties and mechanical deformability, the CNT based devices are suitable for the flexible/stretchable applications (Figure 1.11h). Figure 1.11i shows an out current diagram from CNT based flexible pressure sensor.

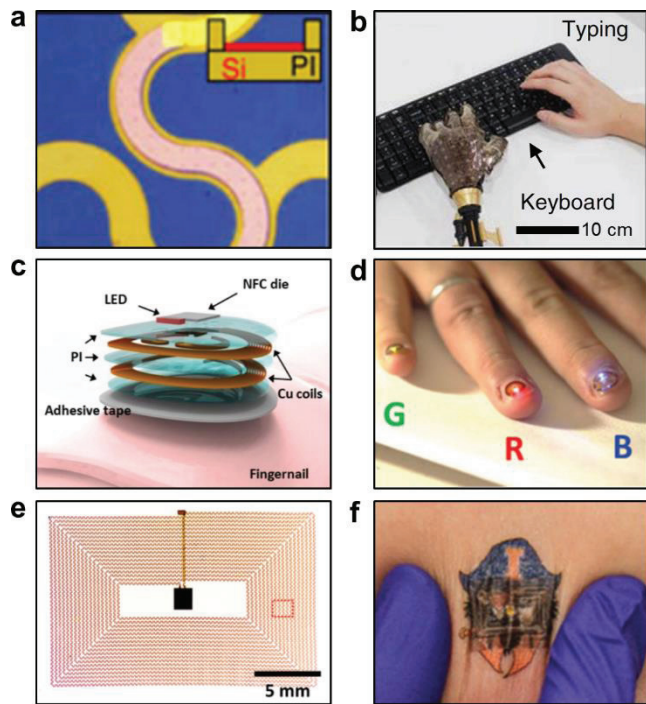


Figure 1.10. Semiconductor nanomembranes. (a) Optic image of the Si pressure sensor. (b) Demonstration of pressure sensor to the artificial skin. (c) Exploded scheme of the wireless, NFC capable electronic system on fingernail. (d) Image of LED integrated wireless system laminated on the fingernail. (e) Optic image of the NFC devices. (f) Deformed epidermal NFC electronics.

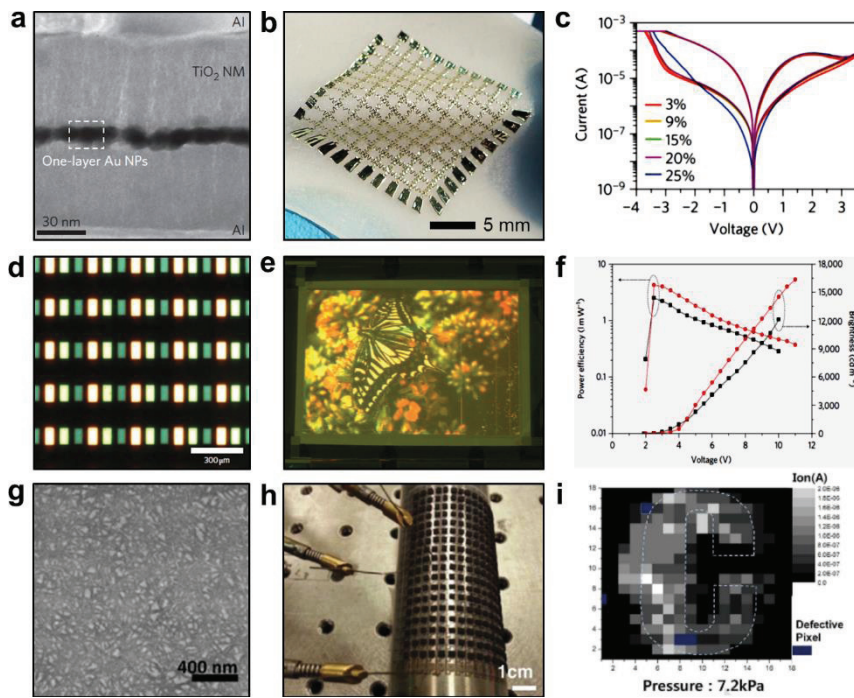


Figure 1.11. Colloidal nanomaterials and CNT for the active material of soft electronics. (a) Cross-sectional TEM image of the RRAM with Au nanoparticle layer. (b) Optic image of the deformable RRAM array on the commercial patch. (c) I-V characteristics of the deformable RRAM under different strains. (d) EL image of the transferred RGB QD layers. (e) Optic image of the full color QD display. (f) Power efficiency and brightness curve of QLED under various applied voltage. (g) SEM image of the deposited SWCNTs on the PET substrate. (h) Optic image of the flexible CNT TFTs. (i) Output currents diagram under 7.2 kPa applied pressure.

1.3.4 Transdermal Drug Carrier

Recently, transdermal drug delivery system is introduced with wearable electronic/optoelectronics to facilitate feedback diagnostic and therapeutic system. By analyzing the monitored bio-signs from the electronic sensors, the corresponding feedback therapy will transdermally proceed at optimum stimulus through actuating devices. Microneedles were conventional utilized to penetrate the epidermis and to deliver the drugs into the skin. Generally, microneedles are manufactured by soft lithography techniques. The drugs are encapsulated in the microneedle by water soluble polymer to protect from the oxidation and contamination. **Figure 1.12a** shows swellable microneedles, which is coated with hydrating polymer.^[50] This polymer swelled inside of the epidermis by absorbing intercellular matrix, and forked the skin tightly. The swellable microneedles achieved the 3.5-fold higher adhesion than staple fixation. Microneedles coated with thermo-responsive polymer can control the drug delivery rate by thermal actuator (Figure 1.12b).^[14] By heating the microneedle, encapsulating polymer swelled and transdermally released the drugs into the skin.

Another approach is transdermal drug delivery with porous nanoparticles. The mesoporous silica (m-silica) have massive pores inside of the nanoparticle, which can be container of the drugs. The drug-loaded m-silica

was patterned transfer on the hydrocolloide patch using structured stamp (Figure 1.12c).^[48] On the backside of the patch, thermal actuator made by thin Au metal line is located. By control the thermal actuation time and temperature, the drug inside of the m-silica was controlled released into the pig skin (Figure 1.12d).

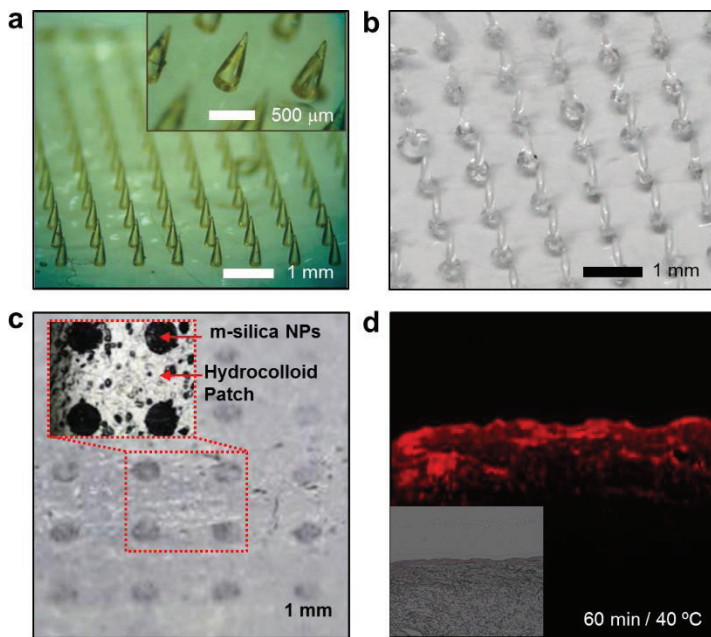


Figure 1.12. Transdermal drug delivery system **(a)** Swellable microneedles. **(b)** Image of the drug loaded microneedles. The drugs are encapsulated with thermos-responsive polymer. **(c)** Optic image of patterned mesoporous silica nanoparticles on the hydrocolloid patch. **(d)** Cross-sectional fluorescence image of mouse skin. Dye is penetrated into the skin under thermal actuation.

1.3.5 Adhesive Patch

To attach wearable electronics on the human skin, adhesive patches have been commonly employed. There are several requirements to be a human-friendly adhesive patch; high adhesive force to attach electronics without slip, skin-like low modulus to reduce feeling of irritation, breathable structure to prevent side effects like allergic response or redish, and repeatable adhesion to be reused. Spin-casted, film type low modulus PDMS or silicon rubber are widely utilized as adhesive patch, however, they cannot be recycled/reused and they are vulnerable to the shear force (**Figure 1.13a and b**).^[51]

Dry adhesives, micro-/nano-structured surface which mimic the gecko's feet, are attracted as new type adhesives without chemical glue. Recently, patch with mushroom-like micropillars are reported to give biocompatibility and restorable adhesion (Figure 1.13c and d).^[52] Moreover, modulus-tunable composite micropillars are demonstrated to enhance compatibility. With the replica molding and inking technique, the modulus of the nanopillar pad can be tuned to skin-like modulus (~50 kPa). This modulus tuning enhances the repeatable adhesion force, and enable to in-vivo recording of heartbeat on the chest (Figure 1.13e and f).^[53]

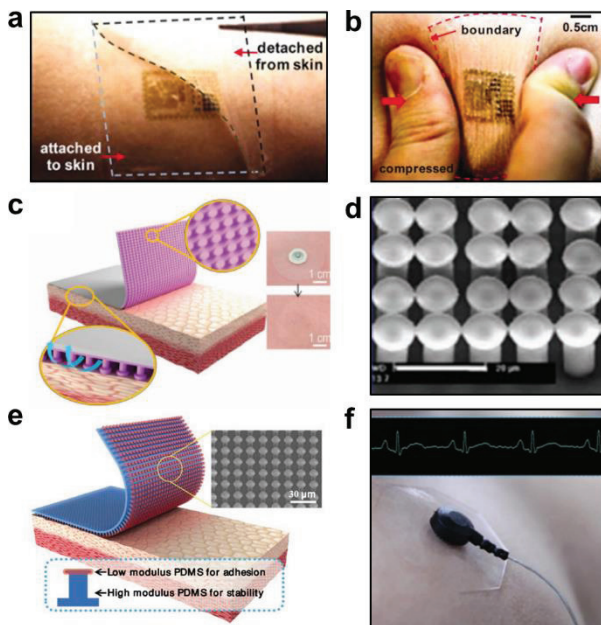


Figure 1.13. Adhesive patch. (a) Optic image of epidermal electronics. Low-modulus PDMS was employed to attach the electronics on the human skin. (b) Optic image of the compressed epidermal devices. The devices completely follow the skin curvatures. (c) Schematic illustration of mushroom-like dry adhesive patch. (d) An SEM image of the mushroom-like dry adhesive structures. (e) Schematic illustration of modulus-tunable dry adhesives. (f) Optic image of the dry adhesives on the chest. Inset shows the measured EKG signal from the electrode.

References

- [1] J. Park, K. An, Y. Hwang, J.-G. Park, H.-J. Noh, J.-Y. Kim, J.-H. Park, N.-M. Hwang, T. Hyeon, *Nat. Mater.* **2004**, 3, 891.
- [2] S. Choi, J. Park, W. Hyun, J. Kim, J. Kim, Y. B. Lee, C. Song, H. J. Hwang, J. H. Kim, T. Hyeon, D.-H. Kim, *ACS Nano* **2015**, 9, 6626.
- [3] P. Y. Huang, C. S. Ruiz-Vargas, A. M. van der Zande, W. S. Whitney, M. P. Levendorf, J. W. Kevek, S. Garg, J. S. Alden, C. J. Hustedt, Y. Zhu, J. Park, P. L. McEuen, D. A. Muller, *Nature* **2011**, 469, 389.
- [4] D.-H. Kim, N. Lu, Y. Huang, J. A. Rogers, *MRS Bulletin* **2012**, 37, 226.
- [5] J. Kim, D. Son, M. Lee, C. Song, J.-K. Song, J. H. Koo, D. J. Lee, H. J. Shim, J. H. Kim, M. Lee, T. Hyeon, D.-H. Kim, *Sci. Adv.* **2016**, 2, E1501101.
- [6] C. Pang, G.-Y. Lee, T.-i. Kim, S. M. Kim, H. N. Kim, S.-H. Ahn, K.-Y. Suh, *Nat. Mater.* **2012**, 11, 795.
- [7] S. Kim, Y. Su, A. Mihi, S. Lee, Z. Liu, T. K. Bhandakkar, J. Wu, J. B. Geddes III, H. T. Johnson, Y. Zhang, J.-K. Park, P. V. Braun, Y. Huang, J. A. Rogers, *Small* **2012**, 6, 901.
- [8] H. Keum, A. Carlson, H. Ning, A. Mihi, J. D Eisenhaure, P. V Braun, J. A Rogers, S. Kim, *J. Micromech. Microeng.* **2012**, 22, 055018.
- [9] H.-J. Chung, T.-i. Kim, H.-S. Kim, S. A. Wells, S. Jo, N. Ahmed, Y. H. Jung, S. M. Won, C. A. Bower, J. A. Rogers, *Adv. Funct. Mater.* **2011**, 21,

3029.

- [10] M. Kaltenbrunner, T. Sekitani, J. Reeder, T. Yokota, K. Kuribara, T. Tokuhara, M. Drack, R. Schwödiauer, I. Graz, S. Bauer-Gogonea, S. Bauer, T. Someya, *Nature* **2013**, 499, 458.
- [11] S. J. Kim, H. R. Cho, K. W. Cho, S. Qiao, J. S. Rhim, M. Soh, T. Kim, M. K. Choi, C. Choi, I. Park, N. S. Hwang, T. Hyeon, S. H. Choi, N. Lu, and D.-H. Kim, *ACS Nano* **2015**, 9, 2677.
- [12] W.-H. Yeo, Y.-S. Kim, J. Lee, A. Ameen, L. Shi, M. Li, S. Wang, R. Ma, S. H. Jin, Z. Kang, Y. Huang, J. A. Rogers, *Adv. Mater.* **2013**, 25, 2773.
- [13] D. J. Lipomi, M. Vosgueritchian, B. C-K. Tee, S. L. Hellstrom, J. A. Lee, C. H. Fox, Z. Bao, *Nat. Nanotechnol.* **2011**, 6, 788.
- [14] H. Lee, T. K. Choi, Y. B. Lee, H. R. Cho, R. Ghaffari, L. Wang, H. J. Choi, T. D. Chung, N. Lu, T. Hyeon, S. H. Choi, D.-H. Kim, *Nat. Nanotechnol.* **2016**, DOI: 10.1038/nnano.2016.38.
- [15] D. K. Kim, Y. Lai, B. T. Diroll, C. B. Murray, C. R. Kagan, *Nat. Commun.* **2012**, 3, 1216.
- [16] T. Yokota, P. Zalar, M. Kaltenbrunner, H. Jinno, N. Matsuhisa, H. Kitanosako, Y. Tachibana, W. Yukita, M. Koizumi, T. Someya, *Sci. Adv.* **2016**, 2, e1301856.

- [17] K. Lambert, Y. Justo, J. S. Kamal, Z. Hens, *Angew. Chem. Int. Ed.* **2011**, 50, 12058.
- [18] C. P. Collier, R. J. Saykally, J. J. Shiang, S. E. Henrichs, J. R. Heath, *Science* **1997**, 277, 1978.
- [19] H. Song, F. Kim, S. Connor, G. A. Somorjai, P. Yang, *J. Phys. Chem. B* **2005**, 109, 188.
- [20] F. Kim, S. Kwan, J. Akana, P. Yang, *J. Am. Chem. Soc.* **2001**, 123, 4360.
- [21] A. Tao, F. Kim, C. Hess, J. Goldberger, R. He, Y. Sun, Y. Xia, P. Yang, *Nano Lett.* **2003**, 3, 1229.
- [22] S. Srivastava, D. Nykypanchuk, M. Fukuto, O. Gang, *ACS Nano* **2014**, 8, 9857.
- [23] F. C. Krebs, *Solar Energy Materials & Solar Cells* **2009**, 93, 394.
- [24] C.-Y. Cai, K.-Y. A. Lin, H. Yang, *Appl. Phys. Lett.* **2014**, 105, 201913.
- [25] J. Krantz, M. Richter, S. Spallek, E. Spiecker, C. J. Brabec, *Adv. Funct. Mater.* **2011**, 21, 4784.
- [26] T.-i. Kim, H. E. Jeong, K. Y. Suh, H. H. Lee, *Adv. Mater.* **2009**, 21, 2276.
- [27] H. E. Jeong, J.-K. Lee, H. N. Kim, S. H. Moon, K. Y. Suh, *Proc. Natl. Acad. Soc.* **2009**, 106, 5639.
- [28] K. S. Martirosyan, C. Dannangoda, E. Galstyan, D. Litvinov, *J. Appl. Phys.* **2012**, 111, 094311.
- [29] L. Liu, X. Wan, L. Sun, S. Yang, Z. Dai, Q. Tian, M. Lei, X. Xiao, C. Jiang, W. Wu, *RSC Adv.* **2015**, 5, 9783.

- [30] A. A. Bessonov, M. N. Kirikova, D. I. Petukhov, M. Allen, T. Ryhänen, M. J. A. Bailey, *Nat. Mater.* **2015**, 14, 199.
- [31] K. Fukuda, T. Sekine, D. Kumaki, S. Tokito, *ACS Appl. Mater. Interfaces* **2013**, 5, 3916.
- [32] T. Aernouts, T. Aleksandrov, C. Girotto, J. Genoe, J. Poortmans, *Appl. Phys. Lett.* **2008**, 92, 033306.
- [33] B. H. Kim, M. S. Onses, J. B. Lim, S. Nam, N. Oh, H. Kim, K. J. Yu, J. W. Lee, J.-H. Kim, S.-K. Kang, C. H. Lee, J. Lee, J. H. Shin, N. H. Kim, C. Leal, M. Shim, J. A. Rogers, *Nano Lett.* **2015**, 15, 969.
- [34] B. Y. Ahn, E. B. Duoss, M. J. Motala, X. Guo, S.-I. Park, Y. Xiong, J. Yoon, R. G. Nuzzo, J. A. Rogers, J. A. Lewis, *Science* **2009**, 323, 1591.
- [35] J. T. Muth, D. M. Vogt, R. L. Truby, Y. Mengüç, D. B. Kolesky, R. J. Wood, J. A. Lewis, *Adv. Mater.* **2014**, 26, 6307.
- [36] J. J. Adams, E. B. Duoss, T. F. Malkowski, M. J. Motala, B. Y. Ahn, R. G. Nuzzo, J. T. Bernhard, J. A. Lewis, *Adv. Mater.* **2011**, 23, 1335.
- [37] A. Rizzo, M. Mazzeo, M. Biasiucci, R. Cingolani, G. Gigli, *Small* **2008**, 4, 2143.
- [38] T.-H. Kim, K.-S. Cho, E. K. Lee, S. J. Lee, J. Chae, J. W. Kim, D. H. Kim, J.-Y. Kwon, G. Amaralunga, S. Y. Lee, B. L. Choi, Y. Kuk, J. M. Kim, K. Kim, *Nat. Photon.* **2011**, 5, 176.
- [39] L. Hu, H. S. Kim, J.-Y. Lee, P. Peumans, Y. Cui, *ACS Nano* **2010**, 4, 2955.

- [40] M.-S. Lee, K. Lee, S.-Y. Kim, H. Lee, J. Park, K.-H. Choi, H.-K. Kim, D.-G. Kim, D.-Y. Lee, S.W. Nam, J.-U. Park, *Nano Lett.* **2013**, 13, 2814.
- [41] B. Y. Ahn, E. B. Duoss, M. J. Motala, X. Guo, S.-I. Park, Y. Xiong, J. Yoon, R. G. Nuzzo, J. A. Rogers, J. A. Lewis, *Science* **2009**, 323, 1590.
- [42] K. S. Kim, Y. Zhao, H. Jang, S. Y. Lee, J. M. Kim, K. S. Kim, J.-H. Ahn, P. Kim, J.-Y. Choi, B. H. Hong, *Nature* **2009**, 457, 706.
- [43] T. Choi, S. J. Kim, S. Park, T. Y. Hwang, Y. Jeon, B. H. Hong, *Nanoscale* **2015**, 7, 7138.
- [44] S. Lim, D. Son, J. Kim, Y. B. Lee, J.-K. Song, S. Choi, D. J. Lee, J. H. Kim, M. Lee, T. Hyeyon and D.-H. Kim, *Adv. Funct. Mater.* **2015**, 25, 375.
- [45] J. Kim, M. Lee, H. J. Shim, R. Ghaffari, H. R. Cho, D. Son, Y. H. Jung, M. Soh, C. Choi, S. Jung, K. Chu, D. Jeon, S.-T. Lee, J. H. Kim, S. H. Choi, T. Hyeyon and D.-H. Kim, *Nat. Commun.* **2014**, 5, 5747.
- [46] J. Kim, A. Banks, Z. Xie, S. Y. Heo, P. Gutruf, J. W. Lee, S. Xu, K.-I. Jang, F. Liu, G. Brown, J. Choi, J. H. Kim, X. Feng, Y. Huang, U. Paik, J. A. Rogers, *Adv. Funct. Mater.* **2015**, 25, 4761.
- [47] J. Kim, A. Banks, H. Cheng, Z. Xie, S. Xu, K.-I. Jang, J. W. Lee, Z. Liu, P. Gutruf, X. Huang, P. Wei, F. Liu, K. Li, M. Dalal, R. Ghaffari, X. Feng, Y. Huang, S. Gupta, U. Paik, J. A. Rogers, *Small* **2015**, 11, 906.
- [48] D. Son, J. Lee, S. Qiao, R. Ghaffari, J. Kim, J.E. Lee, C. Song, S.J. Kim, D.J. Lee, S.W. Jun, S. Yang, M. Park, J. Shin, K. Do, M. Lee, K. Kang,

- C.S. Hwang, N. Lu, T. Hyeon, D.-H. Kim, *Nat. Nanotechnol.* **2014**, 9, 397.
- [49] C. Yeom, K. Chen, D. Kiriya, Z. Yu, G. Cho, A. Javey, *Adv. Mater.* **2015**, 27, 1561.
- [50] S. Y. Yang, E. D. O'Cearbhail, G. C Sisk, K. M. Park, W. K. Cho, M. Villiger, B. E. Bouma, B. Pomahac, J. M. Karp, *Nat. Commun.* **2013**, 4, 1702.
- [51] D.-H. Kim, N. Lu, R. Ma, Y.-S. Kim, R.-H. Kim, S. Wang, J. Wu, S. M. Won, H. Tao, A. Islam, K. J. Yu, T.-i. Kim, R. Chowdhury, M. Ying, L. Xu, M. Li, H.-J. Chung, H. Keum, M. McCormick, P. Liu, Y.-W. Zhang, F. G. Omenetto, Y. Huang, T. Coleman, J. A. Rogers, *Science* **2011**, 333, 838.
- [52] M. K. Kwak, H.-E. Jeong, K. Y. Suh, *Adv. Mater.* **2011**, 23, 3949.
- [53] W. G. Bae, D. Kim, M. K. Kwak, L. Ha, S. M. Kang, K. Y. Suh, *Adv. Healthc. Mater.* **2013**, 2, 109.

Chapter 2. Wearable Red-Green-Blue Quantum Dot Light-Emitting Diode Array Using High Resolution Intaglio Transfer-Printing

2.1 Introduction

Many mobile electronic devices, including smartphones and tablets, consist of electronic and optoelectronic components, such as microprocessors, memory modules, and high resolution information displays. More advanced systems provide the higher mobility by shifting platforms from rigid/planar to wearable/deformable ones. Recently, significant progresses have been made in flexible and stretchable electronics.^[1-4] However, the deformable, high resolution full-colour light-emitting diode (LED) array, which is used as input/output terminals in wearable electronic systems, is a daunting goal.^[5-8] Although previous reports showed great breakthroughs, such as flexible and/or stretchable inorganic LEDs,^[9] polymer LEDs,^[10-12] and organic LEDs,^[13-15] practical challenges (e.g. full-colour display, luminous efficiency, and ultrathin thickness) still remain.

Among various light-emitting devices, colloidal quantum dot LEDs (QLEDs) have attracted great attention as next-generation displays based on

electroluminescence (EL).^[16–23] Quantum dots (QDs) have distinctive optoelectronic properties,^[24,25] such as the colour tunability,^[26–29] narrow PL emission spectra,^[30] high quantum yield,^[31] and photo-/air-stability.^[32] Additional advantages include printability on various substrates,^[33,34] ultrathin active layers,^[35] and high luminescence at low operating voltages in QLEDs.^[36–38] However, previously reported QLEDs are not suitable for wearable displays because they are not deformable in multiple directions. In addition, for full-colour wearable QLED displays, the red-green-blue (RGB) sub-pixels should be precisely aligned with high resolution, which cannot be realized by the conventional solution processes.^[39,40] Dry transfer-printing provides an effective route to fabricate pixelated RGB QD films over a large area, but the previous printing methods^[41–44] using structured stamps have severe discrepancies between the original designs and the resulting pixel shapes, particularly in high-definition designs.

Here, we report ultrathin and wearable RGB QLED arrays based on the high resolution intaglio transfer-printing technique. This novel transfer-printing process uses a rigid intaglio trench to create full-colour QD arrays with controlled and uniform pixel sizes that can achieve 2,460 pixels per inch (ppi) resolution. These aligned RGB pixels can be utilized to fabricate efficient true-white LEDs or active matrix-driven full-colour displays. Furthermore, high-

efficiency deformable QLEDs (brightness of 14,000 cd m⁻² under the low driving voltage of 7 V, which is the best device performance among the wearable LEDs reported so far^[6,10,14,15]) are applied in electronic tattoo demonstrations as a practical example of wearable devices. Ultrathin designs enable QLEDs to conform to various curvilinear and dynamic surfaces and maintain high EL performances after 1,000 repeated deformation tests.

2.2. Experimental Section

2.2.1 Materials

The CdSe/ZnS QDs for blue and green QDs and the CdSe/CdS/ZnS QDs for red QDs were synthesized in the laboratory. All QDs have CdSe-ZnS core-shell alloyed structures to enhance EL and show a PL quantum yield of > ~80%. Poly(3,4-ethylenedioxythiophene): poly(styrenesulfonate) (PEDOT:PSS) (VP AI 4083) was purchased from Clevios, and TFB (SOL 2036) was purchased from Solaris. Anhydrous butanol, heptane, and m-xylene were purchased from Sigma-Aldrich. Zinc oxide nanocrystals (NCs) for the electron transport layer, PbS QDs and CuInSe QDs were synthesized in the laboratory. Cadmium oxide (CdO, >99.99%), zinc acetate ($Zn(OAc)_2$, 99.99%), zinc acetate dehydrate ($Zn(OAc)_2 \cdot (H_2O)_2$, 99.9%), lead chloride ($PbCl_2$, 99.999%), elemental sulfur (S, 99.99%), elemental selenium (Se, 99.99%), oleic acid (OA, 90%), 1-octadecen (1-ODE, 90%), trioctylphosphine (TOP, 97%), tributylphosphine (TBP, >93.5%), 1-octanethiol (98.5%), anhydrous cyclohexane, and anhydrous ethanol were purchased from Sigma-Aldrich. Oleylamine (OLAm, 80-90%) was purchased from Acros Organics. Indium iodide (InI_3 , 99.999%) and copper iodide (CuI , 99.998%) were purchased from Alfar Aesar. Prior to use, OA, 1-ODE, and OLAm were degassed at 120°C under vacuum for 4 h.

2.2.2 Synthesis of CdSe/CdS/ZnS Red QDs

Red light-emitting CdSe/CdS/ZnS core/shell QDs were prepared by multiple injections of precursors. In a glove box, 1.2 mmol of CdO was added into the reaction solvent composed of 1.5 mL of OA and 20.0 mL of 1-ODE. The mixture was degassed under vacuum for 2 h at 130°C and then heated to 300°C under Ar atmosphere. At this elevated temperature, 0.3 mmol of TOPSe (1M) solution was rapidly injected into the Cd-(oleate)₂ solution. The reaction was maintained to allow CdSe cores to grow into the desired sizes. Then, 0.9 mmol of 1-octanethiol was slowly introduced into the reacting solution at 300°C to form CdSe/CdS core/shell QDs. After 40 min of CdS shell growth, 4.8 mmol of Zn-(oleate)₂ and 4.8 mmol of TBPS solution (2 M) were slowly injected into the solution to form thick ZnS outer shells on the CdSe/CdS QDs. The reaction mixture was kept at 300°C for 15 m for the further growth of the ZnS outer shell. The product was purified by repeating the precipitation/redispersion processes to remove excessive shell reagents. The as-synthesized CdSe/ZnS alloyed QDs were treated with oleic acid to guarantee dispersibility of the QD solution. The FTIR spectrum of QD samples was analysed at ATR-FTR mode on Tensor 27 (Bruker, Germany) installed at the National Center for Inter-university Research Facilities (NCIRF) in Seoul National University.

2.2.3 Synthesis of CdSe/ZnS Green QDs

Green light-emitting CdSe/ZnS core/shell QDs were prepared from the reaction between metal-oleate and TOPS and TOPSe. For the preparation of Cd-(oleate)₂ and Zn-(oleate)₂ solution, 0.2 mmol of CdO and 4.0 mmol of Zn(OAc)₂ were added into the reaction solution composed of 6.0 mL of OA and 15.0 mL of 1-ODE in a glove box. The mixture was degassed under vacuum for 2 h at 130°C and then heated to 300°C under Ar atmosphere. At this elevated temperature, 0.2 mmol of TOPSe solution (1 M) was rapidly injected into the solution followed by the injection of 4 mmol of TOPS solution (1 M) to form ZnS shells on the cores. The reaction mixture was held at 300°C for 15 min. The product was purified by repeating the precipitation/redispersing processes to remove excessive shell reagents.

2.2.4 Synthesis of CdSe/ZnS Blue QDs

Blue light-emitting CdSe/ZnS core/shell QDs were prepared using the reaction between metal-oleate and elemental S and Se. To prevent rapid growth of QDs, consequently, in order to obtain blue light-emitting QDs, elemental S and Se were employed as anion precursors instead of as general precursors such as TOPSe and TOPS solution. For the preparation of Cd-(oleate)₂ and Zn-(oleate)₂ solution, 1.0 mmol of CdO and 9.0 mmol of Zn(OAc)₂ were added

into the reaction solution composed of 8.0 mL of OA and 15.0 mL of 1-ODE in a glove box. The mixture was degassed under vacuum for 2 h at 130°C and then heated to 300°C under Ar atmosphere. At 300°C, 1.8 mmol of S and 0.2 mmol of Se dissolved in 3 mL of 1-ODE were injected into the Cd-(oleate)₂ and Zn-(oleate)₂ solution. After 10 min of reaction, without any purification, 8.0 mmol of TBPS solution (2 M) was slowly injected into the reaction mixture at 300°C. The reaction mixture was held at the same temperature for 50 min for the formation of thick ZnS shells on the cores. The product was purified by repeating the precipitation/redispersion processes to remove excessive shell reagents.

2.2.5 Synthesis of Zinc Oxide NCs

Zinc oxide (ZnO) NCs were synthesized using a method modified from a previous report.^[45] First, 0.48 g of KOH in 25-ml methanol was added dropwise to 1.23 g of Zn(OAc)₂·(H₂O)₂ in 55-ml methanol over 2 h at 60°C in ambient conditions. This solution is reacted for 2 h at 60°C. The product was purified by repeating the precipitation/redispersion method using the hexane and isopropyl alcohol mixture and redispersed in butanol. Before used as the electron transport layer, the ZnO NC solution was processed through a 200-nm porous cellulose acetate filter.

2.2.6 Synthesis of PbS IV-VI Semiconductor QDs

The PbS IV-VI semiconductor QDs were synthesized using the method in our previous report.^[46] In a glove box, 1 mmol of PbCl₂ was added into 5 mL of OLAm. The mixture was degassed under vacuum for 2 h at 90°C, forming a clear solution containing metal-amine complex. Then, 0.83 mmol of amine-sulfur complex solution (0.83 mmol elemental sulfur was dissolved in 2.5 mL of oleylamine) was rapidly injected into the Pb-oleylamine complex solution at 90°C. The resulting black colloidal solution was heated to 220°C and held at that temperature for 1 h for further PbS QD growth. The product was purified by repeating the precipitation/redispersion process.

2.2.7 Synthesis of Cu-In-Se I-III-VI Semiconductor QDs

The Cu-In-Se I-III-VI semiconductor QDs were synthesized using the method in our previous report.^[47] For the synthesis of 5-nm QDs, 0.5 mmol of copper (I) iodide (0.095 g) and 0.5 mmol of indium (III) iodide (0.248 g) were added into 15 mL of oleylamine. The solution was degassed under vacuum for 30 m at 120°C, forming a clear solution of metal-amine complexes. Oleylammonium selenocarbamate was separately prepared by the reaction of carbon monoxide (CO), 5.0 mmol of selenium powder, and 10 mL of oleylamine at 120°C. The 2.0 mL of oleylammonium selencabamate solution

was injected into the metal-amine complex solution at 70°C under an Ar atmosphere. The reaction solution was heated to 210°C and held at that temperature for 20 min. The product was precipitated by ethanol-containing TOP followed by repeating the purification process (precipitation/redispersion method).

2.2.8 Characterization of Nanocrystal Materials

Transmission electron microscopy (TEM) images were obtained by a JEOL 2100F electron microscope. The absorption spectra were acquired by a CARY 5000E UV-VIS-NIR spectrophotometer. Photoluminescence (PL) and time-resolved fluorescence spectra were recorded by an FLS 980 spectrometer (Edinburgh Instruments). For PL, the QDs were excited with a steady-state xenon lamp, and the emitted photons were detected by a single-photon-counting photomultiplier. The valance band maximum of the layer materials was determined by the ultraviolet photoelectron spectroscopy (Thermo Fisher Scientific Co.) with a He discharge lamp (21.2 eV).

2.2.9 Intaglio Transfer-Printing

The QD layer was spin-casted on the 1-octadecyltrimethoxysilane (ODTS) treated silicon (Si) substrate (donor substrate), and a flat PDMS stamp

was utilized to quickly pick up (10 cm/s) the QD layer.^[41] The picked-up QD layer was conformally contacted on the intaglio trench with the low applied pressure and slowly detached. Then, the intaglio QD patterns are formed on the stamp. Finally, the non-contacted QD layer, i.e. intaglio patterns, remaining on the stamp can be transferred to the desired substrate. The intaglio trenches were negatively carved on the Si substrate using the deep Si etcher (Versaline, PLASMA THERM). The residual QD layers on the trench were easily eliminated through either the mechanical rubbing or cleaning in piranha solution; thus, intaglio trenches are reusable.

2.2.10 Finite-Element Method (FEM) Simulation of the Intaglio Transfer Printing and Structured Stamping Method

To analyse different yields of the pick-up and transfer printing process, FEM simulations of the structured stamping and of the intaglio transfer printing were used, as shown in Figure 2.6 as well as Figure 2.3b and c. The substrates and stamps were modelled as rigid bodies, and the quantum dot (QD) layer was modelled as a single layer of continuum particle elements, as shown in Figure 2.6a and b. For transferring a square pixel (size: 150 µm × 150 µm), a structured stamp (150 µm × 150 µm with 20-µm height) was used in the structured stamping method (Figure 2.6a). In the intaglio transfer technique, on the other

hand, a $150 \mu\text{m} \times 150 \mu\text{m}$ square trench and a flat stamp were utilized (Figure 2.6b). The QD/stamp interaction and QD/substrate interaction were modelled using the cohesive contact. Surfaces followed the traction-separation behaviour, $t = K\delta$, where t is the traction normal to the surface, δ is the separation between the surfaces, and K is the coefficient representing the bonding strength. If the separation reaches a critical value, the traction gradually degrades to zero, and two surfaces are regarded as debonded. Following values were used in the simulation: $K_{stamp/QD} = 4.2 \times 10^{-5} \text{ Pa}/\mu\text{m}$ and $K_{substrate/QD} = 4.0 \times 10^{-5} \text{ Pa}/\mu\text{m}$ in the structured stamping and $K_{stamp/QD} = 1.5 \times 10^{-5} \text{ Pa}/\mu\text{m}$ and $K_{substrate/QD} = 3.0 \times 10^{-5} \text{ Pa}/\mu\text{m}$ in the intaglio printing. These values were selected by considering the bonding strength differences. In the structured stamping, $K_{stamp/QD}$ is larger than $K_{substrate/QD}$, but the difference is small. In the intaglio transfer printing, $K_{stamp/QD}$ is smaller than $K_{substrate/QD}$, which is reasonable because of the slow pick-up procedure. The pick-up process was simulated by moving the stamp upward while fixing the substrate. The resulting FEM simulation results for QD transfer-printings are shown in Figure 2.3b and c, which are well matched with the experimental results shown in Figure 2.3a.

The details of FEM simulations used to analyse the delamination and crack propagation of QD layers near the edge of stamps (Figure 2.6c and d) are given as follows. The substrate was modelled as a rigid body, whereas the

structured stamp and the QD layer were modelled using three-dimensional solid elements. The thickness of the QD layer is \sim 40 nm, and the corner radius of the elastomeric stamp is \sim 350 nm. The surfaces followed the traction-separation behaviour, $t = K\delta$. The incompressible Neo-Hookean model was used to represent the polydimethylsiloxane (PDMS) stamp: $W = C_1(I_1 - 3)$, where W is the strain energy potential, I_1 is the first invariant of the left Cauchy-Green tensor, and C_1 ($=$ 383.5 kPa for PDMS) is a material parameter. The QDs were modelled as a plastic material with an initial yield stress of 10^{-4} MPa, and the fracture occurs after the strain reaches 0.01. Figure 2.6e shows the normal stress distribution to the vertical direction. The stress is localized at the edge of the stamp, initiating the delamination between the stamp and the QD layer (Figure 2.6e (i)). The delamination proceeds until it meets the delamination between the substrate and the QD layer, which results in the fracture of the QD layer inside of the pixel edge (Figure 2.6e (ii)). In the intaglio transfer technique, on the other hand, the stress is focused on the edge of pattern, where the crack is formed exactly at that location (Figure 2.6f (i) and (ii)). The bonding strength between the substrate and the QD layer is much higher than that between the stamp and the QD layer, which explains Figure 2.6d and f.

2.2.11 Fabrication of PWQLEDs

To fabricate PWQLEDs, ~100-nm-thick indium tin oxide (ITO) on polyethylene terephthalate (PET) substrate was patterned and successively cleaned with the acetone, isopropyl alcohol (IPA), deionized water, and IPA. After the 5 min of ultraviolet ozone (UV/O₃) treatment, an anode substrate was spin-coated with Poly(3,4-ethylenedioxythiophene): poly(styrenesulfonate) (PEDOT:PSS) followed by annealing at 120°C for 10 min. Then, poly[(9,9-dioctylfluorenyl-2,7-diyl)-co-(4,4'-(N-(4-sec-butylphenyl))diphenylamine)] (TFB) was spin-coated at 2,000 rpm and annealed at 150°C for 30 min. Each red-green-blue (RGB) QD pixel was precisely patterned on the annealed TFB layer by the intaglio transfer printing. A custom-made transfer printer, which could control the pressure and pick-up rate, was used to pick up QD layers from the donor substrate. A manual-type mask aligner was used for the delicate alignment of RGB pixels on the TFB layer. The area ratio of RGB pixels in PWQLEDs was 1:1:2. After transferring the QD layer, the device was annealed at 150°C for 30 min. A 40-nm-thick ZnO nanocrystal (NC) layer was utilized for the electron transport layer, which was spin-coated on the transferred QD layer, followed by annealing at 120°C for 10 min. A 50-nm-thick lithium-aluminium alloy cathode was then thermally evaporated at a rate of 0.1 nm/s through a shadow mask. Final encapsulations are added for the protection.

2.2.12 Fabrication of Mixed White QLEDs (MWQLEDs)

In this work, MWQLEDs refer to QLEDs whose active layer is composed of mixed R, G, and B QDs in the solution. The fabrication process of MWQLEDs is same as that of PWQLEDs (Supplementary Text 1.2), except for the procedure for the active layer. Mixed QD solutions, in different volume ratios of each QD dispersion, were utilized to manufacture the active layer in MWQLEDs; the ratio of each RGB QD dispersion was 1:1:2. Before mixing QD solutions, the concentration of each QD solution was adjusted to make 40-nm-thick QD layers by spin casting. The mixing ratio of the QD solution was matched with the ratio of the RGB pixel area of PWQLEDs (the area ratio of RGB pixels in PWQLEDs is 1:1:2).

2.2.13 Fabrication of Wearable QLEDs

The nickel sacrificial layer was evaporated on a cleaned Si wafer. The bottom encapsulation film was composed of double-layered Parylene-C and epoxy (SU8-2000.5, MicroChem), the spin-coated 600-nm-thick epoxy on the Ni-coated Si wafer followed by evaporated 500-nm-thick Parylene-C. The film was then annealed at 95°C for 1 min and then at 150°C for 30 min after UV exposure. The Parylene-C layer protects QLEDs from the oxidation, and the epoxy layer prevents the Parylene-C film from the delamination and provides

an ultra-flat surface through the reflowing process. Indium tin oxide (ITO) was sputtered on the encapsulation film (50 W, 30 min, 5 mTorr, 200°C) and patterned. Then, PEDOT:PSS was spin-casted on the UV/O₃-treated cathode at 2,000 rpm for 30 s. The resulting cathode was annealed at 120°C for 10 min in the ambient atmosphere and annealed at 150°C for 10 min in a glove box to remove the residual solvent. 0.5 wt% poly[(9,9-dioctylfluorenyl-2,7-diyl)-co-(4,4'-(N-(4-sec-butylphenyl))diphenylamine)] (TFB) in m-xylene was spin-coated and annealed at 150°C in the glove box. The QD layer was transfer-printed on the ITO pattern by the intaglio transfer-printing method in air and annealed at 150°C in the glove box. In addition, Zinc oxide (ZnO) nanocrystals in butanol were spin-coated and annealed at 145°C. Finally, the anode material, Li/Al alloy, was thermally evaporated for ~80 nm and encapsulation layers (Parylene-C and epoxy layers) were deposited to protect the device. The encapsulated device was flooded in the Ni etchant to dissolve the sacrificial layer. For the buckled, stretchable QLEDs, ultrathin QLEDs were transfer-printed on the pre-stretched PDMS layer, followed by a mild annealing treatment to dry any residual water. Current flows through the vertically overlapped area between ITO and Li/Al.

2.2.14 PL Lifetime Measurements

Time-resolved PL spectroscopy data were obtained by a time-correlated single-photon-counting module in the FLS 980 spectrometer (Edinburgh Instruments, U.K.). The individual R/G/B QDs, RGB mixed QDs, and RGB aligned pixelated QDs on quartz substrates were excited using a ~376-nm laser (EPL-375). The pulse width and repetition rate of the pulsed diode laser were ~74.5 ps and ~5 MHz, respectively. The PL was spectrally dispersed in a monochromator (1,800 gr/mm grating) and detected with a micro-channel plate photomultiplier (detector response width < 25 ps) at the emission maxima of each colour (440 nm, 520 nm, and 640 nm for blue, green, and red, respectively). The pulsed laser and time-correlated single-photon-counting system provided a time window of 50 ns with 8,192 data channels.

2.2.15 Device Characterization

The current-voltage curves for QLEDs were measured with a Keithley 2436 source meter. The EL of QLEDs was measured with a CS-2000A spectrophotometer (measurement spot size < 500 µm) by sweeping the applied voltage from 0 to 8 V. The white QLED and flexible QLED measurements were performed at room temperature in the glove box, and all stretchable and deformable QLED measurements were performed in ambient conditions. All

the device characteristics were measured and averaged with 6 different devices and 12 different LED units.

Result and discussion

2.3.1 High Resolution Intaglio Transfer-Printing

For high-definition full-colour RGB QLED arrays, a novel QD integration process, known as the intaglio transfer-printing, has been developed through which nanocrystal layers can be transfer-printed on various substrates regardless of the size, shape, and arrangement of pixels. The procedure is illustrated in **Figure 2.1a**. The QD layer coated on the donor substrate was quickly picked up with a flat elastomeric polydimethylsiloxane (PDMS) stamp (Figure 2.1a (1)). The picked-up QD layer was lightly contacted on the intaglio trench (Figure 2.1a (2)) with a pressure of $< 50 \text{ g cm}^{-2}$ and slowly detached $< 1 \text{ mm s}^{-1}$ (Figure 2.1a (3)). Only the non-contacted part of QD layer stayed on the stamp and was transfer-printed on the target substrate (Figure 2.1a (4)). This transfer-printing is facilitated by the differences in surface energy between PDMS stamp and the target substrates (19.8 mJ m^{-2} for the PDMS, and $> 200 \text{ mJ m}^{-2}$ for the glass, organic layers, and oxide layers) on which the QD layer can be tightly bound. Based on the same principle, multiple transfer-printings are also possible (Figure 2.1a (5), (6)); the second QD layer is exquisitely integrated on the first layer without any morphological changes. The resulting photoluminescence (PL) image is shown in Figure 2.1b. The optical microscope images (Figure 2.1c) and fluorescence microscope images (insets) show

magnified views of each colour pattern Figure 2.1b, which consists of tens of micron-sized pixels (triangle, hexagon, and star patterns). High resolution aligned RGB pixels, 2,460 ppi (6 μm pixel size; magnified view in inset), can be created by the multiple printing processes described above (**Figure 2.2**), demonstrating that the novel method is applicable to ultrahigh resolution full-colour QD displays.

As the pixel size decreases, the intaglio transfer-printing technique becomes more important. We compare results obtained from the intaglio transfer-printing (current) and structured stamping (conventional) methods (**Figure 2.3a–c**). See Figure 2.1a (intaglio printing) and **Figure 2.4** (structured stamping) for the comparison of processes. In Figure 2.3a, the white areas represent the transferred QDs. The fraction of the non-transferred area in the structured stamping method increases at higher resolution. On the contrary, the intaglio transfer-printing process accomplishes the transfer yield of ~100%. The same tendency is observed in different shape (circular dots; **Figure 2.5**), demonstrating ~100% transfer yield regardless of the size or shape of the patterns. The discrepancies from the designed patterns are particularly dominant near the edges of dot (square and circle) patterns. The importance of fine dot patterns are particularly highlighted in patterning complex RGB pixels in full colour displays.

Theoretical analysis of the enhanced yields of high resolution patterning in the intaglio transfer-printing over the structured stamping was performed using the finite-element method (FEM). **Figure 2.6a–d** compare two methods by simulating the transfer-printing of a square pixel (size: 150 µm × 150 µm). In the structured stamping method, the shape is determined by the pick-up process (process (1) and (2) of Figure 2.4). As the contacted structure stamp is rapidly retrieved, the delamination between the stamp and the QD layer is initiated from edges of the stamp structure and propagates into the centre of the stamp structure, which induces stresses and generates cracks in the QD layer (Figure 2.6e). Cracks of the QD layer, therefore, occur at the inside of designed pixel edges and result in a reduced pixel size (Figure 2.3b). On the contrary, in the intaglio transfer-printing method, the pixel shape is determined by the QD release process from the flat stamp to the intaglio trenches (process (2) and (3) of Figure 2.1a). Cracks of the QD layer occur at sharp edges of intaglio trenches (Figure 2.6f). Therefore, the obtained pixel pattern precisely matches the original design (Figure 2.3c). The QD/intaglio-trench interfacial energy, which is much higher than the QD/stamp interfacial energy, further helps the high definition and yield. See Supplementary Methods for details of FEM simulations and related mechanical analysis.

The intaglio printing process can be generalized to transfer various QD

layers (**Figure 2.7**) regardless of QD materials (CuInSe and PbS) or sizes (2–18 nm). Furthermore, the current method is readily expanded over large areas by the repetitive aligned transfer-printing, which is a critical technology for the mass production (Figure 2.3d). Often, distances between pixels should be variable depending on pattern designs. The structured stamping method shows the sagging and leaning of structures in elastomeric stamps, thereby showing low yields, particularly with a large pattern spacing (**Figure 2.8a and c**). However, the intaglio stamping method does not exhibit these defects (Figure 2.8b and c).

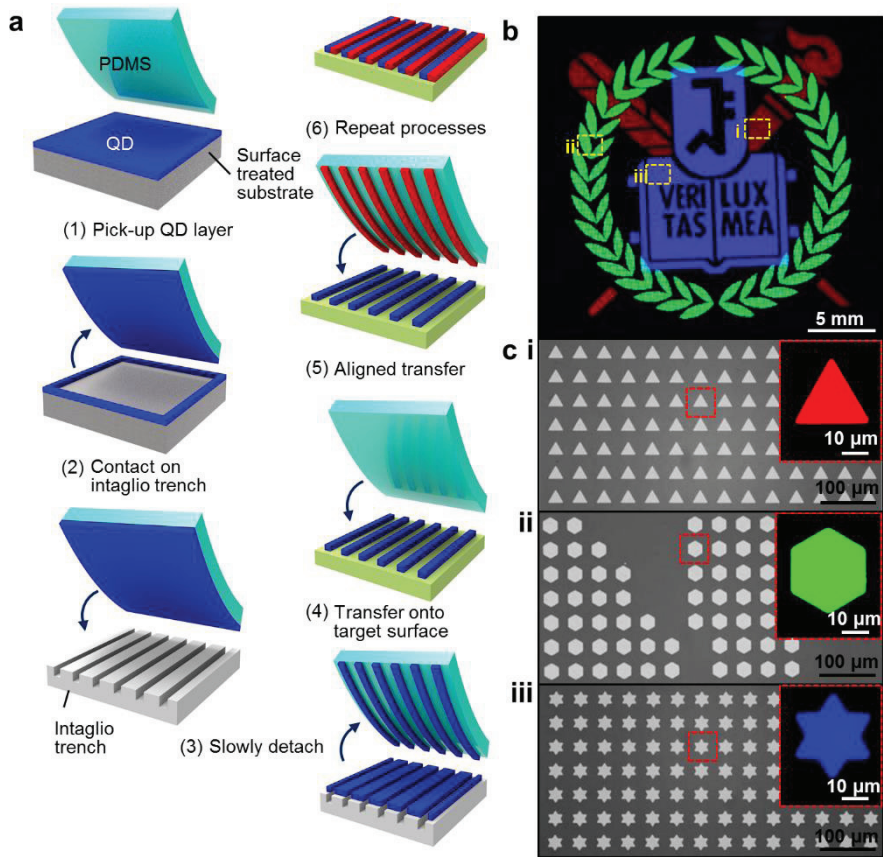


Figure 2.1. Intaglio transfer-printing for high resolution RGB QLEDs. (a) Schematic illustration of the intaglio transfer-printing process. Inset images on the left of each frame show the side view. **(b)** The PL image of the RGB QD patterns via multiple aligned transfer-printings. **(c)** Magnified views of selected regions of Figure 1b. Each colour pattern consists of thousands of tens-of-microns-sized pixels (red: triangle (top), green: hexagon (middle), and blue: star (bottom)). Insets show further magnified PL images.

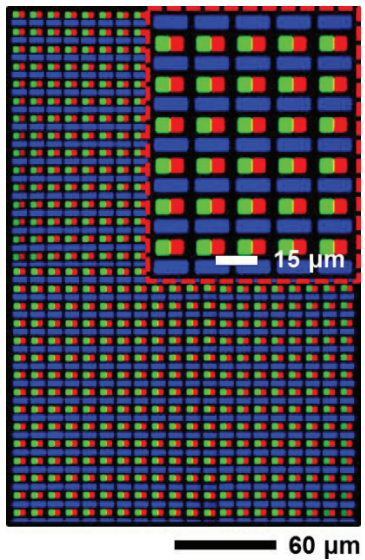


Figure 2.2. The PL images showing aligned RGB pixels whose resolution is 2,460 pixels per inch (ppi).

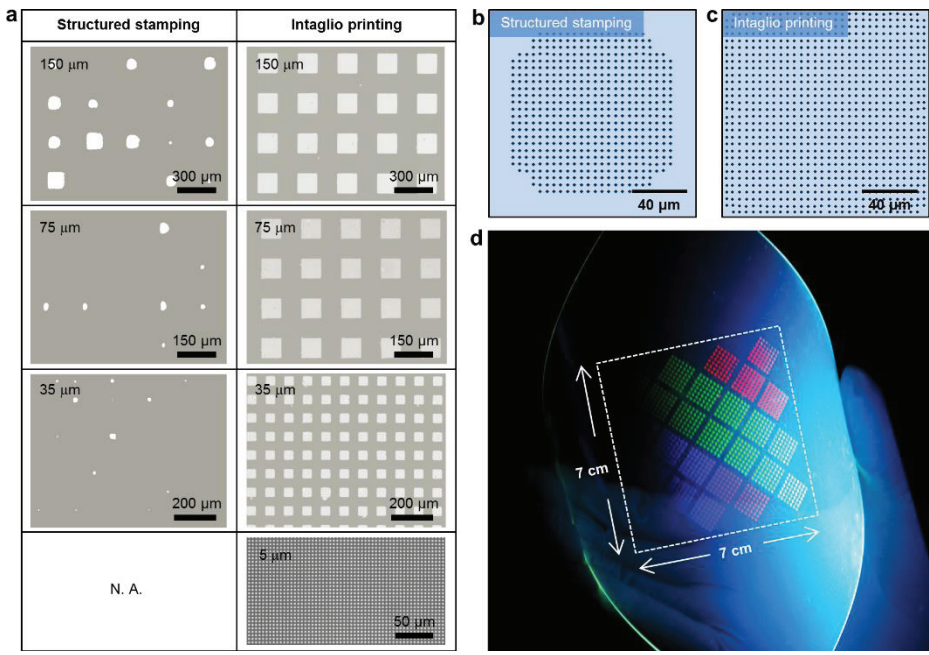


Figure 2.3. Experimental and theoretical analysis of the intaglio transfer-printing. (a) Pattern-size scaling in the structured stamping (left) and intaglio transfer-printing (right). QD transfer yields of the structured stamping dramatically decrease especially in high resolutions, while those of the intaglio printing approach ~100% in all design rules. (b, c) Finite-element method simulations of the transferred area of the rectangular pattern (size: 150 µm × 150 µm) for the structured stamping (b) and intaglio printing (c). (d) PL image of a large-area QD dot array (7 cm × 7 cm) patterned by repeated aligned intaglio transfer-printing on a flexible polyethylene terephthalate (PET) substrate.

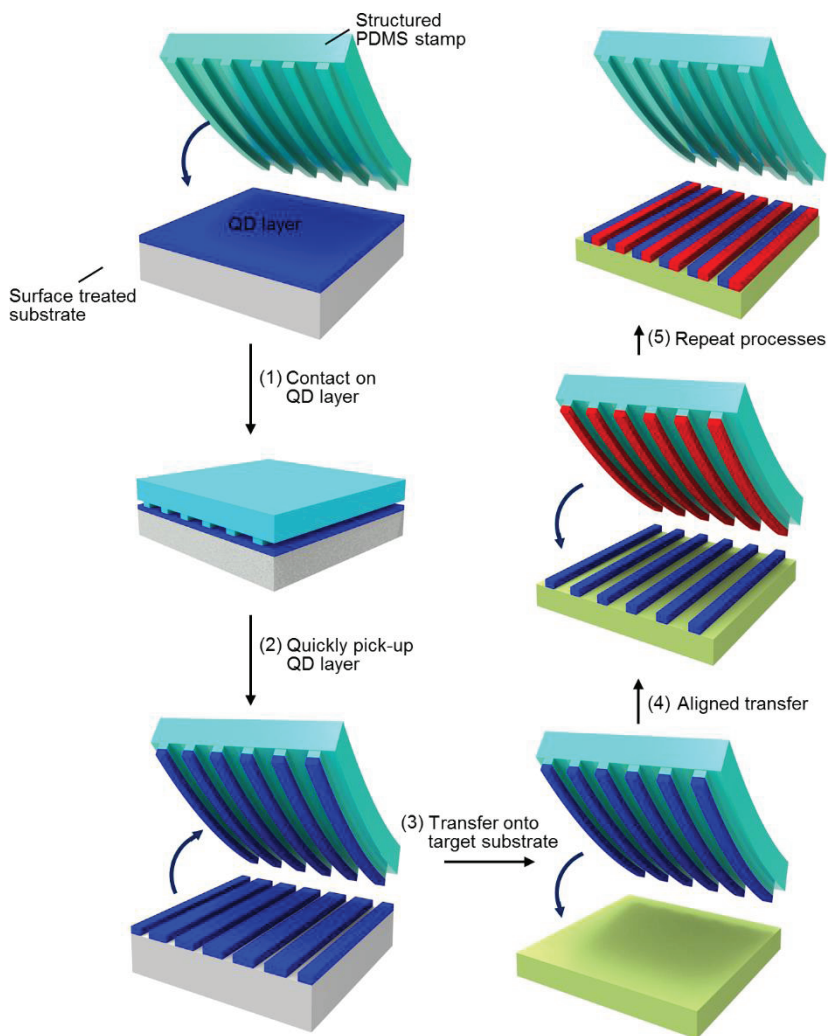


Figure 2.4. Schematic illustration of the structured stamping method. The QD layer is directly picked up from the ODTs-treated substrate by the structured PDMS stamp. This process is previously reported and widely used as the dry transfer-printing method.

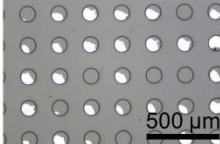
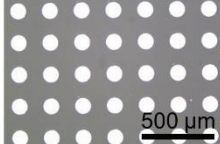
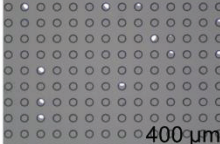
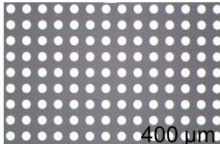
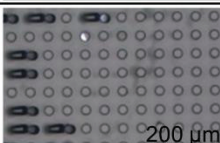
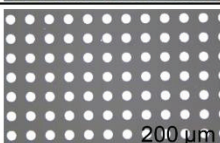
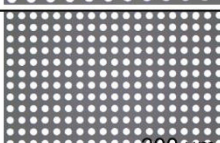
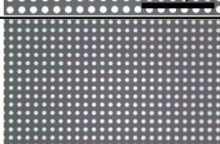
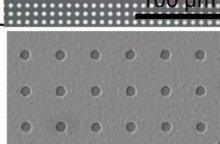
Pixel size (μm)	Structured stamping	Intaglio printing	PPI	5' (smart phone)
100			127	-
45			282	-
30			423	Retina
16	N. A.		794	FHD
5	N. A.		2540	UHD
<1	N. A.		<13,000	μLED

Figure 2.5. Circular pattern-size effect on the yield of transfer printing

QDs. As the designed circular pattern size decreases, the transfer yield in the structured stamping method dramatically decreases. On the contrary, the transfer yield in the intaglio printing method approaches ~100% regardless of the pattern size.

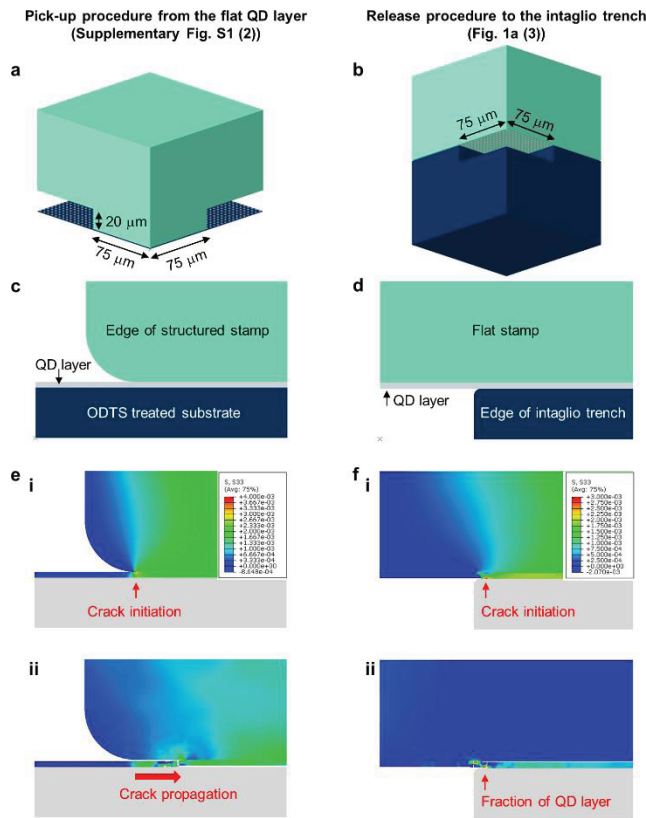


Figure 2.6. Finite-element method (FEM) simulations of the structured stamping and intaglio printing method. (a, b) One quarter of the single-dot structured stamp (a) and the single-dot trench (b) contacting the substrate. (c) The magnified side-view of the edge of the structured stamp at the pick-up process (process (2) of Supplementary Fig. 1). The structured stamp in contact with the spin-casted QD layer on the ODTs-treated substrate. (d) The magnified side-view of the edge of the intaglio trench at the releasing process (process (3) of Fig. 1a). The picked-up QD layer in contact with the intaglio trench. (e) Gradient of normal stress on the QD layer and edge of the structured stamp. As the stamp moves upward (pick-up), cracks propagate from the edge into the centre of the stamp (i → ii). (f) Gradient of normal stress on the QD layer and the flat elastomeric stamp (i). Cracks do not propagate into the centre, and the QD layer is broken at edge of the trench (ii).

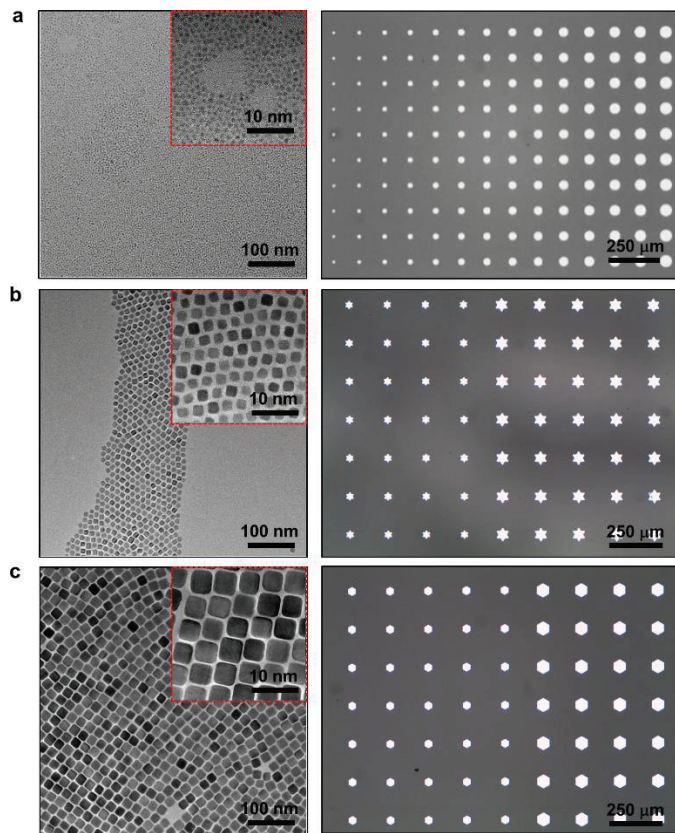


Figure 2.7. Intaglio transfer printing demonstrations of various QDs. **(a)** A TEM image of Cu-In-Se QDs (size: 2 nm) (left) and intaglio transfer-printed dot patterns (right) using the Cu-In-Se QD layer. **(b, c)** The TEM images of PbS QDs (8 nm **(b)**, and 18 nm **(c)**) (left) and intaglio transfer-printed patterns (right) using the PbS QD layers. Insets of each image in the left column show the high-resolution TEM images.

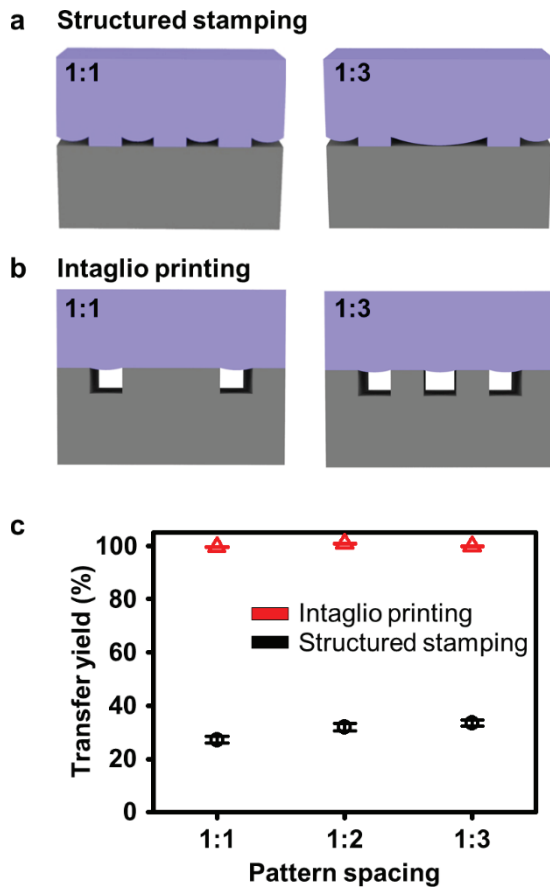


Figure 2.8. Effect of pattern spacing on the transfer-printing yield. (a) An illustration of the structured stamp with various pattern spacings (pattern:space = 1:1 and 1:3). When the pattern spacing is wide during the pick-up procedure, the stamp may sag or lean because of the high applied pressure, causing deformation in the resulting patterns. (b) An illustration of the intaglio trench with various pattern spacings (pattern:space = 1:1 and 1:3). Because the applied pressure on the flat stamp is much lower than that on the structured stamp, deformation of the stamp can be neglected, and the resolution of the pattern is not affected by pattern spacing. (c) Transfer yield versus pattern spacing.

2.3.2 White LEDs Fabricated by Transfer-Printing of RGB QDs

Our intaglio transfer-printing technique can be employed to create high-quality pixelated white QLEDs (PWQLEDs) on human arm (**Figure 2.9a**). Conventional white QLEDs have employed a mixture of several kinds of QDs and phosphors of different characteristic wavelengths.^[48–52] However, these white QLEDs have been proven to be ineffective due to the inescapable energy transfer between the different sized QDs/phosphors (e.g. Förster energy transfer).^[53,54] In the mixed system, it is difficult to obtain balanced white light because the energy transfer occurs from B to G, R, and from G to R. Therefore, it is desired to realize white emission by controlling the injected current of each RGB sub-pixel in the pixelated LED arrays, rather than by controlling RGB luminophore content in the mixed system.

On the other hand, the current flexible PWQLEDs utilize aligned RGB fine pixels (Figure 2.9b), whose colour can be tuned to be the true white with high efficiency. We unify QD materials using CdSe/ZnS alloyed QDs (**Figure 2.10**) to minimize variations in the RGB EL brightness and to prevent the inefficient blue EL of CdS-based QDs.^[35,42] All the CdSe/ZnS alloyed QDs have the same type of ligand, oleic acid (**Figure 2.11**). Figure 2.9c shows the band diagram for PWQLEDs, which is estimated from the ultraviolet (UV) photoelectron spectra (**Figure 2.12**). Band alignments and efficient electron and

hole injections are enabled by the careful selection and integration of inorganic/organic materials for each layer.

The EL of PWQLEDs involves of three distinct peaks that match each monochromatic RGB EL. The EL location of PWQLEDs in Commission International de l'Eclairage coordinates is (0.39, 0.38) under 6 V bias, which indicates the emission of true-white light (Figure 2.9d). The EL spectra at different applied voltages are presented on Figure 2.9e. Furthermore, EL efficiencies are compared between PWQLEDs and mixed white QLEDs (MWQLEDs) in which the active layer is created by mixing RGB QDs in the solution phase. The brightness of PWQLEDs is enhanced over MWQLEDs by ~10% to ~52% depending on the applied voltage (Figure 2.9f), and the EQE of PWQLEDs is higher than that of MWQLEDs in entire operating voltage (Figure 2.9g).

For the better understanding of the enhanced performance of PWQLEDs, time-resolved PL measurements were conducted for QD layers employed in MWQLEDs and PWQLEDs (Figure 2.9h). The time-resolved PL of each RGB QD layer was also measured for the comparison. In MWQLEDs, the carrier lifetime of blue and green QDs considerably decreases, while that of red QDs increases, which implies the energy transfer between QDs.^[53,54] Because QDs with different band gaps are adjacent to each other in the close-

packed (mixed) layer, they transfer energy to neighbouring QDs with lower energy band gaps instead of emitting photons. The energy transfer between QDs of the same colour is neglected for analysis. In PWQLEDs, on the contrary, the carrier lifetime of pixelated QD arrays does not change from that of individual RGB QDs. These results demonstrate that the geometrical separation of pixelated configurations effectively suppresses the energy transfer process, enabling highly efficient true-white emission.

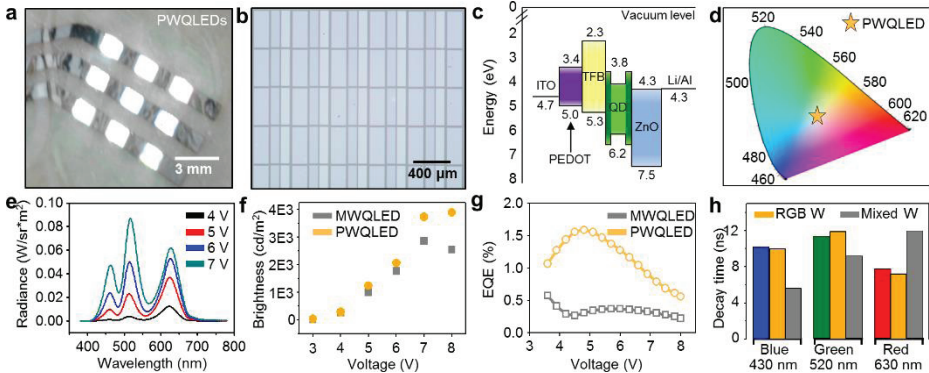


Figure 2.9. True white light emission based on pixelated RGB QLEDs. (a) Optical images of the wearable white QLEDs under the bias. (b) Magnified view (PL image) of the RGB QD pixels of white QLEDs. (c) Energy band diagram of white QLEDs estimated by ultraviolet photoelectron spectrometry. (d) CIE 1931 x-y chromaticity diagram showing the true-white colour (0.39, 0.38) of PWQLEDs. (e) EL spectra of pixelated white QLEDs (PWQLEDs) under various applied voltage. (f) Brightness versus voltage of PWQLEDs and MWQLEDs. PWQLEDs show the higher efficiency than MWQLEDs, particularly at the high brightness. (g) External quantum efficiency of PWQLEDs and mixed white QLEDs (MWQLEDs). (h) Time-resolved PL decay time of aligned RGB (PWQLED), mixed (MWQLED), and monochromatic (R, G, and B) QD layers.

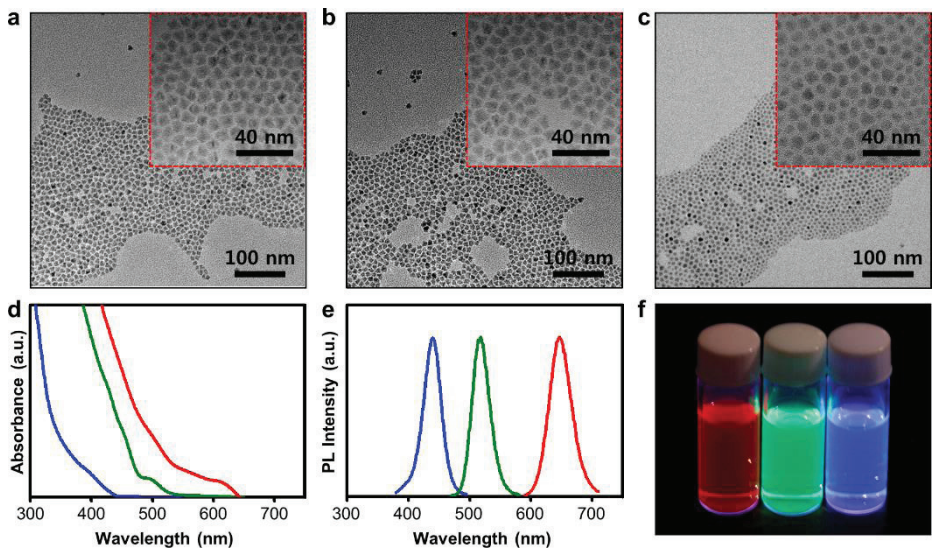


Figure 2.10. Characteristics of CdSe-based R/G/B QDs. (a–c) The TEM images of the red CdSe/CdS/ZnS QDs (a), green CdSe/ZnS QDs (b), and blue CdSe/ZnS QDs (c). Insets show the high-resolution TEM images. (d) Absorption spectra of RGB QDs. (e) The EL spectra of RGB QDs. (f) Photograph of the RGB QD solution under UV excitation.

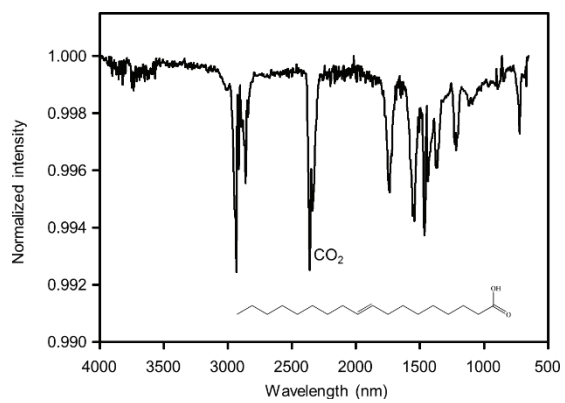


Figure 2.11. FTIR characterization of CdSe/ZnS alloyed QDs. The FTIR peaks match with the oleate ligands on the surface of the QDs.

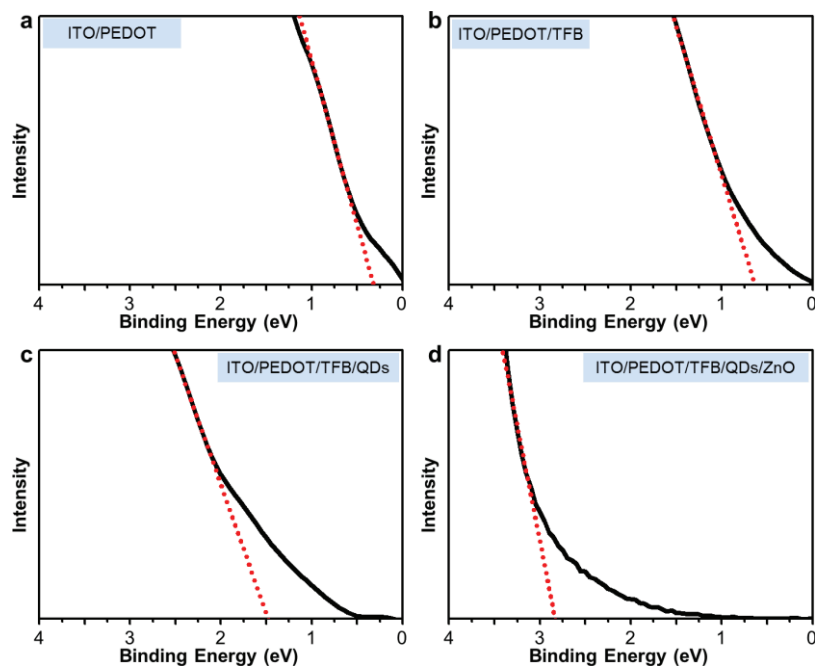


Figure 2.12. UV photoelectron spectra of layer materials employed in QLEDs. (a-d) The HOMO or valance band maximum of each layer is determined by the edge of the low-binding energy region in UPS spectra: (a) ITO/PEDOT, (b) ITO/PEDOT/TFB, (c) ITO/PEDOT/TFB/QDs, and (d) ITO/PEDOT/TFB/QDs/ZnO.

2.3.3 Electronic Tattoos based on Ultrathin, Wearable QLEDs

The current QLED technologies are applied in electronic tattoo demonstrations (**Figure 2.13**). Ultrathin form factors (total thickness of ~2.6 μm , including ~300-nm-thick active and ~1.1- μm -thick encapsulation layers; inset of Figure 2.13a) enable various deformations and conformal integrations with soft, curvilinear epidermal tissues.^[2,7] The detailed device structures and the magnified view of active layers (electron transport layer (ETL), QDs, and hole transport layer (HTL)) are shown in Figure 2.13a and b, respectively. The ultrathin encapsulation consists of a Parylene-C and epoxy bilayer. Electronic tattoos show outstanding device performances, such as a high brightness of 14,000 cd m⁻² at a driving voltage of 7 V and EQE of 2.35% at 4.5 V bias (*J-V-L* characteristics, Figure 2.13c). The electronic tattoo exhibits EQE above 1% in the range of 3.6 – 6.9 V applied voltages (current density: 3.4 – 1132 mA cm⁻²) as shown in **Figure 2.14a**. To the best of our knowledge, the brightness is higher than the previously reported values of the wearable LEDs at the same driving voltage.^[6,10,14,15] The high device performance at the low driving voltage, which can be obtained by commercial mobile batteries, is particularly beneficial to wearable device applications. The high EL performance remains stable after 1,000 cycles of uniaxial stretching (~20% applied strain, Figure 2.13d). For stretching tests, ~20% pre-strain, which is similar with the skin

stretchability,^[7] is applied to ultrathin QLEDs to form a wavy structure.^[9]

Moreover, as shown in Figure 2.14b, the lifetime of electronic tattoo is about 41.7 h at 3 mA applied current (initial brightness = 4554 cd m^{-2}), which corresponds to device lifetime of 12815 h at 100 cd m^{-2} (lifetime \times initial brightness^{1.5} = constant).^[20] Furthermore, these ultrathin QLEDs can be laminated on various curvilinear substrates, such as the crumpled Al foil, human skin, round glass, metal can, and sharp edges of a slide glass (Figure 2.13e–h, Figure 2.15a–d). Various deformations, such as bending, folding, or crumpling, as well as moistures (water droplets) do not cause mechanical/electrical damages or any decrease in the EL performance (Figure 2.13e–h, Figure 2.15e).

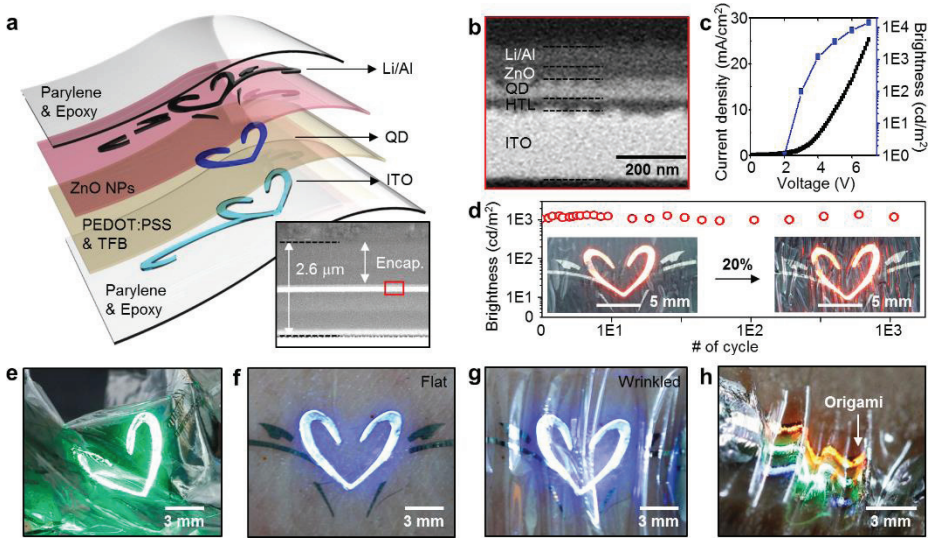


Figure 2.13. Electronic tattoo demonstrations using ultrathin wearable QLEDs. (a) Exploded view of the electronic tattoo. The inset is a cross-sectional SEM image. (b) Magnified view of the cross-sectional SEM image (inset of Fig. 4a) that shows the detailed layer information of active layers. (c) The $J-V-L$ characteristics of the ultrathin, wearable QLEDs. (d) Stable brightness in multiple stretching experiments ($\sim 20\%$, 1,000 times). The inset shows photographs of buckled and stretched ultrathin red QLEDs (0% and $\sim 20\%$, left and right). (e) Optical image of ultrathin green QLEDs laminated on crumpled Al foil. (f-g), Photographs of the electronic tattoo (blue QLEDs) laminated on the human skin (f). The wearable QLEDs maintain the original optoelectronic performances even under skin deformations (g). (h) Optical image of wearable PWQLED arrays laminated on the human skin.

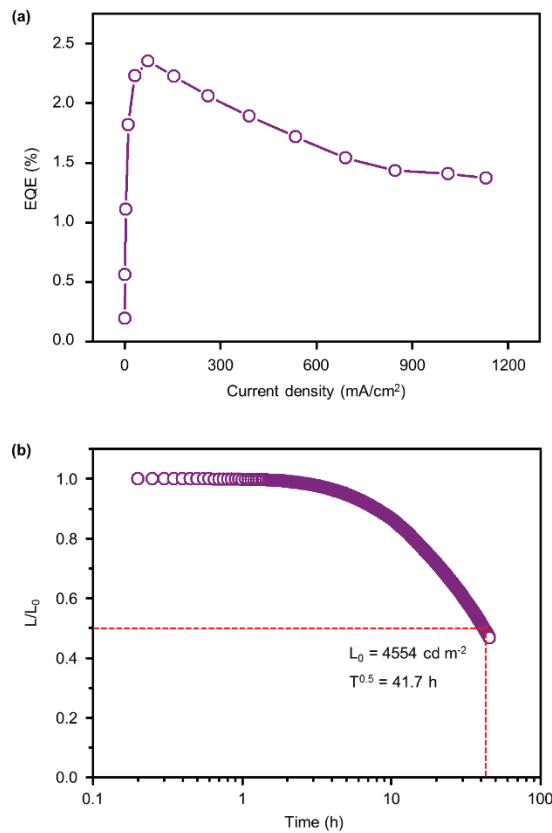


Figure 2.14. Device characteristics of wearable electronic tattoo. (a) External quantum efficiency (EQE) versus current density. (b) Lifetime characteristics. At the initial luminance of 4554 cd m^{-2} , the half-lifetime is 41.7 h under constant current operation (3 mA) at room temperature.

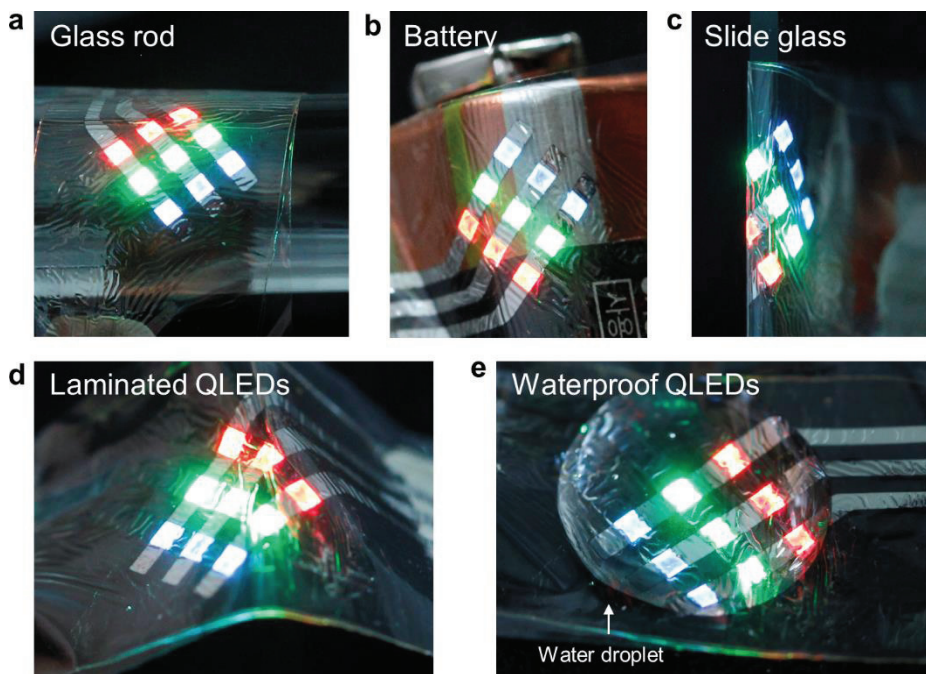


Figure 2.15. Ultrathin QLEDs on various curvilinear substrates. (a–c)
Photographs of the ultrathin and wearable QLED arrays on the curved surface of the glass rod (a), the battery (b), and the edge of the slide glass (c). (d) laminated freestanding wearable QLEDs. (e) Waterproof wearable QLEDs.

2.4 Conclusion

In conclusion, we demonstrate ultrathin, wearable RGB LED arrays fabricated using colloidal QDs and high resolution intaglio transfer-printing technology. This novel pixel-defining technique achieves the 60K ultra-high definition (UHD) RGB resolution (based on 40-inch flat panels). High-efficiency true-white QLED arrays as well as electronic tattoo applications demonstrate versatile utilities of the current work. These state-of-art devices can be laminated on various soft and curvilinear surfaces without diminishing the high EL efficiency. The current progress will realize high-definition full-colour deformable QLEDs and enable design variations in emerging wearable electronics.

* The contents of this chapter were published in Nature Communication (2015, 6, 7149).

References

- [1] S. Xu, Y. Zhang, L. Jia, K. E. Mathewson, K.-I. Jang, J. Kim, H. Fu, X. Huang, P. Chava, R. Wang, S. Bhole, L. Wang, Y. J. Na, Y. Guan, M. Flavin, Z. Han, Y. Huang, J. A. Rogers, *Science* **2014**, 344, 70.
- [2] M. Kaltenbrunner, T. Sekitani, J. Reeder, T. Yokota, K. Kuribara, T. Tokuhara, M. Drack, R. Schwödiauer, I. Graz, S. Bauer-Gogonea, S. Bauer, T. Someya, *Nature* **2013**, 499, 458.
- [3] D. Son, J. Lee, S. Qiao, R. Ghaffari, J. Kim, J. E. Lee, C. Song, S. J. Kim, D. J. Lee, S. W. Jun, S. Yang, M. Park, J. Shin, K. Do, M. Lee, K. Kang, C. S. Hwang, N. Lu, T. Hyeon, D.-H. Kim. *Nat. Nanotechnol.* **2014**, 9, 397.
- [4] D. J. Lipomi, M. Vosgueritchian, B. C-K. Tee, S. L. Hellstrom, J. A. Lee, C. H. Fox, Z. Bao, *Nat. Nanotechnol.* **2011**, 6, 788.
- [5] S. Pimputkar, J. S. Speck, S. P. DenBaars, S. Nakamura, *Nat. Photon.* **2009**, 3, 180.
- [6] R.-H. Kim, D.-H. Kim, J. Xiao, B. H. Kim, S.-I. Park, B. Panilaitis, R. Ghaffari, J. Yao, M. Li, Z. Liu, V. Malyarchuk, D. G. Kim, A.-P Le, R. G. Nuzzo, D. L. Kaplan, F. G. Omenetto, Y. Huang, Z. Kang, J. A. Rogers, *Nat. Mater.* **2010**, 9, 929.
- [7] D.-H. Kim, N. Lu, R. Ma, Y.-S. Kim, R.-H. Kim, S. Wang, J. Wu, S. M.

- Won, H. Tao, A. Islam, K. J. Yu, T.-i Kim, R. Chowdhury, M. Ying, L. Xu, M. Li, H.-J. Chung, H. Keum, M. McCormick, P. Liu, Y.-W. Zhang, F. G. Omenetto, Y. Huang, T. Coleman, J. A. Rogers, *Science* **2011**, 333, 838.
- [8] T.-i. Kim, J. G. McCall, Y. H. Jung, X. Huang, E. R. Siuda, Y. Li, J. Song, Y. M. Song, H. A. Pao, R.-H. Kim, C. Lu, S. D. Lee, I.-S. Song, G. Shin, R. Al-Hasani, S. Kim, M. P. Tan, Y. Huang, F. G. Omenetto, J. A. Rogers, M. R. Bruchas, *Science* **2013**, 340, 211.
- [9] S.-I. Park, Y. Xiong, R.-H. Kim, P. Elvikis, M. Meitl, D.-H. Kim, J. Wu, J. Yoon, C.-J. Yu, Z. Liu, Y. Huang, K.-c. Hwang, P. Ferreira, X. Li, K. Choquette, J. A. Rogers, *Science* **2009**, 325, 977.
- [10] M. S. White, M. Kaltenbrunner, E. D. Głowacki, K. Gutnichenko, G. Kettlgruber, I. Graz, S. Aazou, C. Ulbricht, D. A. M. Egbe, M. C. Miron, Z. Major, M. C. Scharber, T. Sekitani, T. Someya, S. Bauer, N. S. Sariciftci, *Nat. Photon.* **2013**, 7, 811.
- [11] J. Liang, L. Li, X. Niu, Z. Yu, Q. Pei, *Nat. Photon.* **2013**, 7, 817.
- [12] Z. Yu, X. Niu, Z. Liu, Q. Pei, *Adv. Mater.* **2011**, 23, 3989.
- [13] T.-H. Han, Y. Lee, M.-R. Choi, S.-H. Woo, S.-H. Bae, B. H. Hong, J.-H. Ahn, T.-W. Lee, *Nat. Photon.* **2012**, 6, 105.
- [14] T. Sekitani, H. Nakajima, H. Maeda, T. Fukushima, T. Aida, K. Hata, T.

- Someya, *Nat. Mater.* **2009**, 8, 494.
- [15] C. Wang, D. Hwang, Z. Yu, K. Takei, J. Park, T. Chen, B. Ma, A. Javey, *Nat. Mater.* **2013**, 12, 899.
- [16] R. H. Friend, R. W. Gymer, A. B. Holmes, J. H. Burroughes, R. N. Marks, C. Taliani, D. D. C. Bradley, D. A. Dos Santos, J. L. Brédas, M. Lögdlund, W. R. Salaneck, *Nature* **1999**, 397, 121.
- [17] V. L. Colvin, M. C. Schlamp, A. P. Alivisatos, *Nature* **1994**, 370, 354.
- [18] S. Coe, W.-K. Woo, M. G. Bawendi, V. Bulović, *Nature* **2002**, 420, 800.
- [19] Y. Shirasaki, G. J. Supran, M. G. Bawendi, V. Bulović, *Nat. Photon.* **2013**, 7, 13.
- [20] X. Dai, Z. Zhang, Y. Jin, Y. Niu, H. Cao, X. Liang, L. Chen, J. Wang, X. Peng, *Nature* **2014**, 515, 96.
- [21] K.-S. Cho, E. K. Lee, W.-J. Joo, E. Jang, T.-H. Kim, S. J. Lee, S.-J. Kwon, J. Y. Han, B.-K. Kim, B. L. Choi, J. M. Kim, *Nat. Photon.* **2009**, 3, 341.
- [22] L. Sun, J. J. Choi, D. Stachnik, A. C. Bartrik, B.-R. Hyun, G. G. Malliaras, T. Hanrath, F. W. Wise, *Nat. Nanotech.* **2012**, 7, 369.
- [23] W. K. Bae, Y.-S. Park, J. Lim, D. Lee, L. A. Padilha, H. McDaniel, I. Robel, C. Lee, J. M. Pietryga, V. I. Klimov, *Nat. Commun.* **2013**, 4, 2661.
- [24] J. Joo, H. B. Na, T. Yu, J. H. Yu, Y. W. Kim, F. Wu, J. Z. Zhang, T. Hyeon, *J. Am. Chem. Soc.* **2003**, 125, 11100.

- [25] J. H. Yu, X. Liu, K. E. Kweon, J. Joo, J. Park, K.-T. Ko, D. W. Lee, S. Shen, K. Tivakornasasithorn, J. S. Son, J.-H. Park, Y.-W. Kim, G. S. Hwang, M. Dobrowolska, J. K. Furdyna, T. Hyeon, *Nat. Mater.* **2010**, 9, 47.
- [26] S. Coe-Sullivan, *Nat. Photon.* **2009**, 3, 315.
- [27] D. V. Talapin, J.-S. Lee, M. V. Kovalenko, E. V. Shevchenko, *Chem. Rev.* **2010**, 110, 389.
- [28] A. P. Alivisatos, *Science* **1996**, 271, 933.
- [29] N. Tessler, V. Medvedev, M. Kazes, S. Kan, U. Banin, *Science* **2002**, 295, 1506.
- [30] Z. Chen, B. Nadal, B. Mahler, H. Aubin, B. Dubertret, *Adv. Funct. Mater.* **2014**, 24, 295.
- [31] I. Mekis, D. V. Talapin, A. Kornowski, M. Haase, H. Weller, *J. Phys. Chem. B* **2003**, 107, 7454.
- [32] J. M. Caruge, J. E. Halpert, V. Wood, V. Bulović, M. G. Bawendi, *Nat. Photon.* **2008**, 2, 247.
- [33] W.-K. Koh, S. R. Saudari, A. T. Fafarman, C. R. Kagan, C. B. Murray, *Nano Lett.* **2011**, 11, 4764.
- [34] D. K. Kim, Y. Lai, B. T. Diroll, C. B. Murray, C. R. Kagan, *Nature Commun.* **2012**, 3, 1216.
- [35] Q. Sun, Y. A. Wang, L. S. Li, D. Wang, T. Zhu, J. Xu, C. Yang, Y. Li, *Nat.*

Photon. **2007**, *1*, 717.

- [36] J. Kwak, W. K. Bae, D. Lee, I. Park, J. Lim, M. Park, H. Cho, H. Woo, D. Y. Yoon, K. Char, S. Lee, C. Lee, *Nano Lett.* **2012**, *12*, 2362.
- [37] L. Qian, Y. Zheng, J. Xue, P. H. Holloway, *Nat. Photon.* **2011**, *5*, 543.
- [38] B. S. Mashford, M. Stevenson, Z. Popovic, C. Hamilton, Z. Zhou, C. Breen, J. Steckel, V. Bulović, M. Bawendi, S. Coe-Sullivan, P. T. Kazlas, *Nat. Photon.* **2013**, *7*, 407.
- [39] S. Coe-Sullivan, J. S. Steckel, W.-K. Woo, M. G. Bawendi, V. Bulović, *Adv. Func. Mater.* **2005**, *15*, 1117.
- [40] W. K. Bae, J. Kwak, J. Lim, D. Lee, M. K. Nam, K. Char, C. Lee, S. Lee, *Nano Lett.* **2010**, *10*, 2368.
- [41] L. Kim, P. O. Anikeeva, S. A. Coe-Sullivan, J. S. Steckel, M. G. Bawendi, V. Bulović, *Nano Lett.* **2008**, *8*, 4513.
- [42] T.-H. Kim, K.-S. Cho, E. K. Lee, S. J. Lee, J. Chae, J. W. Kim, D. H. Kim, J.-Y. Kwon, G. Amaratunga, S. Y. Lee, B. L. Choi, Y. Kuk, J. M. Kim, K. Kim, *Nat. Photon.* **2011**, *5*, 176.
- [43] T.-H. Kim, D.-Y. Chung, J. Ku, I. Song, S. Sul, D.-H. Kim, K.-S. Cho, B. L. Choi, J. M. Kim, S. Hwang, K. Kim, *Nat. Commun.* **2013**, *4*, 2637.
- [44] A. Rizzo, M. Mazzeo, M. Palumbo, G. Lerario, S. D’Amone, R. Cingolani, G. Gigli, *Adv. Mater.* **2008**, *20*, 1886.

- [45] C. Pacholski, A. Kornowski, H. Weller, *Angew. Chem., Int. Ed.* **2002**, 41, 1188.
- [46] J. Joo, H. B. Na, T. Yu, J. H. Yu, Y. W. Kim, F. Wu, J. Z. Zhang, T. Hyeon, *J. Am. Chem. Soc.* **2003**, 125, 11100.
- [47] J. Yang, J.-Y. Kim, J. H. Yu, T.-Y. Ahn, H. Lee, T.-S. Choi, Y.-W. Kim, J. Joo, M. J. Ko, T. Hyeon, *Phys. Chem. Chem. Phys.* **2013**, 15, 20517.
- [48] Y. Li, A. Rizzo, R. Cingolani, G. Gigli, *Adv. Mater.* **2006**, 18, 2545.
- [49] P. O. Anikeeva, J. E. Halpert, M. G. Bawendi, V. Bulović, *Nano Lett.* **2007**, 7, 2196.
- [50] H. S. Jang, H. Yang, S. W. Kim, J. Y. Han, S.-G. Lee, D. Y. Jeon, *Adv. Mater.* **2008**, 20, 2696.
- [51] Y. Zhang, C. Xie, H. Su, J. Liu, S. Pickering, Y. Wang, W. W. Yu, J. Wang, Y. Wang, J.-i. Hahm, N. Dellas, S. E. Mohney, J. Xu, *Nano Lett.* **2011**, 11, 329.
- [52] E. Jang, S. Jun, H. Jang, J. Lim, B. Kim, Y. Kim, *Adv. Mater.* **2010**, 22, 3076.
- [53] C. R. Kagan, C. B. Murray, M. Nirmal, M. G. Bawendi, *Phys. Rev. Lett.* **1996**, 76, 3043.
- [54] S. A. Crooker, J. A. Hollingsworth, S. Tretiak, V. I. Klimov, *Phys. Rev. Lett.* **2002**, 89, 186802.

Chapter 3. Temperature controlled, patterned graphene transfer printing for transparent and wearable electronic/optoelectronic system

3.1 Introduction

As transparent and wearable electronics are under spotlights, diverse nanoscale materials, such as carbon nanomaterials, ultrathin inorganic nano-ribbons/membranes, and nanowire composites, have been intensively studied.^[1,2] Particularly among them, graphene has received significant attentions due to its uniquely beneficial properties including mechanical flexibility, optical transparency, high conductivity/carrier mobility, and thermal responsiveness.^[3-5] Various individual graphene-based devices (*e.g.*, transistors,^[6-8] memory devices,^[9] light-emitting diodes (LEDs),^[10,11] optical^[12] and mechanical^[13,14] sensors, electrical^[15] and thermal^[16] actuators, and cell culture devices^[17]) have been demonstrated. The ultimate goal of this research trend is the integration of diverse graphene-based electronic/optoelectronic devices toward multifunctional all-graphene electronic systems, *i.e.*, a well-organized array of graphene devices interconnected by graphene electrodes.^[18,19] However, the photolithographical patterning and oxygen

plasma etching of graphenes on pre-formed graphene passive/active components and/or other functional electronic materials/units are limited by several processing hurdles.^[20-23] A viable route for the goal is to organize/integrate multiple stacks of patterned graphene device components by using the aligned transfer printing technique.^[24,25]

High-quality graphene, which is synthesized on metal foils using the chemical vapor deposition,^[26,27] is typically transferred onto target substrates using thermal release tapes^[28] or through scooping method with sacrificial polymer layers,^[29-33] such as poly(methylmethacrylate) (PMMA),^[30,31] polystyrene (PS),^[32] and polyisobutylene (PIB).^[33] These methods have been successfully applied in large-scale graphene transfer procedures.^[27,28, 34] Recently novel direct transfer printing methods using electrochemical delamination^[35] or static electricity^[36] have been proposed and demonstrated significantly low sheet resistance and high quality graphene surface by eliminating contaminations from organic/inorganic residues. Many challenges still exist, however, in multiple aligned transfer of graphene patterns and device components onto pre-patterned ones. Transfer printing using the elastomeric polydimethylsiloxane (PDMS) stamp^[37] has been successfully demonstrated to selectively pick up inorganic^[38-41] and metal nanomembranes,^[42] nanoparticles,^[43] and carbon nanotubes^[44] and position them on pre-registered target locations. However, in

spite of these advances, the multiple transfer of patterned graphene using elastomeric stamps on diverse substrates has remaining challenges to achieve high-quality interfaces, micrometer-range alignments, and high success rates (*i.e.*, yields).

Here, a simple but effective aligned transfer printing process of patterned graphene device components is developed. Key advancements are in the use of designed thermal treatment sequences as well as viscoelastic sacrificial polymers with elastomeric stamps for the efficient patterned graphene transfer. The heating and cooling protocol results in the dramatic increase of the transfer yield (from ~27% to ~90%) in comparison with conventional procedures (method without thermal treatments). The proposed high-fidelity multiple transfer printing technique along with in-depth understanding of related materials and mechanics in processes and device designs enables the transparent and wearable all-graphene multifunctional electronic system.

3.2 Experimental Section

3.2.1 Graphene Synthesis

To synthesize the graphene using the chemical vapor deposition (CVD) process, a 25- μm -thick copper foil (Alfa Aesar, USA) was used. The Cu foil was annealed at 1,000°C for 30 min in CVD under a constant hydrogen flow (8 sccm, 0.08 Torr), followed by an additional methane gas flow (20 sccm, 1.6 Torr) for 30 min. After the synthesis process was complete, the chamber was rapidly cooled to room temperature using the hydrogen gas flow (8 sccm, 0.08 Torr).

3.2.2 Other Materials used for Experiments

To create the graphene-PDMS stamp, poly(methylmethacrylate) (PMMA A4, MicroChem, USA), acetone (Samchun Chemical, Republic of Korea), copper etchant (FeCl_3 , Trasene, USA), positive photoresists, S1805, AZ5214, and AZ4620 (AZ Electronics Materials, USA), a polydimethylsiloxane base and curing agent (PDMS, Sylgard 184, Dow Corning, USA), polyisobutylene (PIB, Sigma Aldrich, USA), and decane (Samchun Chemical, Republic of Korea) were utilized. To fabricate the epidermal graphene devices, SU-8 2 (MicroChem, USA) and SU-8 2000.5 (MicroChem, USA) were used for encapsulation.

3.2.3 “Heating and Cooling” Transfer Printing of Patterned Graphene

Monolayer graphene was synthesized using the chemical vapor deposition procedure.^[21] The graphene film was doped with the Au salt and stacked on another graphene film on a Cu foil in order to control the conductivity (details are in the Supporting Information). After adjusting the graphene resistance, the stacked graphene layers on the Cu foil were patterned using photolithography and O₂ plasma etching. The patterned graphene was spin coated with a PIB solution (30 mg ml⁻¹ in n-decane solvent, Aldrich, USA), and annealed at 100°C for 1 min so as to vaporize the decane (Samchun Chemical, Republic of Korea). A 10-mm-thick PDMS elastomer stamp (Sylgard 184, Dow Corning, USA) was then put into conformal contact with the PIB layer. The Cu/graphene/PIB/PDMS structure was immersed in the FeCl₃ solution in order to dissolve the Cu foil, and was then washed with deionized water and dried at room temperature. Then, the graphene/PIB/PDMS assembly was aligned on the target transfer printing location. To increase the interfacial adhesion, the sample was heated on a hotplate at 100°C for 10 min, followed by cooling at -20°C for 30 min. In the final stage of the transfer printing process, the PDMS stamp was gently detached from the substrate and the PIB layer was removed using pure decane. A Raman spectrum of graphene film was analyzed using T64000

(Horiba, Japan) at NCIRF and the AFM measurement was performed in the tapping mode (Dimension iCON, Bruker, Germany).

3.2.4 Measurement of Transparency and Sheet Resistance

The transparency was measured using ~550-nm visible light and a Cary series UV-Vis-NIR spectrophotometer (Agilent Technologies, USA). The sheet resistance was measured using a CMT-series 4-point probe (Advanced Instrument Technology, Republic of Korea).

3.2.5 Measurement of Interfacial Energy by Peel Test

A 30 μm thick PIB layer is coated on a 50 μm thick PET substrate to prevent elongation of PIB during the peel test. The PDMS thickness (Young's modulus $\sim 19.8 \text{ MPa}$) is scaled down to 300 μm (the PDMS thickness used in thermally controlled transfer printing is $\sim 8 \text{ mm}$) to retain flexibility during the peel test. The peeling angle of two laminated layer (PIB/PDMS or PIB/PET) is fixed to 90°, and the width of layer is fixed to 20 mm.

3.2.6 Fabrication of Stretchable Graphene Devices

A 50-nm-thick nickel layer was deposited on a silicon substrate as a sacrificial layer using thermal evaporation. An encapsulation layer (SU-8 2) was spin-cast

on the Ni layer at 3,000 rpm for 30 s, soft-cured at 65°C for 1 min, and hard-cured at 95°C for 1 min. The encapsulation layer was photolithographically patterned and fully cured at 150°C for 30 min. The doped graphene film was then transferred onto the SU8-2 film and photolithographically patterned and etched using O₂ plasma. This process was used to pattern all of the interconnections of the all-graphene circuit. Pre-patterned graphene layers for graphene sensors and actuators (e.g., strain gauges and heaters) were precisely aligned and transferred onto the graphene interconnection pre-patterns through the transfer printing process with “heating and cooling” thermal treatments. The SU8-2 top encapsulation layer was spin-coated and patterned and Ag paste was utilized to the pad for external wiring. 30:1 PDMS was spin-cast at 1,000 rpm for 30 s, followed by curing at 130°C for 10 min. After the PDMS was fully cured, the sacrificial Ni layer was etched in Ni etchant and the graphene circuit was transferred/laminated on the human skin.

3.2.7. Fabrication of Graphene Anode based Wearable Quantum Dot LEDs

Graphene layer was transferred onto the ultrathin PET substrates (4.5 μm), doped with Au ion (10 mM in nitromethane), and successfully patterned by O₂ plasma. After cleaning substrates with acetone and isopropyl alcohol (IPA), (3-

aminopropyl)triethoxysilane (APTES) was treated onto the substrates for 20 min in order to modify the surface. Poly(3,4-ethylenedioxythiophene):poly(styrenesulfonate) (PEDOT:PSS, PH1000) layers were then spin-coated on substrates and annealed at 120°C for 10 min. The PEDOT:PSS-coated substrates were transferred into a Ar-filled glove box for deposition of additional layers. Poly[(9,9-diethylfluorenyl-2,7-diyl)-co-(4,4'-(N-(4-sec-butylphenyl))diphenylamine)] (TFB), quantum dots (QD) and ZnO nanocrystal (NC) layers were spin-coated layer by layer at 2,000 rpm for 30s. Each layers were annealed at 150°C for 30 min after spin-coating. Lithium-aluminum alloy electrodes (70 nm) were then deposited by thermal evaporation at a high vacuum condition ($\sim 8 \times 10^{-7}$ torr) through a shadow mask. Finally, the devices were encapsulated by epoxy (SU8-2) layers for protection.

3.2.8 Wireless Communication System

The custom-made wireless communication system equipped on the smart band was built. It consists of a controller, Bluetooth unit (Arduino Pro Mini, Sparkfun, USA), and battery (Figure S8). The medical devices on mSC patches were connected to the external commercial devices (e.g. tablets or smartphones) wirelessly through Bluetooth module of the smart band. Data was transferred to external devices from mSC patches and commands were

delivered vice versa. For instance, the resistance change of strain gauges was measured through the specially designed resistor-capacitor (RC) circuit. The resistance alternation modulated the discharging time of capacitor, which was detected by the controller unit and wirelessly transferred to external devices through Bluetooth unit. A Labview (National Instruments, USA) program analyzed the RC delay and changed over to original resistance values. The program also monitored the motion of high-risk patients, such as tremors, and sent alarms in emergency situations. Another program installed in controller unit can remotely turn on/off the iontophoresis actuator by using smartphone applications (SPLDuino Lite, Helloapps, USA).

3.2.9 Laboratory Animals

Balb/c nude mice (age: 6 weeks) were obtained from the Experimental Animal Center, Chuncheon Center, Korea Basic Science Institute (KBSI), Chuncheon, South Korea. These animals were individually housed in transparent plastic cages with wire grid covers under controlled temperatures (22-24°C) with the 12 hour light/dark cycle (lights on from 08:00 to 20:00). All animal procedures were in accordance with the Guide for the Care and Use of Laboratory Animals issued by the Laboratory Animal Resources Commission of KBSI. The Institutional Animal Care and Use Committee at the KBSI

(KBSI-AEC1409) reviewed and approved this study. All of the experiments were conducted to minimize the number of animals used and the suffering caused by the procedures used in the current study.

3.3 Result and Discussion

3.3.1 Representative Multifunctional System based on Wearable Graphene Devices

A representative example of multifunctional integrated system based on wearable graphene electronic/optoelectronic devices fabricated through the thermally controlled transfer printing process is illustrated in **Figure 3.1**. The multi-stacked and stretchable graphene devices (sensors, actuators, and LEDs) are conformally laminated on the human skin and connected to a smart band that contains a controller, a power-supply module, and a wireless data transmission unit (Figure 3.1a). The ultrathin thickness of graphene circuits in addition to meandering device designs enables the high stretchability.^[45,46] The portable, invisible, and multifunctional features of this wearable system enlists many applications. One application scenario in the personalized healthcare, for example, is as follows. Integrated sensors monitor bio-signals of the user (*e.g.*, activity and/or tremor) in real-time (Figure 3.1b). The collected information is wirelessly transmitted to the external smart devices (*e.g.*, smartphone) through a Bluetooth module in the smart band (Figure 3.1a). When acute, abnormal conditions are to be notified to the user, the quantum dot (QD) LEDs are turned on (Figure 3.1c). Electrical and thermal actuators (iontophoresis electrodes and heater) effectively induce feedback transdermal drug delivery and/or thermal

physiotherapy (Figure 3.1d and e). The feedback actuation can be remotely controlled through a custom-made Android application.

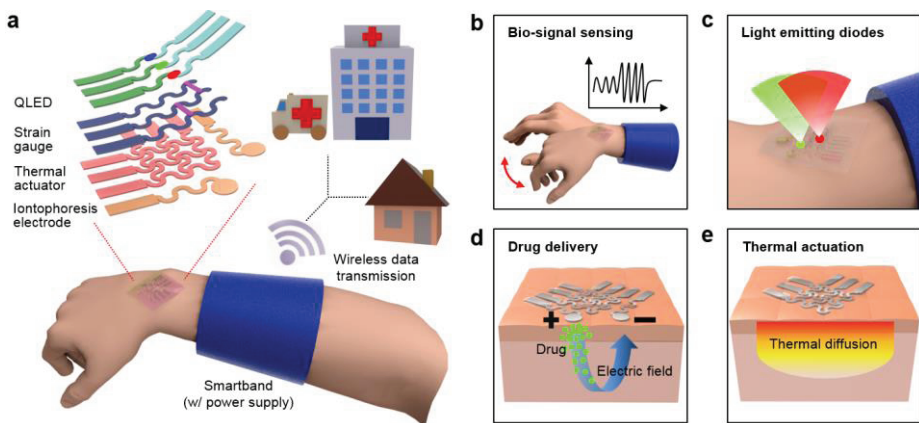


Figure 3.1. Schematic illustrations of the wearable and transparent graphene electronic/optoelectronic system. (a) Exploded view of stacked graphene devices and system integration. **(b-e)** Multiple functions of the integrated wearable system; sensing bio-signals (b), showing alarms through light emitting diodes (c), transdermal drug delivery (d), and thermal therapy (e).

3.3.2 Fabrication of Thermally Controlled Patterned Graphene Transfer

Figure 3.2 is a schematic diagram of the thermally controlled, aligned transfer printing process of graphene patterns. The insets are optical camera images of graphene layers at each step; note that the transparent graphene patterns are colorized for ease of viewing. First, non-patterned graphene monolayers are stacked on the graphene grown on the Cu foil using the conventional transfer method^[26,27] to adjust the resistance of the graphene layers.^[16] The resulting resistance-controlled multi-stacked graphene is photolithographically patterned so that the desired features/designs are obtained. Then, the patterned graphene is coated with a viscoelastic sacrificial layer of poly-isobutylene (PIB)^[33] and conformal contact is made with the PDMS stamp. FeCl₃ solution is used to chemically etch the Cu foil and releases the graphene/PDMS stamp. After the etching solution is washed away, the graphene-holding stamp is aligned to make a contact with the target substrates and/or pre-patterned graphene layers. To increase the interfacial adhesion, the contacted system (stamp/patterned-graphene/substrate) is heated to 100°C. Subsequent cooling to -20°C and returning to room temperature complete the transfer process. During the low-temperature stage, the thermal expansion coefficient mismatch between the PIB and PDMS focuses the mechanical stress at the edge of the PIB/PDMS interface, which enables easy separation of the

PDMS stamp from the patterned-graphene on the substrate and thereby increases the transfer yield. After the transfer printing, the PIB sacrificial layer is removed using the decane solution.

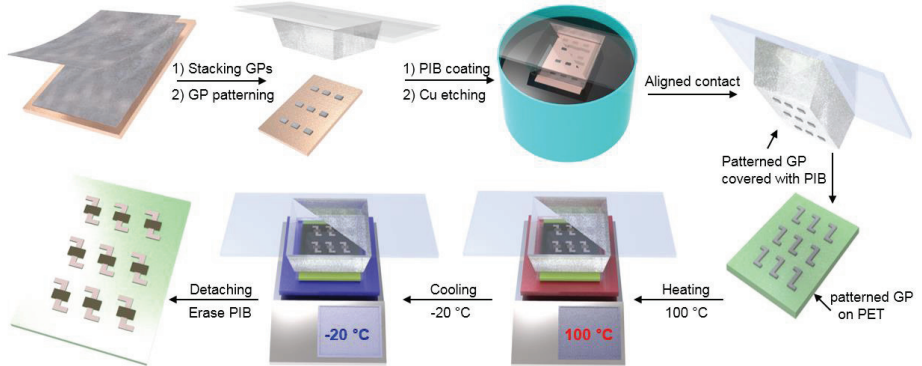


Figure 3.2. Schematic illustration of the thermally controlled transfer printing process.

3.3.3 Effect of thermal treatment during graphene transfer printing

We statistically analyzed the influence of different thermal treatment sequences on the yield of transfer printing by using ~400 patterned graphene samples. We used samples of an array of square patterns (size: $300 \times 300 \mu\text{m}^2$).

Figure 3.3a summarizes the obtained transfer printing yields at various thermal treatment conditions. As demonstrated in the previous reports,^[20,21,27,28,34] large-area graphene patterns/films are easily transferred on desired substrates because of the strong van der Waals force between graphene and receiving substrates. However, as the graphene pattern size decreases, which is necessary for high-density electronics and optoelectronics, the van der Waals force decreases dramatically.^[47] Since the adhesion force between graphene and target substrates is smaller than that between PIB and PDMS at room temperature in particular, small graphene patterns are easily delaminated from the receiving substrates during the retrieval process of the PDMS stamp (Figure 3.3b and c). The designed thermal treatment sequences overcome this problem. We compared representative optical microscope images of thermally treated graphene layers at different temperature sequences (see Figure 3.3c–e for transfer printing at room temperature, after heating, and after heating-cooling, respectively). To show the differences in each transfer printing process more clearly, images of the graphene samples were collected before the removal of

the PIB. Due to thermal treatments, the transfer yield increases from 27% (no treatment) to 78% (heating only) and to 90.5% (heating-cooling). This thermally controlled transfer printing technique can be applied over the large area (size: 5 cm × 5 cm; **Figure 3.4**, inset shows the magnified view) on an ultrathin PET substrate (thickness: ~4.5 μm) of various surface properties (from hydrophilic to superhydrophobic surfaces; **Figure 3.5**).

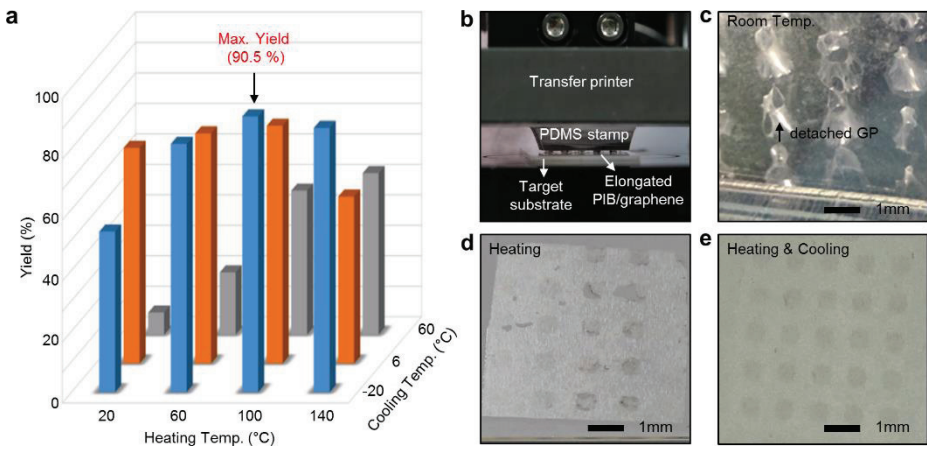


Figure 3.3. Experimental evaluation of “heating and cooling” sequences.

(a) Effects of different thermal treatment sequences on the transfer printing yield. **(b)** Optical camera image of the failed graphene transfer printing without the thermal treatment (at room temperature). **(c–e)** Graphene layers transferred by using PIB (c) at room temperature, (d) after heating treatment, and (e) after heating and cooling treatment.

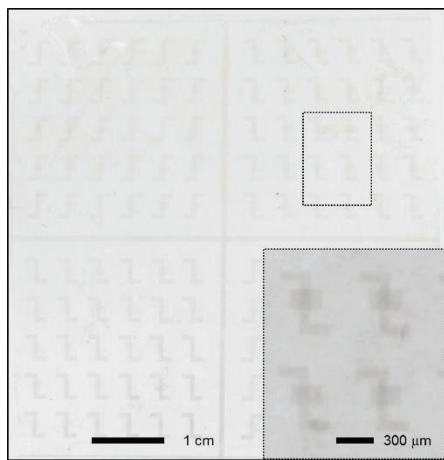


Figure 3.4. Large-area transfer printing of graphene patterns. Inset (dotted box) shows the magnified image of graphene patterns.

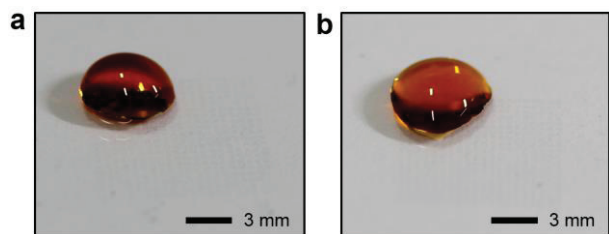


Figure 3.5. Graphene patterns transferred on the (a) hydrophilic and (b) superhydrophobic surface.

3.3.4 Mechanism Study of the Thermally Controlled Graphene Transfer Process

A detailed theoretical analysis of the mechanism behind the thermally controlled graphene transfer process was conducted, based on the experimental data shown in **Figure 3.6**. The PDMS, PIB, and glass substrate have different thermal expansion behaviors, as shown in Figure 3.6a. These differences in thermal expansion properties result in a thermal expansion mismatch, which causes a stress build-up between the layers in response to temperature changes. In addition, PIB exhibits quite large viscoelasticity (Figure 3.6a), which affects the amount of induced stress. The stress relaxation in PIB was measured at 20°C (black dots), 60°C (blue dots), and 100°C (red dots), as shown in Figure 3.6b. From a theoretical perspective, the relaxation modulus can be described by a series of exponential decaying functions

$$G(t) = \sum_{i=1}^4 w_i \exp\left[-\left(\frac{t}{\tau_i}\right)\right], \quad (1)$$

where $G(t)$ is the relaxation modulus at time t , w_i is the weighting factor ($\sum_{i=1}^4 w_i = 1$), and τ_i is the relaxation time. If the viscosity follows the Arrhenius dependence on the temperature, the shift factor ψ is given by

$$\psi = \exp\left(\frac{H}{R}\left(\frac{1}{T_R} - \frac{1}{T}\right)\right), \quad (2)$$

where H is the activation enthalpy for stress relaxation, R is the universal gas constant, T_R is the reference temperature (100°C in this analysis), and T is the current temperature. The reduced time ξ is defined by the shift factor as

$$\xi = \int_0^t \psi(t') dt' = \int_0^t \exp\left(\frac{H}{R}\left(\frac{1}{T_R} - \frac{1}{T(t')}\right)\right) dt'. \quad (3)$$

The stress relaxation at different temperatures can be represented by replacing t with ξ in Equation (1). The model parameters are obtained from the stress relaxation data. Figure 3.6b shows the fitted results for the data obtained at 20°C (black line), 60°C (blue line), and 100°C (red line), along with a prediction for -20°C (dark green line). At 100°C, 90 % of the applied stress was found to be relaxed after 1,200 s, whereas only 20 % is expected to be relaxed at -20°C. The thermally controlled graphene transfer process utilizes this difference in the stress relaxation during the thermal cycle.

The role of the thermal cycle in the development of the thermal stress at the edge of the PIB/PDMS interface, which is a critical factor for easy separation of the PDMS stamp from the patterned-graphene/substrate, was examined by using a thermo-mechanical finite element simulation (Figure 3.6c

and d). The PDMS/PIB/PET substrate structure was modeled by two-dimensional plane strain elements. Because the analysis was focused on the PDMS/PIB interface, the graphene between the PIB and PET substrate was ignored. Linear elasticity and linear thermal expansion were assumed for the PDMS and the PET substrate, whereas the viscoelasticity model was used for the PIB (Figure 3.6c). To determine the effect of the viscoelasticity on the thermal stress, the results for the elastic PIB were also calculated (Figure 3.6d). As the interfacial stress is strongly affected by modulus and thickness, we experimentally obtained modulus (**Table 3.1**) and thickness (Figure 3.6a) of PIB and PDMS layers at various temperatures. The initial temperature of the finite element model was set to 20°C. As the temperature increases from 20 to 100°C (heating), the thermal strain mismatch between the layers instantly generates shear stresses, as seen on the left of Figure 3.6c. After a 10-min period at a fixed temperature of 100°C, the majority of the stress was relaxed (Figure 3.6c, middle), as expected from Figure 3.6b. When the sample was cooled to -20°C, a large shear stress was developed at the PDMS/PIB interface (Figure 3.6c, bottom), promoting easy separation of the materials during the transfer process. The shear stress developed at the PIB/PET interface does not lead to separation due to the strong adhesion between PIB and substrate according to the experimental results. Note that, if PIB is elastic, holding the temperature at

100°C does not cause the developed stress to relax (Figure 3.6d, top and middle) and cooling to -20°C leaves only a small amount of shear stress (Figure 3.6d, bottom).

Furthermore, we directly compared the effect of sequential thermal treatments in the interfacial energy of PIB/PDMS and PIB/PET using a peel test. After the heating and cooling thermal treatment, the relative adhesion force of PIB/PDMS is ~14% decreased and that of PIB/PET is ~200% increased. The detailed results are shown in **Figure 3.7**.

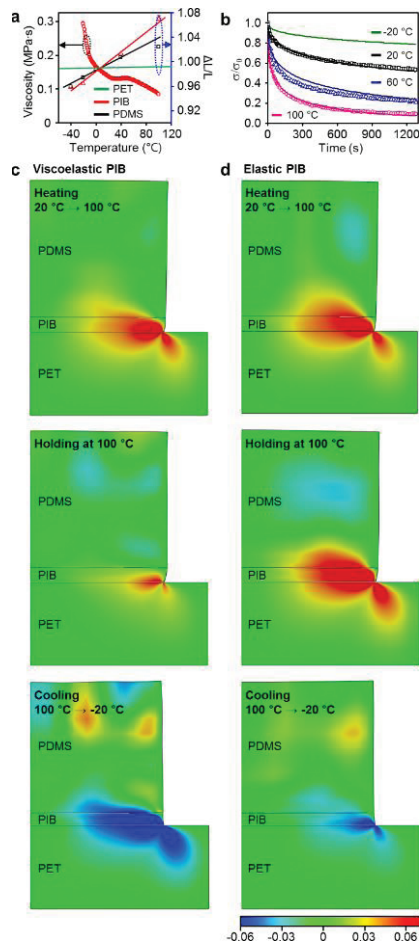


Figure 3.6. Simulation of the elastic and viscoelastic behaviors of PDMS, PIB, and PET layers during the thermal treatment. (a) Temperature dependence of PIB viscosity and thermal expansion behavior of PDMS, PIB, and PET. **(b)** Stress relaxation of PIB at various temperatures (dot: measured data, line: model prediction). **(c, d)** FEM-predicted shear stress in PDMS, PIB, and PET substrate after heating from 20 to 100°C, holding for 10 min, and cooling to -20°C. The viscoelasticity (c) and linear elasticity (d) models were used for PIB.

Table 3.1. Young's modulus of PIB and PDMS.

Temperature (°C)	Young's modulus (MPa) of PIB	Young's modulus (MPa) of PDMS
100	0.878	4.623
60	1.057	3.340
20	1.574	4.185
-20	1.866 (extrapolated)	5.029 (extrapolated)

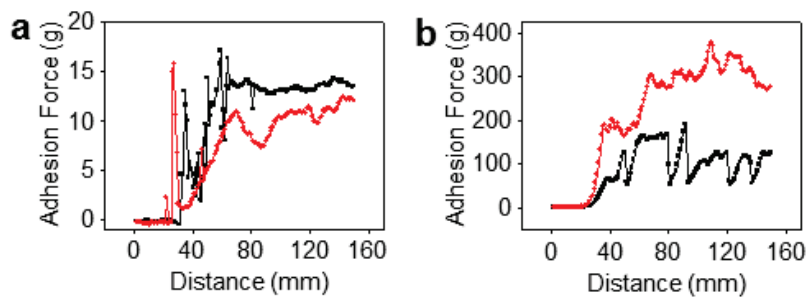


Figure 3.7. Peel test of PIB/PDMS, PIB/PET interfaces. (a) Adhesion force of PIB/PDMS interface with (red) and without (black) heating and cooling thermal treatment. **(b)** Adhesion force of PIB/PET interface with (red) and without (black) heating and cooling thermal treatment.

3.3.5 Characteristics of Transferred Graphene Patterns

To validate the quality of graphene patterns/stacks fabricated through the thermally controlled multiple transfer printing process, we examined their optical and electrical properties through various material characterization methods. Imaging using atomic force microscopy (AFM) confirms the integrity and quality of the transferred graphene surface (**Figure 3.8a**). The AFM phase image presents the pure graphene layer without organic residues (Figure 3.8b). Raman spectroscopy analysis (Figure 3.8c) shows the high intensity at the typical G-band for the graphene monolayer with the minimal one at the defect band. The 2D Raman mapping analysis (area: $280 \mu\text{m} \times 220 \mu\text{m}$) confirms the uniform and high quality surface of graphene prepared by thermally controlled transfer printing method (**Figure 3.9**).

The thermally controlled transfer printing technique readily forms various resistance/transparency distributions (Figure 3.8d-g). A graphene pattern with different electrical and optical properties can be achieved using the proposed transfer printing technique (see Figure 3.8e–g for its optical image, sheet resistance, and transparency, respectively). Figure 3.8d summarizes various sheet resistances and transparencies of multi-stacked graphene layers. By stacking Au doped graphene layers and/or hybridizing with Ag nanowires, the graphene sheet resistance can be controlled from ~ 60 to $\sim 1500 \Omega/\square$, which

corresponds to ~80% to ~95% transparency. The minimum resolution of the thermally controlled transfer printing was 5 μm in our experiment. 5 μm grid patterns, spaced with 25 μm , 50 μm , 100 μm , and 200 μm , were successfully transfer-printed (**Figure 3.10**). This patterned graphene transfer printing can be applied to various substrates including the PDMS substrate with various modulus (from 20 kPa to 2 MPa; Figure 3.8h). Figure 3.8i shows the variety of examples of the multi-stacked aligned graphene patterns (i: flower and sparrow, ii: 3-legs-traditional-bird, and iii: partially overlapped heater patterns).

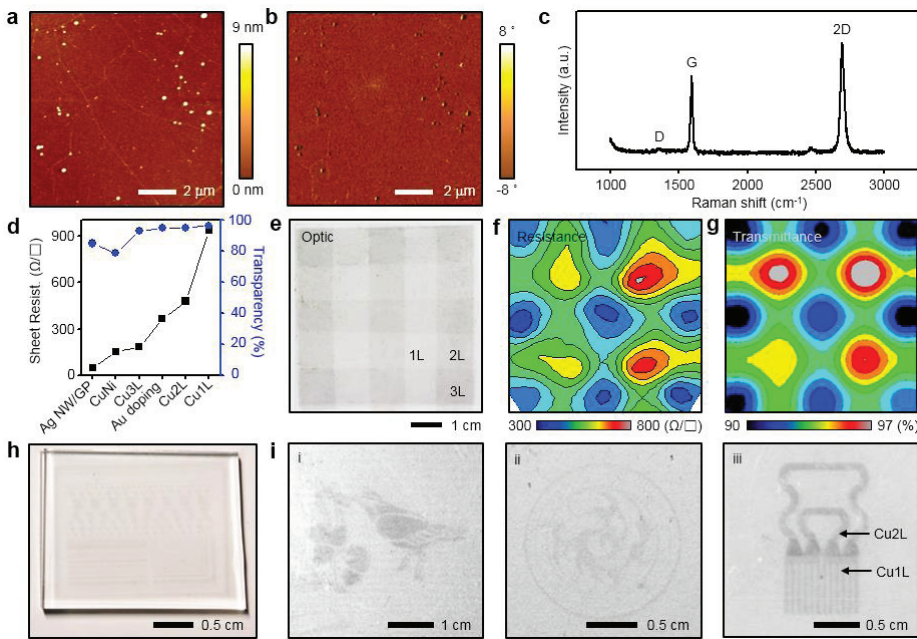


Figure 3.8. Electrical and optical properties of transferred graphene patterns. (a, b) Atomic force microscopy: (a) height image and (b) phase image of graphene patterns transferred onto 300-nm-thick SiO₂ substrate. (c) Raman spectrum from thermally controlled transfer-printed graphene layer. (d) Sheet resistance and transparency of various resistance-controlled graphene layers. (e) Optical image of a stacked graphene pattern. (f) Areal distribution of sheet resistance and (g) transparency. (h) Optical image of the transferred graphene pattern on the PDMS substrate. (i) Various multi-stacked graphene patterns.

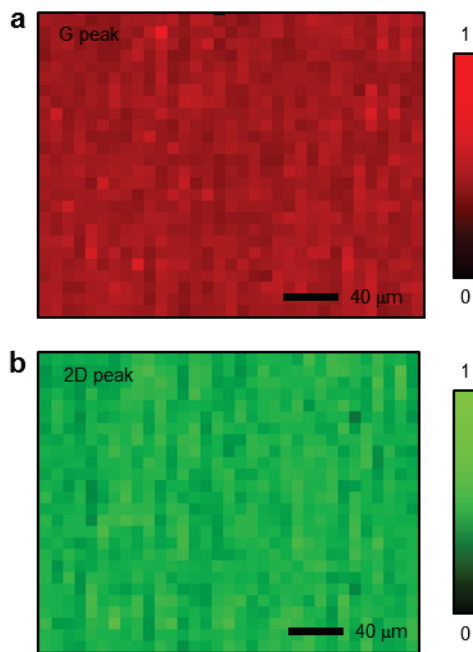


Figure 3.9. Large scale 2D Raman mapping analysis. (a,b) Raman mapping data of G peak (a) and 2D peak (b) of graphene layer (area: 280 $\mu\text{m} \times 220 \mu\text{m}$).

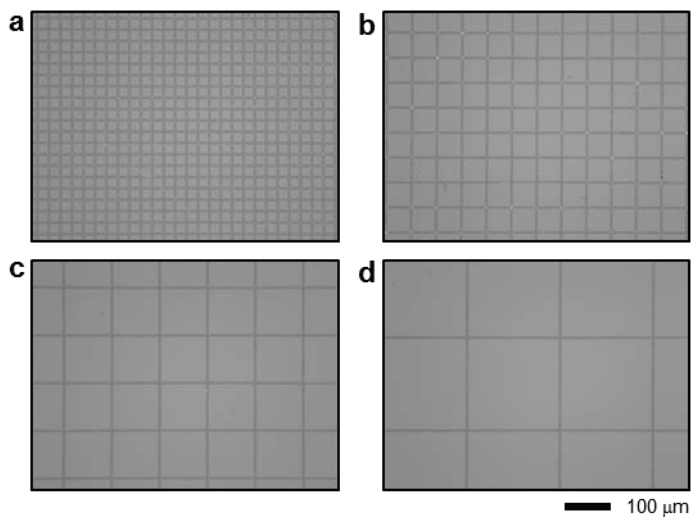


Figure 3.10. Optic images of high resolution graphene patterns transferred by our thermally controlled transfer printing technique. (a-d) 5 μm grid patterns are spaced with 25 μm (a), 50 μm (b), 100 μm (c), and 200 μm (d), respectively.

3.3.6 Integrated wearable graphene sensors and actuators

This thermally controlled transfer printing technique can be applied to various device fabrications. Graphene-based sensors and actuators (temperature sensor, strain gauge, and thermal actuator) on a flexible PET substrate, for example, are demonstrated. The resistance of the fabricated temperature sensor varies linearly at different temperatures, with a sensitivity of $\sim 30 \Omega ^\circ\text{C}^{-1}$. The gauge factor of the graphene strain gauge is found to be ~ 2.1 . The resistance of the sensing unit is designed ~ 50 times greater than that of the interconnection. Therefore, the resistance changes of sensors induced by variations in the temperature and external strain are significantly higher than those of the interconnection, which maximizes the sensitivity.

Integration of individual devices together with a custom-made smart band enables a transparent and wearable sensor and actuator with the wireless data transmission and control. The wearable system is designed to be conformally laminated on the human skin, which maximizes the sensor sensitivity and feedback actuation efficiency. The resulting array fabricated via the thermally controlled transfer printing is shown in **Figure 3.11a** and b (inset of Figure 3.11b shows the magnified view). The graphene devices are connected by graphene electrodes and encapsulated by transparent, ultrathin ($< \sim 1 \mu\text{m}$) epoxy layers (SU8-2, MicroChem, USA). The graphene devices are

located on the neutral mechanical plane to dissipate the bending-induced strain. The intrinsic softness of the graphene enhances the mechanical reliability of the system further.^[48] The strain gauge in the integrated system successfully monitors human physical activity or tremor by characterizing joint movements. Figure 3.11c shows the cyclic fatigue test result which exhibits no performance changes over 1,000 times of bending (bending radius \sim 500 μm). The ultrathin (overall thickness $<$ \sim 2 μm) and stretchable design helps to maintain the robust contact between devices and soft human skin without delamination and thereby the signal to noise ratio is relatively high. Figure 3.11d shows the wearable graphene heater on human arm. The graphene wearable system is connected to the smart-band,^[49] which includes the power supply, control, and wireless communication module (Figure 3.11e and f and **Figure 3.12** for representative wireless experimental setup image, schematic circuit diagram of the smart band, and its image, respectively). The tremor signals measured by the strain gauge,^[43] for instance, are wirelessly transmitted to the external electronic devices (*e.g.*, smartphone and/or tablet) via Bluetooth. Figure 3.11g shows the transmitted signals to the external computer after the noise filtering.

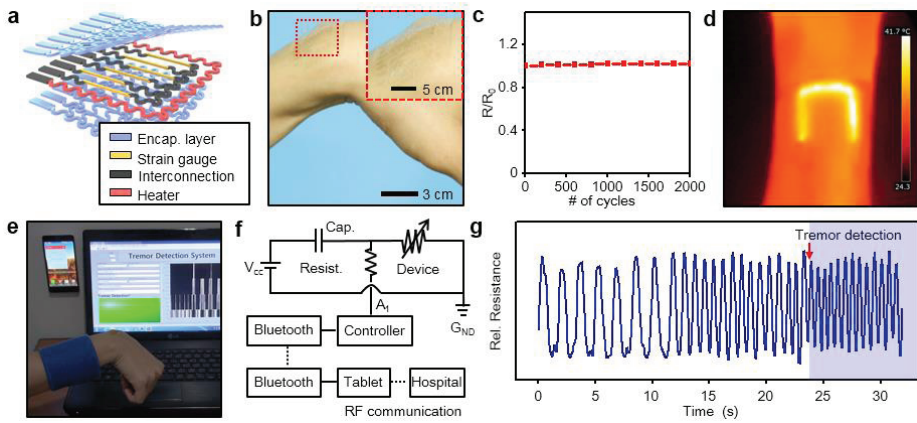


Figure 3.11. Integrated wearable sensors and actuators. **(a)** Exploded illustration of the wearable sensors and actuators. **(b)** Optical image of the graphene electronic system conformally laminated on the wrist, which corresponds to Figure 7a. Inset shows the magnified view. **(c)** Relative resistance change during the cyclic bending test. **(d)** IR image of epidermal heater on human arm. **(e)** Image of the wireless tremor detection system and **(f)** its schematic circuit diagram. **(g)** Wirelessly transmitted motion and tremor signals after the noise filtering.

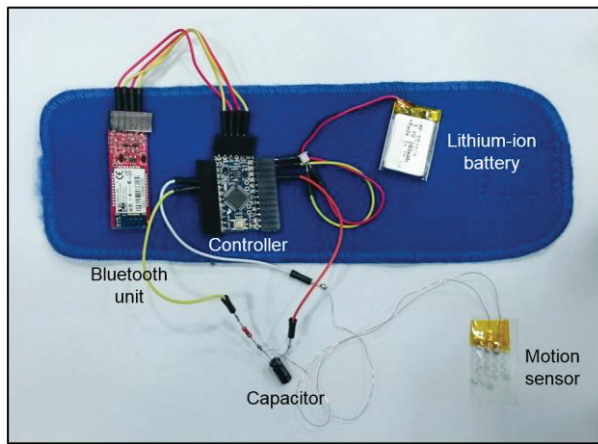


Figure 3.12. Optical camera image of a custom-made smart band which consists of a Bluetooth unit, power source (lithium-ion battery), and controller unit.

3.3.7 Wearable Quantum Dot LED with the Graphene Anode

The information display is another important component in the electronic/optoelectronic system to provide signals and/or alarms to the user. The graphene electrode can be used for wearable quantum dot LEDs (QLEDs).^[47] An emergency alarm, for example, can be displayed to the user through the skin-mounted QLEDs. QLEDs have many advantages, such as the color purity, air/water stability, ultra-thinness, and cost-effectiveness, and become an emerging candidate for the flexible and stretchable display. Despite recent advances in QLED technologies, accomplishing deformable QLEDs is a daunting goal due to poor mechanical deformability of ITO anodes. By virtue of the transparency and flexibility of the graphene electrodes, wearable QLEDs could be fabricated (**Figure 3.13**). The exploded illustration (Figure 3.13a) provides the layer information and inset images show wearable QLEDs on the human arm. The QLEDs are stacked on top of the wearable sensors and actuators. The semi-transparent Li/Al alloy cathodes are shown, while the graphene anodes are invisible. Figure 3.13b shows the band structure of the QLED including the anode and cathode, hole and electron transporting layer, and light emitting layer. Current density and brightness at various applied voltages ($J-V-L$ performance) and electroluminescence efficiency (EQE) of the QLEDs are presented in Figure 3.13c and d, respectively. The wearable QLEDs

are operated with a commercial micro-battery (Figure 3.12) by virtue of their low required power consumption. Bending deformations up to 180° do not change the QLED performance (Figure 3.13e).

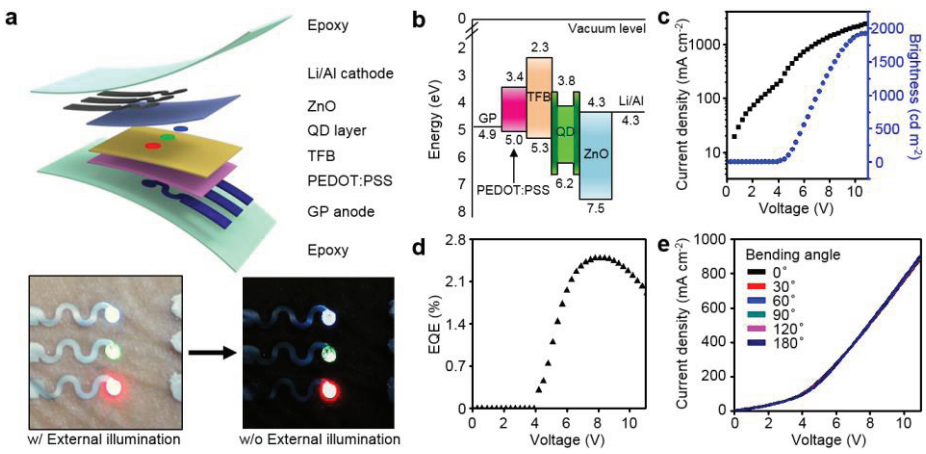


Figure 3.13. Wearable QLED with the graphene anode. (a) Exploded illustration of the wearable QLED. The insets at the bottom show corresponding images of the QLED laminated on the human arm with (left) and without (right) the external illumination. (b) Energy band diagram of the QLED. (c) J - V - L characteristics and (d) external quantum efficiency of the wearable QLED. (e) Stable J - V characteristics of the QLED at various bending angles (from 0° to 180°).

3.3.8 Graphene based Wearable Thermal/Electrical Actuators for Transdermal therapy

Feedback actuators in relation to the sensing are crucial to complete the loop of sensing and actuation.^[43] **Figure 3.14** shows the representative example, a wirelessly controlled feedback actuation for the thermal therapy^[50] (by heaters) and the transdermal drug delivery^[43,51] (by iontophoresis electrodes) in response to the measured data from integrated sensors (Figure 3.14a). Thermal energy diffusion from graphene heaters to dermal and vascular tissues near the wrist is shown in Figure 3.14b (infrared and optical camera image in the left and right frame). Thermal therapy is a widely-used physical treatment.^[48] The conformal lamination of the heater on the skin maximizes the heat transfer and physiotherapy efficiency. Note that the time-dependent thermal actuation properties of the graphene heater is similar with that of devices based on other transparent electrodes, such as an indium-tin-oxide (Figure 3.14c). Figure 3.14d shows repetitive on-off cycles of the heater (1 min period), presenting the stable and fast heating property. Another feedback actuation, transdermal drug delivery, is performed by using the local electric field formed by iontophoresis electrodes. Figure 3.14e shows the laminated iontophoresis electrodes on the skin of a nude mouse. Polar drugs (doxorubicin, Aldrich, USA) loaded on graphene electrodes are delivered through the skin

and into the bloodstream by the applied electric field. The transdermal drug diffusion is fast and without any pain. The penetration depth can be easily tuned by controlling the stimuli number. The confocal image shows that the penetration depth of the drug is proportional to the number of applied iontophoresis stimuli (Figure 3.14f-h).

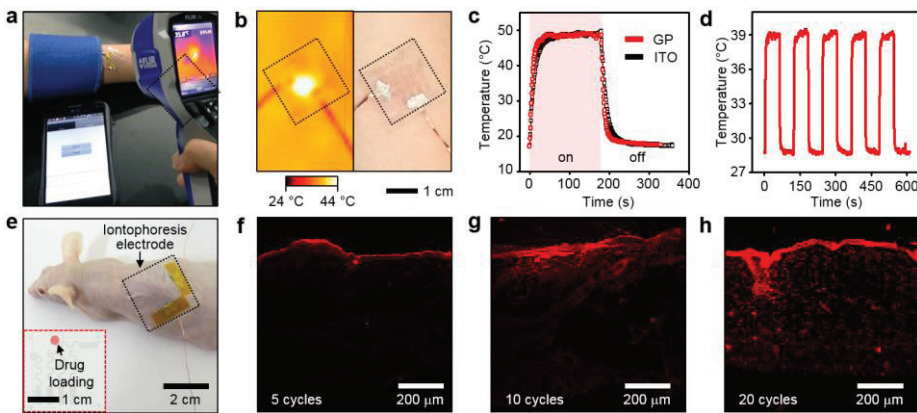


Figure 3.14. Feedback thermal and electrical actuators. (a) Wirelessly controlled graphene thermal actuator using a custom-made smartphone application. (b) IR (left) and optical (right) image of the graphene heater laminated on the skin. (c) Comparison of thermal responses of transparent heaters made of graphene (GP) and indium-titanium-oxide (ITO). (d) Cyclic thermal stimulations. (e) Image of transdermal drug delivery on the mouse skin using graphene iontophoresis electrodes. Inset shows the drug-loaded iontophoresis electrodes. (f-h) Cross-sectional confocal microscope images showing transdermal drug delivery of doxolubicin (red) through the mouse skin. The penetration depth is proportional to the number of electrical stimulation.

3.4 Conclusion

In summary, we report a thermally controlled transfer printing technique for the integration of patterned graphene devices. The designed “heating and cooling” thermal treatment process transfers patterned graphene layers intact on various substrates. Furthermore, aligned transfer printing allows the accurate integration of stretchable graphene electronic/optoelectronic devices in an ultrathin wearable platform. The resulting multifunctional wearable system is conformally laminated on the human skin to successfully carry out physiological sensing, wireless data transmission, signal display, thermal physiotherapy, and transdermal drug delivery, together with a custom-made smart band. These advances would provide new opportunities for all-graphene integrated systems.

* The contents of this chapter were published in Advanced Functional Materials (2015, 25, 7109).

References

- [1] D.-H. Kim, N. Lu, R. Ghaffari, J. A. Rogers, *NPG Asia Mater.* **2012**, *4*, e15.
- [2] T. Sekitani, H. Nakajima, H. Maeda, T. Fukushima, T. Aida, K. Hata, T. Someya, *Nature Mater.* **2009**, *8*, 494.
- [3] K. S. Novoselov, V. I. Fal'ko, L. Colombo, P. R. Gellert, M. G. Schwab, K. Kim, *Nature* **2012**, *490*, 192.
- [4] Q. Bao, K. P. Loh, *ACS Nano* **2012**, *6*, 3677.
- [5] D. H. Lee, J. Yi, J. M. Lee, S. J. Lee, Y.-J. Doh, H. Y. Jeong, Z. Lee, U. Paik, J. A. Rogers, W. I. Park, *ACS Nano* **2013**, *7*, 301.
- [6] W. H. Lee, J. Park, Y. Kim, K. S. Kim, B. H. Hong, K. Cho, *Adv. Mater.* **2011**, *23*, 3460.
- [7] T. Q. Trung, N. T. Tien, D. Kim, M. Jang, O. J. Yoon, N.-E. Lee, *Adv. Funct. Mater.* **2014**, *24*, 117.
- [8] T. Q. Trung, S. Ramasundaram, S. W. Hong, N.-E. Lee, *Adv. Funct. Mater.* **2014**, *24*, 3438.
- [9] X. Wang, W. Xie, J.-B. Xu, *Adv. Mater.* **2014**, *26*, 5496.
- [10] J.-T. Seo, J. Han, T. Lim, K.-H. Lee, J. Hwang, H. Yang, S. Ju, *ACS Nano* **2014**, *8*, 12476.

- [11] T.-H. Han, Y. Lee, M.-R. Choi, S.-H. Woo, S.-H. Bae, B. H. Hong, J.-H. Ahn, T.-W. Lee, *Nature Photon.* **2012**, 6, 105.
- [12] F. Xia, T. Mueller, Y.-m. Lin, A. Valdes-Garcia, P. Avouris, *Nature Nanotech.* **2009**, 4, 839.
- [13] S. H. Bae, Y. Lee, B. K. Sharma, H. J. Lee, J. H. Kim, J. H. Ahn, *Carbon* **2013**, 51, 236.
- [14] Y. Wang, L. Wang, T. Yang, X. Li, X. Zang, M. Zhu, K. Wang, D. Wu, H. Zhu, *Adv. Funct. Mater.* **2014**, 24, 4666.
- [15] S. Lim, D. Son, J. Kim, Y. B. Lee, J.-K. Song, S. Choi, D. J. Lee, J. H. Kim, M. Lee, T. Hyeon, D.-H. Kim, *Adv. Funct. Mater.* **2015**, 25, 375.
- [16] J. Kang, H. Kim, K. S. Kim, S.-K. Lee, S. Bae, J.-H. Ahn, Y.-J. Kim, J.-B. Choi, B. H. Hong, *Nano Lett.* **2011**, 11, 5154.
- [17] S. J. Kim, H. R. Cho, K. W. Cho, S. Qiao, J. S. Rhim, M. Soh, T. Kim, M. K. Choi, C. Choi, I. Park, N. S. Hwang, T. Hyeon, S. H. Choi, N. Lu, D.-H. Kim, *ACS Nano* **2015**, 9, 2677.
- [18] F. Withers, T. H. Bointon, M. F. Craciun, S. Russo, *ACS Nano* **2013**, 7, 5052.
- [19] S. Lee, K. Lee, C.-H. Liu, G. S. Kulkarni, Z. Zhong, *Nature Commun.* **2012**, 3, 1018.

- [20] D.-Y. Wang, I.-S. Huang, P.-H. Ho, S.-S. Li, Y.-C. Yeh, D.-W. Wang, W.-L. Chen, Y.-Y. Lee, Y.-M. Chang, C.-C. Chen, C.-T. Liang, C.-W. Chen, *Adv. Mater.* **2013**, *25*, 4521.
- [21] J. Kang, S. Hwang, J. H. Kim, M. H. Kim, J. Ryu, S. J. Seo, B. H. Hong, M. K. Kim, J.-B. Choi, *ACS Nano* **2012**, *6*, 5360.
- [22] W. Jung, D. Kim, M. Lee, S. Kim, J.-H. Kim, C.-S. Han, *Adv. Mater.* **2014**, *26*, 6394.
- [23] H. H. Kim, Y. Chung, E. Lee, S. K. Lee, K. Cho, *Adv. Mater.* **2014**, *26*, 3213.
- [24] S. J. Kang, B. Kim, K. S. Kim, Y. Zhao, Z. Chen, G. H. Lee, J. Hone, P. Kim, C. Nuckolls, *Adv. Mater.* **2011**, *23*, 3531.
- [25] A. Carlson, A. M. Bowen, Y. Huang, R. G. Nuzzo, J. A. Rogers, *Adv. Mater.* **2012**, *24*, 5284.
- [26] X. Li, W. Cai, J. An, S. Kim, J. Nah, D. Yang, R. Piner, A. Velamakanni, I. Jung, E. Tutuc, S. K. Banerjee, L. Colombo, R. S. Ruoff, *Science* **2009**, *324*, 1312.
- [27] K. S. Kim, Y. Zhao, H. Jang, S. Y. Lee, J. M. Kim, K. S. Kim, J.-H. Ahn, P. Kim, J.-Y. Choi, B. H. Hong, *Nature* **2009**, *457*, 706.

- [28] S. Bae, H. Kim, Y. Lee, X. Xu, J.-S. Park, Y. Zheng, J. Balakrishnan, T. Lei, H. R. Kim, Y. I. Song, Y.-J. Kim, K. S. Kim, B. Ozyilmaz, J.-H. Ahn, B. H. Hong, S. Iijima, *Nature Nanotechnol.* **2010**, 5, 574.
- [29] S. K. Lee, J. W. Yang, H. H. Kim, S. B. Jo, B. Kang, H. Bong, H. C. Lee, G. Lee, K. S. Kim, K. Cho, *ACS Nano* **2014**, 8, 7968.
- [30] J. W. Suk, A. Kitt, C. W. Magnuson, Y. Hao, S. Ahmed, J. An, A. K. Swan, B. B. Goldberg, R. S. Ruoff, *ACS Nano* **2011**, 5, 6916.
- [31] A. Reina, X. Jia, J. Ho, D. Nezich, H. Son, V. Bulovic, M. S. Dresselhaus, J. Kong, *Nano Lett.* **2009**, 9, 30.
- [32] E. H. Lock, M. Baraket, M. Laskoski, S. P. Mulvaney, W. K. Lee, P. E. Sheehan, D. R. Hines, J. T. Robinson, J. Tosado, M. S. Fuhrer, S. C. Hernandez, S. G. Walton, *Nano Lett.* **2012**, 12, 102.
- [33] J. Song, F.-Y. Kam, R.-Q. Png, W.-L. Seah, J.-M. Zhuo, G.-K. Lim, P. K. H. Ho, L.-L. Chua, *Nature Nanotechnol.* **2013**, 8, 356.
- [34] L. Gao, G.-X. Ni, Y. Liu, B. Liu, A. H. C. Neto, K. P. Loh, *Nature* **2014**, 505, 190.
- [35] X. Wang, L. Tao, Y. Hao, Z. Liu, H. Chou, I. Kholmanov, S. Chen, C. Tan, N. Jayant, Q. Yu, D. Akinwande, R. S. Ruoff, *Small* **2014**, 10, 694.
- [36] W. Jung, D. Kim, M. Lee, S. Kim, J.-H. Kim, C.-S. Han, *Adv. Mater.* **2014**, 26, 6394.

- [37] A. Carlson, A. M. Bowen, Y. Huang, R. G. Nuzzo, J. A. Rogers, *Adv. Mater.* **2012**, *24*, 5284.
- [38] J. Kim, M. Lee, H. J. Shim, R. Ghaffari, H. R. Cho, D. Son, Y. H. Jung, M. Soh, C. Choi, S. Jung, K. Chu, D. Jeon, S.-T. Lee, J. H. Kim, S. H. Choi, T. Hyeon, D.-H. Kim, *Nature Commun.* **2014**, *5*, 11.
- [39] H. Ko, K. Takei, R. Kapadia, S. Chuang, H. Fang, P. W. Leu, K. Ganapathi, E. Plis, H. S. Kim, S.-Y. Chen, M. Madsen, A. C. Ford, Y.-L. Chueh, S. Krishna, S. Salahuddin, A. Javey, *Nature* **2010**, *468*, 286.
- [40] S. Yang, E. Ng, N. Lu, *Extreme Mech. Lett.* **2015**, *2*, 37.
- [41] D. Chanda, K. Shigeta, S. Gupta, T. Cain, A. Carlson, A. Mihi, A. J. Baca, G. R. Bogart, P. Braun, J. A. Rogers, *Nature Nanotechnol.* **2011**, *6*, 402.
- [42] Y.-L. Loo, R. L. Willett, K. W. Baldwin, J. A. Rogers, *J. Am. Chem. Soc.* **2002**, *124*, 7654.
- [43] D. Son, J. Lee, S. Qiao, R. Ghaffari, J. Kim, J. E. Lee, C. Song, S. J. Kim, D. J. Lee, S. W. Jun, S. Yang, M. Park, J. Shin, K. Do, M. Lee, K. Kang, C. S. Hwang, N. Lu, T. Hyeon, D.-H. Kim, *Nature Nanotechnol.* **2014**, *9*, 397.
- [44] S. J. Kang, C. Kocabas, T. Ozel, M. Shim, N. Pimparkar, M. A. Alam, S. V. Rotkin, J. A. Rogers, *Nature Nanotech.* **2007**, *2*, 230.

- [45] M. Kaltenbrunner, T. Sekitani, J. Reeder, T. Yokota, K. Kuribara, T. Tokuhara, M. Drack, R. Schwödiauer, I. Graz, S. Bauer-Gogonea, S. Bauer, T. Someya, *Nature* **2013**, 499, 458.
- [46] D. P. J. Cotton, I. M. Graz, S. P. Lacour, *Sensors J, IEEE* **2009**, 9, 2008.
- [47] M. K. Choi, J. Yang, K. Kang, D. C. Kim, C. Choi, C. Park, S. J. Kim, S. I. Chae, T.-H. Kim, J. H. Kim, T. Hyeon, D.-H. Kim, *Nature Commun.* **2015**, 6, 7149.
- [48] Y. Wang, R. Yang, Z. Shi, L. Zhang, D. Shi, E. Wang, G. Zhang, *ACS Nano* **2011**, 5, 3645.
- [49] M. K. Choi, O. K. Park, C. Choi, S. Qiao, R. Ghaffari, J. Kim, D. J. Lee, M. Kim, W. Hyun, S. J. Kim, H. J. Hwang, S.-H. Kwon, T. Hyeon, N. Lu, D.-H. Kim, *Adv. Healthc. Mater.* **2016**, 5, 80.
- [50] S. Choi, J. Park, W. Hyun, J. Kim, J. Kim, Y. B. Lee, C. Song, H. J. Hwang, J. H. Kim, T. Hyeon, D.-H. Kim, *ACS Nano* **2015**, 9, 6626.
- [51] M. R. Prausnitz, R. Langer, *Nature Biotechnol.* **2008**, 26, 1261.

Chapter 4. Cephalopod-inspired Miniaturized Suction Cups for Smart Medical Skin

4.1 Introduction

Nature has inspired important advances in the design of mechanical/chemical adhesives.^[1-5] In particular, recent demonstrations of biomimetic dry adhesives based on gecko setae^[6-9] and chemical glues derived from shellfish proteins^[10] provide compelling routes for medical devices that must interface with skin and/or organs. The intimate interfacing is important,^[11,12] since it oftentimes determines the wearability^[13,14] and the quality of diagnosis and therapy.^[15-20] Capabilities for the multiple regeneration of adhesives and the biocompatibility upon detachment from target skin/organ surfaces require more advanced technologies. However, robust, conformal contacts between medical electronics/therapeutics and curvilinear, textured surfaces of dynamically contorting skin remain challenging with existing packaged electronics and encapsulation strategies.^[21-23]

Cephalopods (e.g. octopus, squid) provide an intriguing example in nature whereby the arrayed geometry of suction cups achieves robust and conformal adhesion without chemical adhesives.^[24] Here, we present

cephalopod-inspired miniaturized suction cup (mSC) dry adhesives that are combined with ultrathin stretchable electronics to create a new class of glue-free diagnosis and therapy system. The ultra-low modulus (~108 kPa) mSC array supports embedded stretchable electronics and drug-loaded therapeutic nanoparticles, while firmly laminating on skin without inducing skin irritations/damages during long-term usage and removal. The integrated system allows continuous monitoring of vital sign changes in various physiologic or pathophysiologic conditions, controllable release of drugs, and wireless communication from/to external devices for the remote healthcare. Strong van der Waals forces and negative pressure based on mSC structures create robust mechanical coupling with skin, which enables highly sensitive/accurate biometric sensing and effective transdermal drug delivery, while preserving the tackiness over many uses and drug reloading. These new adhesion features serve a powerful, low cost alternative to single use chemical adhesives.

A representative scenario in clinical applications is described in **Figure 4.1**, whereby the electronic patch is firmly laminated on skin and linked to a wrist band that contains a power supply, a controller, and short-range wireless data transmission unit (**Figure 4.2-4.4**). The mSCs (Figure 4.1c; atomic force microscopy (AFM) images) inspired by octopus tentacles (Figure 4.1b; optic (left) and 3D laser scanner (right) image) generate negative pressure,

which promote adherence to skin. The ultrathin form factor ($< 50 \mu\text{m}$) coupled with low system-level modulus ($\sim 108 \text{ kPa}$) provides comfort, enhanced skin integration, and breathability for daily wear. Integrated sensors (strain gauges, cardiac sensing electrodes, and temperature sensors) monitor physical activity, fine movement such as physiologic or pathologic tremors, and vital signs (e.g. body temperature, respiration, electrocardiogram, pulse, and blood pressure) (Figure 4.1a). The measured biosignals are wirelessly transmitted to external devices through a Bluetooth module located in the smart band (Figure 4.1d left). Acute changes and significant abnormalities of vital signs from a wide array of pathophysiologic conditions are detected with the electronic patch in real time. Alerts that signal the need for urgent medical attention or prevention of life-threatening clinical events can be broadcasted to emergency medical service providers through wireless networks (Figure 4.1d right). Iontophoresis electrode deliver electric fields through dermis to modulate transdermal delivery of drugs loaded in mesoporous silica (m-SiO₂) nanoparticles (inset of Figure 4.1a) by accelerating transport of ions and drug molecules (Figure 4.1e). Drugs can be reloaded periodically on the electronic patch (Figure 4.1f). This system offers a range of possibilities for mobile, point-of-care medical services.

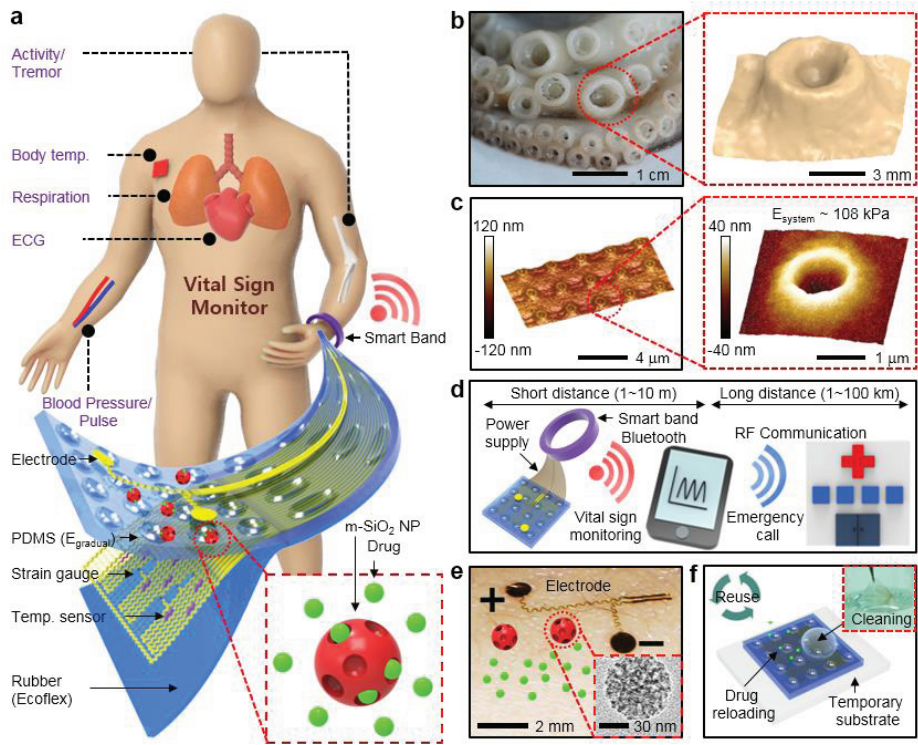


Figure 4.1. Overview of the electronic patch with bio-inspired dry adhesives. **(a)** Schematic illustration of the multifunctional miniaturized suction cup (mSC) electronic patch. Vital signs are monitored by electrodes, strain gauges, and temperature sensors. Drugs loaded in the mesoporous silica nanoparticles are transdermally delivered by iontophoresis. The mSC structures are located at the interface between the patch and skin as dry adhesives. The smart band (connected to the mSC patch) provides wireless functionalities and a power source. **(b)** Photograph of the cephalopod tentacle (left) and 3D laser scanning image of magnified suction cup (right). **(c)** 3D AFM image of mSC array (left) and magnified view (right). The dimension is sub-micrometer and system modulus is $\sim 108 \text{ kPa}$. **(d)** Schematic illustration of the wireless

communication system. Short distance wireless network (Bluetooth) and power supply units are included in the custom-made smart band. Vital signs are transferred to smart devices through Bluetooth and transmitted to remote healthcare centers through RF communication units. **(e)** Control of transdermal drug delivery rates wirelessly via iontophoresis. **(f)** The electronic patch is reused after cleaning (inset) and drug reloading.

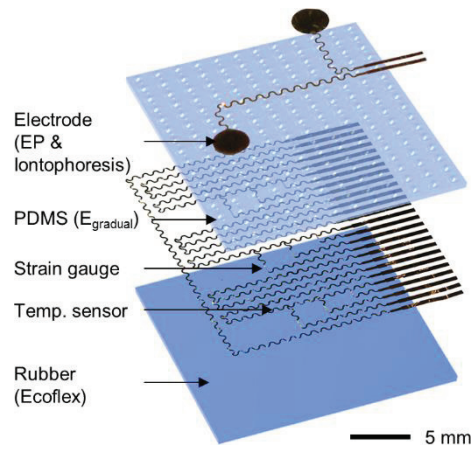


Figure 4.2. Exploded view of mSC electronic patch. The strain gauge and temperature sensor array (image in the middle) is embedded between silicone rubber (Ecoflex; cartoon at the bottom) and top mSCs structured elastomer layer (PDMS; cartoon at the top). The electrodes (topmost image) are located on the surface of the electronic patch.

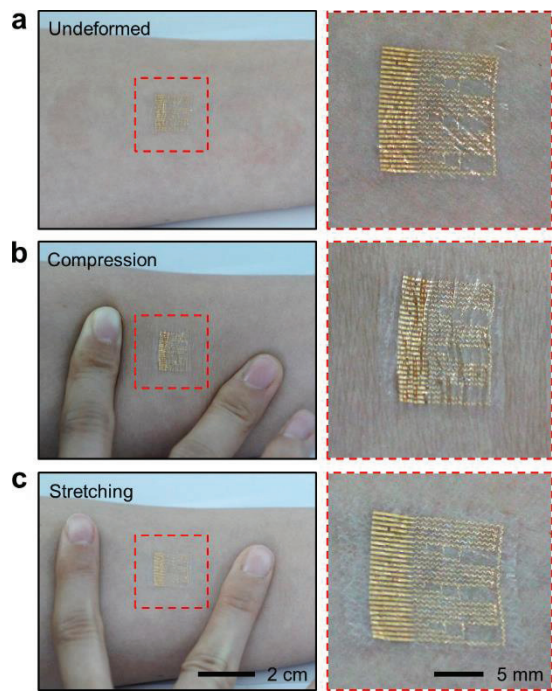


Figure 4.3. Deformable mSCs electronic patch. (a-c) The mSCs electronic patch laminated on skin: undeformed (a), compressed (b), and stretched (c) states. Photographs (right column) show magnified view of each state in the red dotted box.

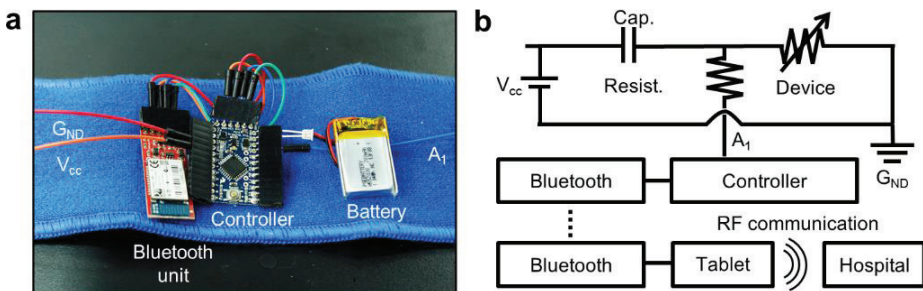


Figure 4.4. Smart band that consists of a Bluetooth unit, a battery, and a controller unit. (a) Image of a custom-made smart band that consists of a Bluetooth unit, a battery, and a controller unit. **(b)** Schematic diagram of the smart band circuit for the real time sensing, wireless data transfer to external devices, and remote control of the electronics in the patch using commercial devices such as a smartphone.

4.2 Experimental Section

4.2.1. Model for Negative Pressure in Compressed mSCs

As discussed in the main text, a 2D array of miniaturized suction cups (mSCs) of half space can be simplified as a single spheroidal void in an infinite body. When arbitrary remote loading ϵ^0 is applied (**Figure 4.10d**, middle), assuming void pressure remains unchanged, the volume change of the void is going to be,

$$V_1 - V_0 = \epsilon_{kk} V_0 = [\epsilon^0 - S(S - I)^{-1}\epsilon^0]_{kk} V_0 \quad (1)$$

where I is the 4th-order identical tensor and S is the 4th-order Eshelby tensor^[25] which are determined by the geometry of the void and the Poisson's ratio of the matrix material. After remote loading is removed, the final pressure and volume becomes p_2 and V_2 as the void volume can be partially recovered (Figure 4.10d, right). Using the superposition illustrated in **Figure 4.5a**, the strain field in the void can be obtained and expressed as follows:

$$\begin{aligned} \epsilon_{ij} &= \epsilon_{ij}^1 + \epsilon_{ij}^2 \\ &= \frac{p_0 - p_2}{2\mu + 3\lambda} \delta_{ij} - [I - S(S - I)^{-1}]_{ijkl} \frac{p_0 - p_2}{2\mu + 3\lambda} \delta_{kl} \\ &= [S(S - I)^{-1}]_{ijkk} \frac{p_0 - p_2}{2\mu + 3\lambda} \end{aligned} \quad (2)$$

where μ and λ are Lamé constants of the matrix material. Thus the volume

change after the remote loading removed is written as

$$V_2 - V_0 = [S(S - I)^{-1}]_{iikk} \frac{p_0 - p_2}{2\mu + 3\lambda} V_0 \quad (3)$$

When uniaxial compressive strain, $\epsilon_{11} = \epsilon_{22} = -\nu\epsilon_{33} = \nu\epsilon$ ($\epsilon > 0$), is applied remotely to the infinite body with a spheroidal void which has three semi axes $(a_1, a_2, a_3) = (a, a, \alpha a)$, the negative pressure in the void can be found by combining equation (1), (3) and $p_0 V_1 = p_2 V_2$ and is written as

$$\frac{\Delta p}{p_0} = \frac{p_0 - p_2}{p_0} \approx \frac{C_1}{1 + 3\beta C_2/4} \epsilon \quad (4)$$

where

$$C_1 = \frac{(1-\nu)[4-5g+4\nu(1-2g)+2(1-2g)(1-2\nu)\alpha^2]}{2[g+2\alpha^2-4\alpha^2g-(1-\alpha^2)(1+\nu)g^2]} \quad (5)$$

$$C_2 = \frac{6(1-2\nu)(1-\alpha^2)g^2-4\nu(1-3g)(1-\alpha^2)+4+2\alpha^2-9g}{3[g+2\alpha^2-4g\alpha^2-(1-\alpha^2)(1+\nu)g^2]} \quad (6)$$

and

$$g = \begin{cases} \frac{\alpha}{(1-\alpha^2)^{3/2}} (\cos(\alpha) - \alpha\sqrt{1-\alpha^2}) & \text{for } \alpha < 1 \\ \frac{\alpha}{(\alpha^2-1)^{3/2}} (\alpha\sqrt{\alpha^2-1} - \operatorname{acosh}(\alpha)) & \text{for } \alpha > 1 \end{cases} \quad (7)$$

The FEM simulations (Figure 4.5 b and c) are also performed to validate the theoretical results given by equation (1) and (3). The infinite body is modeled as an axisymmetric bulk material (element type: CAX4R, Young's modulus: 108 kPa, Poisson's ratio: 0.499) under uniaxial compressive strain $\epsilon = 1\%$ in the axial direction. Spheroidal voids with six different values of α (0.4, 0.5, 0.6, 0.7, 1, and 2) are modeled in FEM and comparisons between the numerical

and the theoretical values are graphed in Figure 4.5 d and e. As we can see from Figure 4.5d and e, the theoretical values matched the FEM results which have validated our derivation.

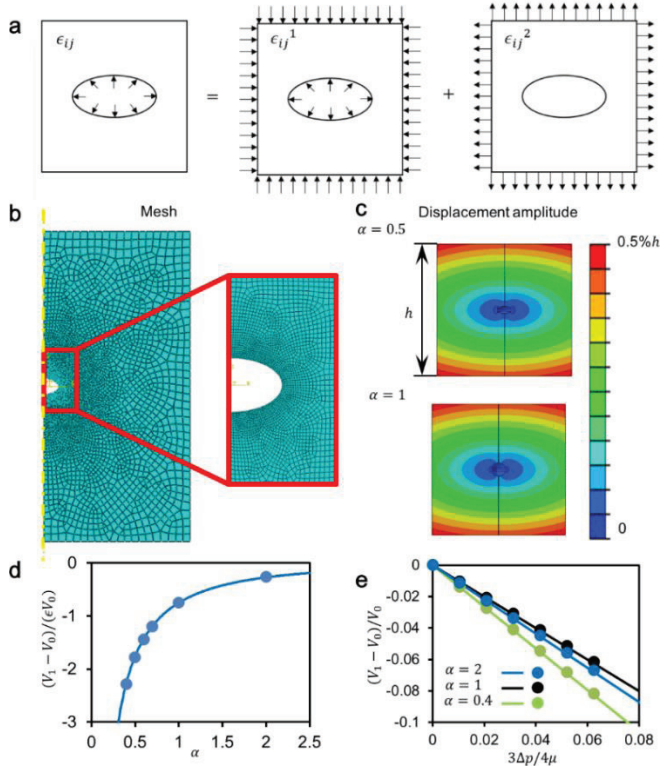


Figure 4.5. Modeling of mSC structures. (a) A void embedded in a body with pressure exerted on the void surface can be considered as the superposition of the following 2 configurations: both the void and the body surfaces are loaded by the same pressure; only the body surface is loaded by the pressure but in the opposite way. (b) The mesh of the FEM model to check how the spheroid void embedded in an axisymmetric body changes. (c) The contour plot of displacement amplitude for $\alpha = 0.5$ and 1 respectively. (d, e) The comparison between the FEM results and the theoretical results where the dots are all FEM results and the curves are obtained from equation (1) in (d) and equation (3) in (e). The applied compressive strain, ϵ , is 1%.

4.2.2. Animal Behavior Test (Monitoring Number of Scratches)

In order to quantify the degree of discomfort after wearing patches, we performed the animal behavior test by using the mouse model. For the similarity with the human skin, nude mice (Balb/c nude mice) were used. We assumed a high degree of discomfort due to the wear of patches would lead to more scratching behavior.^[26,27] Thus the count of scraping action in three different experimental sets (mouse of bare back, back with the mSC patch, back with the commercial hydrocolloid patch) can be a good factor for the quantification of the discomfort induced by different patches.

To visually observe animal behavior, we laminated patches on the back of mice and allowed the mice to swim in water for ~3 minutes. The purpose of the swimming is to remove residual PVA (water-soluble temporary supporting layer) and to confirm conformal mechanical coupling between the patch and the mouse skin. Each mouse was kept in its own cage to isolate each other. Scratching during experiments was monitored for ~3 hours across six mice. To minimize the influence of different time slots and individual differences between animals, behavior tests were carried out during the same time zone and the mice were experimented in turns. The interval of animal behavior tests spanned across ~1 week to ensure that the mice were stable. Scratching behavior in anatomical regions adjacent to the patch were included,

while grooming actions were excluded.

The effect of patch stiffness on comfort was also estimated via similar animal behavior tests. Ultra-soft patches of different thicknesses ($\sim 30 \mu\text{m}$, $\sim 150 \mu\text{m}$, and $\sim 500 \mu\text{m}$) were employed using the same experimental set-up and conditions with the aforementioned animal behavior test. The thinnest patches ($\sim 30 \mu\text{m}$) exhibited the lowest scratching number, which implies highest comfort levels, whereas the thick one resulted in the opposite (**Figure 4.6 c** and **d**). These trends were analyzed by comparing the number of scratches with the stiffness of each patch. Stiffer (thicker) patches tended to cause more strain on the skin and thereby more scratches/discomfort. FEM simulations (uniaxial strain for Figure 4.6 e-h and biaxial strain for Figure 4.6 i-l) corroborated with the experimental results, i.e. the ultrasoft mSC patch caused negligible irritation.

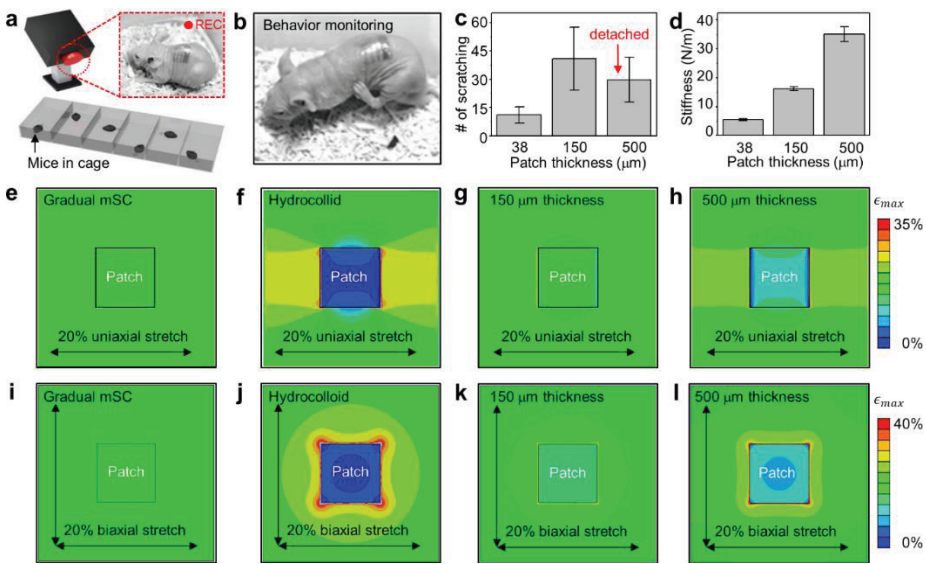


Figure 4.6. Animal scratching behavior test for the measuring of comfortness **(a)** Schematic illustration of the animal behavior observation. Scratching numbers are counted to quantify the degree of discomfort. **(b)** Photograph of mouse's scratching. **(c)** The number of scratching with different patch thicknesses. The scratching number of $\sim 500 \mu\text{m}$ thick patch decreases below that of $\sim 150 \mu\text{m}$ thick patch, because the patch was delaminated from the back of mice before the experiment is over. **(d)** Stiffness versus patch thickness. **(e-h)** Finite element modeling of the load on the patch-attached skin when $\sim 20\%$ uniaxial stretch is applied ($\sim 38 \mu\text{m}$ gradual mSC patch **(e)**, hydrocolloid patch **(f)**, mSC patch with thickness $\sim 150 \mu\text{m}$ **(g)** and $\sim 500 \mu\text{m}$ **(h)**, respectively). **(i-l)** FEM simulation of the induced strain on the patch-attached skin when $\sim 20\%$ biaxial strain is applied; result of $\sim 38 \mu\text{m}$ gradual mSC patch in **(i)**, hydrocolloid patch in **(j)**, $\sim 150 \mu\text{m}$ mSC patch in **(k)**, and $\sim 500 \mu\text{m}$ mSC patch in **(l)**, respectively.

4.2.3 Fabrication of mSC Molds

First, Si molds with the dot-shape trench array of ~500 nm radius and ~3 μm height are prepared by the deep reactive ion etching (Versaline, PLASMA THERM, USA) using the inductively coupled plasma. The surface of Si molds is treated with trichloro(1H,1H,2H,2H-perfluorooctyl)silane (FOTCS) self-assembled monolayer (SAM). Then the hard polyurethane acrylate (h-PUA; MINS 311 RM, Minuta Tech., Korea) is coated and photo-cured on it. Quick detachment of the h-PUA film after its uniform filling into deep trenches of the Si mold achieves the array of mountaintop-shaped h-PUA structures on the Si mold. The weak oxygen plasma etching of the h-PUA structures on the Si mold provides a circular groove near the border of Si trench, since Si is not etched while h-PUA is etched. This groove serves as a rim of mSCs. After FOTCS SAM treatment of the prepared h-PUA/Si mold, another layer of h-PUA is coated, cured, and detached. Then, the mSC mold made of h-PUA is obtained.

4.2.4 Device Fabrication

The device fabrication begins with spin coating the precursor (~1 μm thick film) of polyimide (polyamic acid, Sigma Aldrich, USA) or benzocyclobutene (cyclotene 3022, Dow Chemical, USA) on a sacrificial layer

(poly(methylmethacrylate) (PMMA A2, MicroChem, USA) or thermally deposited nickel layer). 100 nm thick Boron doped Si nano-membranes are prepared from the silicon-on-insulator wafer (SOITEC, France) and then transferred onto prepared polymer films. Desired geometries of electronics are achieved by photolithography and dry etching processes. A lift-off process of Ti/Pt (5/40 nm) film is used for temperature sensors. Cr/Au (7/70 nm) layers are deposited thermally and patterned by the photolithography process for serpentine-shaped interconnections. Additional spin coating forms the top polymeric passivation layer. Final patterning and dry etching steps complete the fabrication of stretchable electronic devices.

4.2.5 Fabrication of Gecko-Inspired Miniaturized-Pillar Structure

Miniaturized-pillar (m-pillar) structures, inspired by gecko setae, were fabricated through a combination of photo-/soft-lithography techniques. Photolithography and inductively-coupled-plasma-assisted deep-reactive-ion-etching patterned an array of holes (reverse structure of m-pillar) on Si wafer. Each hole pattern in this Si master has the size of 1 μm diameter and 3 μm depth. The negative replica mold of m-pillars was fabricated with the photo-curable poly(urethane acrylate) (PUA; MINS 301 RM, Minuta Tech., Korea). To reduce the interfacial energy, FOTCS surface modification was performed.

Stretchable electronic devices were transferred onto the fully cured bottom PDMS layer (sylgard 184, Dow Corning, USA) (1.6 MPa) on poly(vinylalchol) (PVA; Kuraray, Japan) film. Another top PDMS layer (1.6 MPa) was spin-coated and partially cured at 70 °C oven. The negative pillar mold was laminated on the partly cured PDMS, pressed, and then completely cured in 70 °C oven. The final m-pillars were formed by removing the mold.

4.2.6 Fabrication of mSC Electronic Patch

The electronics were released from the temporary handling substrates by etching a sacrificial layer, and then transferred onto an elastomer film of ~39 kPa modulus (Ecoflex 0030, Smooth-on Inc., USA) coated on a PVA film (water-dissolvable temporary supporting layer). After super-hydrophobic treatment of the mSC mold, three PDMS prepolymer solutions diluted by toluene (concentrations: 0.5 g/mL, 1 g/mL, and 2 g/mL) were mixed with the PDMS curing agent of 0.1 g/mL concentration, respectively. The resulting PDMS mixture solutions were then spin-coated in the mSC mold in a sequential order, following spin coating of ~39 kPa PDMS. The coated film was partially cured in 70°C oven and assembled with O₂-plasma-treated devices on Ecoflex/PVA film. The assembled sample was strongly pressed with ~5 mm thick PDMS dampers to equally distribute the applied pressure. Full curing (in

70°C oven), followed by detaching the mSC mold completed the fabrication steps. Additional electrodes for electrophysiology monitoring and iontophoresis were transfer-printed onboard the mSC structure with water soluble tapes (3M Corp., USA).

4.2.7 Adhesion Tests and Verification of Conformal Contacts

The patch adhesive was characterized on a human skin mold (PUA duplication with human skin morphology). Patch samples with different surface structures (gradual mSC, m-pillar, 1.2 MPa mSC, 60 kPa flat) were utilized and back-supported by ~50 µm thick PET films coated with 10:1 PDMS. Each sample was cut into ~1.2 cm width and the adhesion force (maximum force during dragging) was measured by a digital force gauge (Mark-10, USA). Conformal contact was verified by using the mSCs/m-pillar patches containing fluorescent dyes (rubrene, Sigma Aldrich, USA). The patches were laminated on artificial Ecoflex skin segments, and the three-dimensional interface between the patch and the skin was observed via confocal microscopy (LSM780 NLO, Carl Zeiss, Germany).

4.2.8 Characterization of Mechanical Properties (System Modulus)

After dissolving the PVA film (water-dissolvable temporary

supporting layer), the patch was rolled up. Both ends of the rolled patch were fixed by the digital force meter, which measured the induced load during stretching. The system modulus was calculated from the slope of stress-strain curves. To characterize the modulus of the entire system stack, similar experiments were performed across various elastomers (*e.g.*, PDMS, Ecoflex).

4.2.9 Procedures for Reuse of mSC Patch

The mSC patch laminated on the skin was detached by the water-soluble tape which acted as a temporary substrate. After cleansing the patch with acetone (the ingredient of the nail manicure remover) and reloading drugs by drop-casting the drug solution, the patch was re-attached onto the skin. Then the water-soluble tape was easily removed from the skin with the water. Following drying step finished the patch regeneration.

4.2.10 Monitoring Human Vital Signs *in-vivo* and Acute Disease Model

The connector consisted of an array of metal lines was interconnected to a data-acquisition system (National Instruments, USA) through an anisotropic conductive film. Devices were attached on a few locations on skin, including the radial artery, joint, and chest. After the PVA film was dissolved, the patch made conformal contacts to monitor highly sensitive physiological

signals. For animal disease models, strain gauges attached on the epidermis over the heart of the mouse measured the heart rate and respiratory rate. The ethanol tap on the mouse body was utilized to induce acute hypothermia.^[28] 100 µg Norepinephrine (Sigma Aldrich, USA) and 100 µg propranolol (Sigma Aldrich, USA) diluted with phosphate buffered solution were intravascular injected to cause and alleviate acute hypertensive emergency.^[29] Injection of desire-sized thrombus which was formed from mouse blood into inferior vena cava led to blocking pulmonary capillary (pulmonary thromboembolism).^[30]

4.2.11 Wireless Communication System

The custom-made wireless communication system equipped on the smart band was built. It consists of a controller, Bluetooth unit (Arduino Pro Mini, Sparkfun, USA), and battery (Figure 4.4a). The medical devices on mSC patches were connected to the external commercial devices (e.g. tablets or smartphones) wirelessly through Bluetooth module of the smart band. Data was transferred to external devices from mSC patches and commands were delivered vice versa. For instance, the resistance change of strain gauges was measured through the specially designed resistor-capacitor (RC) circuit (Figure 4.4b). The resistance alternation modulated the discharging time of capacitor, which was detected by the controller unit and wirelessly transferred to external

devices through Bluetooth unit. A Labview (National Instruments, USA) program analyzed the RC delay and changed over to original resistance values. The program also monitored the motion of high-risk patients, such as tremors, and sent alarms in emergency situations. Another program installed in controller unit can remotely turn on/off the iontophoresis actuator by using smartphone applications (SPLDuino Lite, Helloapps, USA).

4.2.12 Synthesis of RITC-doped Mesoporous Silica Nanoparticles with Enlarged Nanopores

44 µL of 3-aminopropyltriethoxysilane (APTES; Aldrich, USA), 10 mg of rhodamine B isothiocyanate (RITC; Aldrich, USA), and 1 mL of anhydrous ethanol (Aldrich, USA) were mixed and stirred overnight under the dark condition. Amine group in APTES and isothiocyanate group in RITC were covalently conjugated. The solution was stored in the refrigerator and used without further purifications. To synthesize RITC-doped mesoporous silica nanoparticles with enlarged nanopores (RITC-MSN-L), previous method^[31] was adopted and modified. In details, 3 g of hexadecyl trimethyl ammonium chloride solution (CTAC, 25 wt% in water; Aldrich, USA), 90 mg of triethanolamine (Samchun, Korea), and 30 mL of deionized water were mixed. The solution was heated to 95°C with vigorous stirring. After 1 hour, 2.5 mL of

trimethylbenzene (TMB; Aldrich, USA) was added and 2.25 mL of tetraethylorthosilicate (TEOS; Acros, USA) and 225 μ L of RITC-APTES solution were injected simultaneously. The resulting solution was aged for another 1 hour. The products were centrifuged and washed for several times with deionized water and ethanol to remove unreacted precursors, and dispersed in ethanol. To remove the template (hexadecyl trimethyl ammonium cation in mesopores), 500 μ L of HCl (35%; Samchun, Korea) was added and stirred at 60°C for 1 hour. Then, products were centrifuged and washed by anhydrous ethanol for several times and redispersed in anhydrous ethanol (25 mL). To functionalize RITC-MSN-L with amine groups, 100 μ L of APTES was added to ethanol solution containing RITC-MSN-L. To accelerate the reaction, the mixture was refluxed for 3 hours. After the centrifugation and washing with anhydrous ethanol, amine-functionalized RITC-MSN-L was redispersed in 10 mL of anhydrous ethanol. PEG was covalently conjugated onto RITC-MSN-L-NH₂. 100 mg of mPEG-SG 5000 (Succinimidyl glutarate terminated; Sunbio, Korea) was added to RITC-MSN-L-NH₂ solution and stirred overnight at 35°C. After reaction was completed, products were centrifuged and washed with ethanol and redispersed in 10 mL of chloroform.

4.2.13 Immunofluorescence and Western Blot Analysis

The skin tissues were embedded in optimal cutting temperature (OCT) compound and were sliced at coronal plane to 10 µm thick by microtome (Leica, Germany). This sliced tissues were mounted on slides, and stained with Hematoxylin-Eosin (MHS16, HT110180, Sigma aldrich, USA) by standard histochemical procedure. For the **Figure 4.7c**, the H&E staining of mouse skin was immediately performed after detaching the laminated patches.

Moreover, to prepare immunofluorescence imaging of inflammation factors, we utilized IL-1 β (SC-7884, Santa Cruz Biotechnology, USA) and iNOS (2982S, Cell Signaling Technology, USA) by standard protocol. For the western blot, lysates of skin tissue were prepared with Lysis buffer, which were made of 150 mM NaCl, 50 mM Tris-HCl (pH 7.4), 1% NP-40, 0.1% Sodium Dodecyl Sulfate (SDS), 1 mM Sodium orthovanadate (Na_3VO_4), 5 mM Sodium Fluoride (NaF), 0.25% Sodium Deoxycholate, 5 mM N-Ethylmethylamine, and protease inhibitor cocktail (Roche, Switzerland). The protein concentration was determined with BCA Protein Assay kit (Thermo Fisher Scientific, USA). Tissue lysate samples were separated on 4-12% Bis-Tris Plus gel (Thermo Fisher Scientific, USA) with MES buffer (50 mM MES, 50 mM Tris Base, 0.1% SDS, 1 mM EDTA, pH 7.3) and transferred to Polyvinylidene difluoride (PVDF) membrane with 0.2 micrometer pores (Bio-rad., USA). The blots were

incubated with primary antibodies: mouse anti-TNF α (1:500, Abcam, USA), mouse anti-IL-1 β (1:500, Cell Signaling Technology, USA), and mouse-anti β -actin (1:20000, Sigma, USA). After that, all blots were incubated with secondary antibody: goat anti-mouse IgG-HRP (Santa Cruz Biotechnology, USA). The blot images were captured using the Fusion FX7 system (Vilber Lourmat, Germany) and band density was analyzed by Bio-1D program (Vilber Lourmat, Germany).

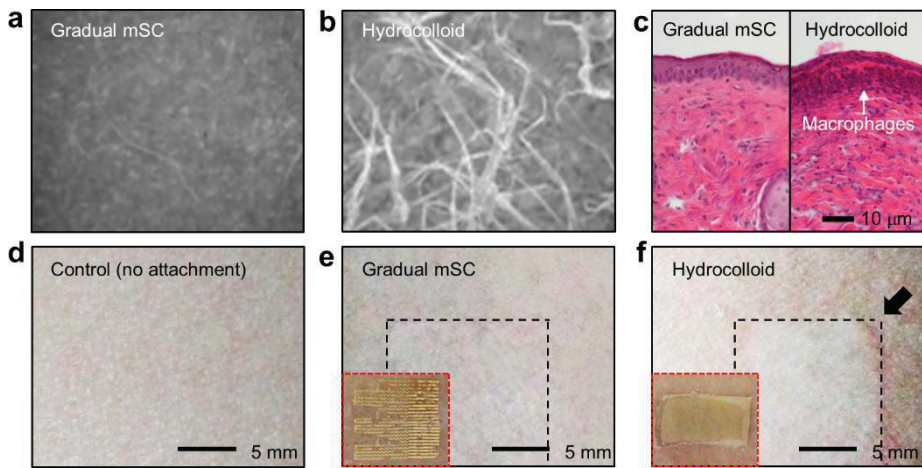


Figure 4.7. Peel-off test of mSC patch. (a, b) Microscope images show the surface of patches (gradual mSC patch in (a) and hydrocolloid patch in (b)) after peeling-off. (c) Cross section image of the skin in the H&E stain histology. (left: gradual mSC patch, right: hydrocolloid patch). (d-f) The skin conditions after detaching each patch from human arms: control (no attachment) (d), gradual mSC patch (e), and hydrocolloid patch (f). Each patch is laminated on skin for 4 days. The reddish irritation is observed on the hydrocolloid-laminated skin (black arrow in (f)). The insets of (e) and (f) present the condition of the laminated patches on the skin after attaching for 4 days.

4.2.14 Laboratory Animals

Balb/c nude mice (age: 6 weeks) were obtained from the Experimental Animal Center, Chuncheon Center, Korea Basic Science Institute (KBSI), Chuncheon, South Korea. These animals were individually housed in transparent plastic cages with wire grid covers under controlled temperatures (22-24°C) with the 12 hour light/dark cycle (lights on from 08:00 to 20:00). All animal procedures were in accordance with the Guide for the Care and Use of Laboratory Animals issued by the Laboratory Animal Resources Commission of KBSI. The Institutional Animal Care and Use Committee at the KBSI (KBSI-AEC1409) reviewed and approved this study. All of the experiments were conducted to minimize the number of animals used and the suffering caused by the procedures used in the current study.

4.3 Result and Discussion

4.3.1 Fabrication, Characterization, and Analysis of Bio-Inspired Suction

Cup Arrays

The fabrication process for the low modulus electronic patch in combination with the aforementioned mSC structures is described. First, the stretchable electronics (Figure 4.2) are transferred onto ultrathin rubber (~14 μm , ~39 kPa) coated on the PVA film. The h-PUA mold with intaglio mSC patterns with super-hydrophobic coating is separately prepared (**Figure 4.8**). The mold is sequentially spin-casted with diluted PDMS layers, whose modulus is gradually altered from ~1.6 MPa to ~500 kPa (**Figure 4.9 a and b**). The relatively high modulus (~1.6 MPa) layer helps to form mSC structures, while the low modulus (~500 kPa) layer provides a soft interfacial layer.^[32] The thickness of coated PDMS layers (~4 μm) is much thinner than the rest of the system (~45 μm), thereby allowing the electronic patch with mSC arrays to achieve the ultra-low system modulus (~108 kPa), which is smaller than the modulus of epidermis (~150 kPa), as shown in Figure 4.9. These fabrication steps are completed upon full cure and removal from the mold. Dissolution of the temporary PVA film finally allows lamination of the electronic patch on skin (Figure 4.3).

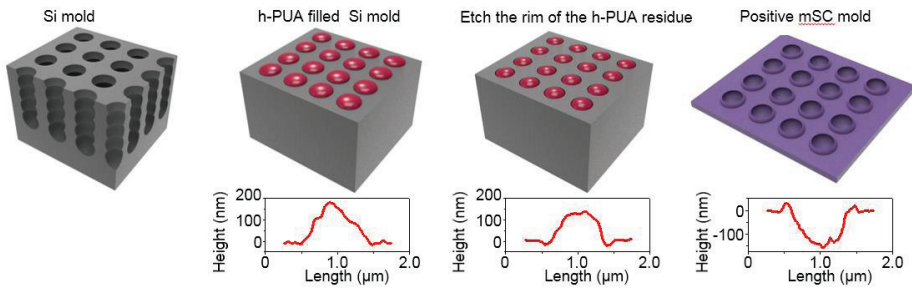


Figure 4.8. Schematic diagram for the fabrication of mSCs mold. The UV curable h-PUA is poured in the sinuous hole-patterned Si mold, partially cured, and detached leaving residual embossed h-PUA on the Si mold. The rim of the embossed h-PUA is etched with oxygen plasma. Repetitive molding makes positive mSCs mold. The insets show the 3D AFM images and corresponding two dimensional AFM profile of the vertical cross-section, respectively.

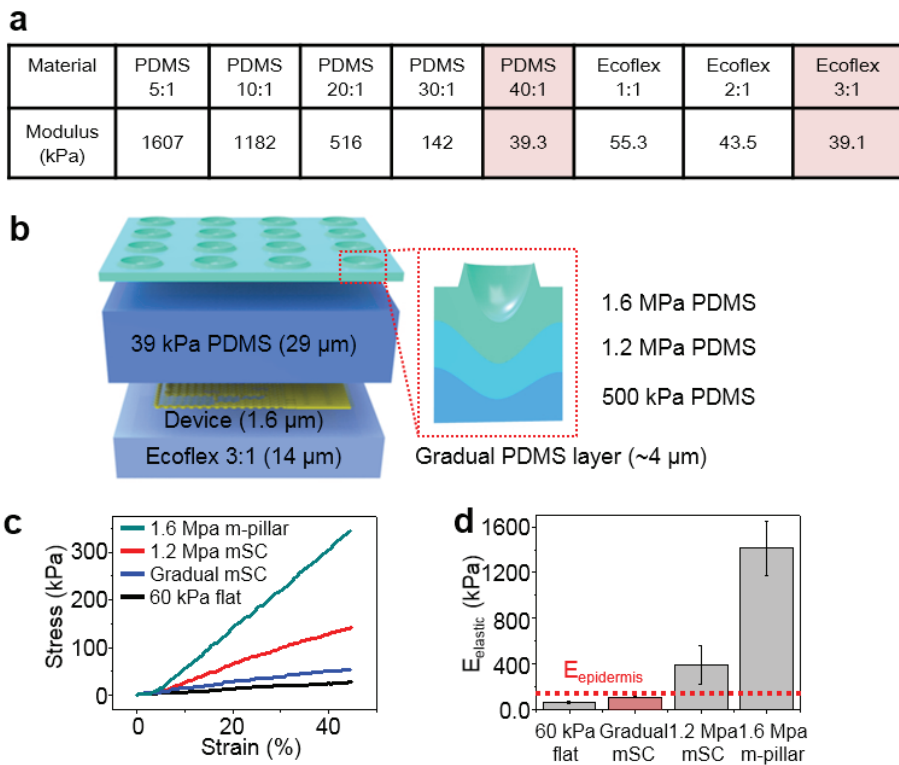


Figure 4.9. Mechanical characteristics of gradual mSC structures. (a) Table that summarizes the Young's modulus of various elastomers (PDMS and Ecoflex). (b) Schematic illustration of the exploded view of the mSC electronic patch. The dashed red box shows a magnified illustration of the mSC structure. The mSC structure consists of three elastomeric layers with gradually changing modulus. The thickness of the gradual PDMS layer is less than ~4 μm . (c) Stress-strain curves for different layers of elastomeric patch. (d) Comparison of the system modulus of various elastomeric patch layers. Red dotted line shows the modulus of human epidermis.

Figure 4.10a shows SEM images of the cephalopod-inspired mSC (top) and the gecko-inspired miniaturized pillar (m-pillar; bottom) structures. Inset shows the top view of mSC structures. These two bio-inspired structures are used to evaluate the tackiness of dry adhesives. Although m-pillars enhance adhesion strength by increasing surface area, these structures require relatively high modulus materials to maintain their shape without tilting, bending, or collapsing.^[32] The system modulus of m-pillar structures (~1.4 MPa; Figure 4.9 c and d) is thus higher than that of the epidermis. In contrast, the mSCs with low aspect ratio (~150 nm height and ~950 nm diameter) can be readily fabricated with ultra-low system modulus (~108 kPa) and exhibit greater tackiness (Figure 4.10b) by a factor of ~3 relative to m-pillars. Confocal microscope images provide more information about enhanced adhesion forces and conformal contacts of mSCs over m-pillars on highly variable skin morphologies (Figure 4.10c).

The mechanics underlying enhanced adhesion of mSCs are analyzed theoretically by finite element modeling (FEM) (Supporting information). Assuming that the mSCs are compressed against a frictionless surface, due to symmetry, a 2D array of mSCs on the surface of half space is equivalent to a 2D array of spheroids in an infinite body, where the Eshelby's inhomogeneity solution applies.^[33] As the stress field in Eshelby's problem decays with

distance cubed, i.e. proportional to $1/r^3$, an mSC structure with radius of 500 nm, spacing of 4 μm , and patch thickness of 47 μm justifies negligible neighboring effects and the half space assumption. Therefore the 2D array of spheroids can be simplified into a single spheroid model with an eighth of it depicted in Figure 4.10d, with the semi-axes of the spheroid being $(a_1, a_2, a_3) = (a, a, \alpha a)$. The initial pressure and volume of the mSC are given by p_0 and V_0 , where p_0 denotes atmospheric pressure. Applying a compressive strain of ϵ on top of the patch will squeeze some air out of the mSCs, giving rise to new volume V_1 while pressure remains the same, i.e. $p_1 = p_0$. When ϵ is removed, assuming no air can come back to the mSC, the mSC volume will partially recover and the final pressure and volume becomes p_2 and V_2 . Since $V_2 > V_1$, we expect $p_2 < p_0$, assuming the amount of gas in the mSC remains the same. Therefore, removal of ϵ effectively creates a negative pressure of $\Delta p = p_0 - p_2$ inside the mSC, and a resulting suction force.

To analytically solve non-dimensionalized $\Delta p/(p_0\epsilon)$ as a function of α , β , and ν , where $\alpha = a_3/a_1$, $\beta = p_0/\mu$, and μ and ν represent the shear modulus and Poisson's ratio of the matrix, respectively, we implement the following strategy (see *SI Appendix* for details). First, we use Eshelby's inhomogeneity solution to analytically derive $V_1(V_0, \epsilon)$. Applying negative pressure Δp to a relaxed mSC allows calculation of the final volume $V_2(V_0, \Delta p)$. The ideal gas

equation $p_0V_1(V_0, \epsilon) = p_2V_2(V_0, p_0 - p_2)$ becomes an equation with just one unknown variable, p_2 , which is analytically solvable. Since Eshelby's solution is only valid for small deformation, we have implemented the following constraints on our solution: $0 \leq \epsilon \leq 5\%$ and $0 \leq (V_0 - V_1)/V_0 \leq 10\%$. Practically, it is also required that $0 \leq p_2 \leq p_0$. The analytical solution under these constraints is plotted in Figure 4.10e, with $\beta = 2.8$ ($p_0 = 101$ kPa, $\mu = 36$ kPa) and $\nu = 0.499$ fixed. As shown in Figure 4.10e, the maximum allowable $\Delta p/p_0$ first increases and then decreases with α , suggesting an optimum α can be found with the given constraints. Experimentally, α^* is computed to be 0.32 with $a_1 = 500$ nm and $a_3 = 160$ nm, which is highlighted in Figure 4.10e. In addition to mSC shape, material properties including μ and ν can also affect $\max(\Delta p/p_0)$.

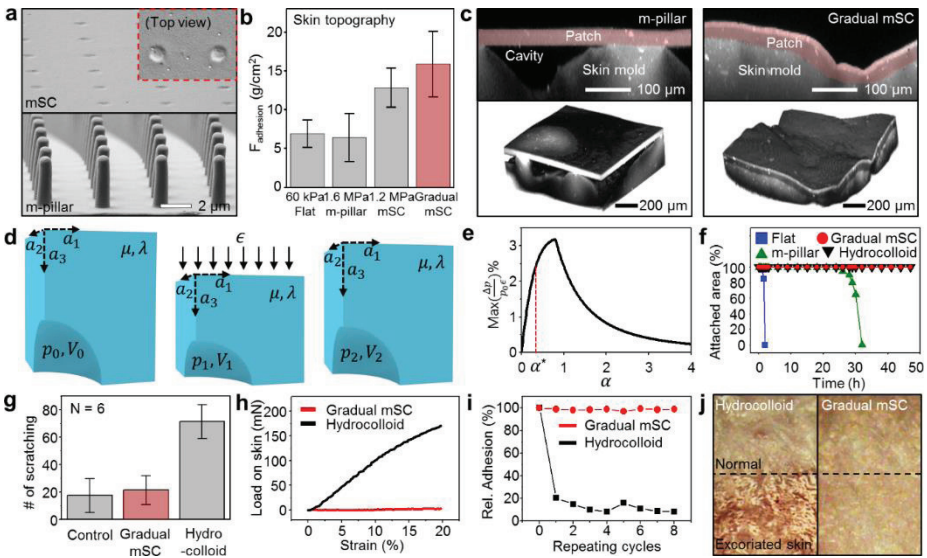


Figure 4.10. Bio-inspired suction cups as comfortable dry adhesives. **(a)** SEM images of the side view of mSCs (top; inset shows top-view of mSCs) and m-pillars (bottom). **(b)** Change in adhesion force on the skin topology mold with different surface-structured patches (flat, m-pillars, mSCs with different moduli). **(c)** Confocal microscope images (cross-section and 3D view) at the vicinity of the contacting interface between structured patch and skin mold (left: m-pillar, right: gradual mSC). **(d)** Spheroidal void embedded in the infinite body with Lame constants (μ, λ) and semi-axes $(a_1, a_2, a_3) = (a, a, \alpha a)$. The initial pressure and volume of the void (p_0, V_0) are changed to (p_1, V_1) when compressive strain ε is applied. After removing the load, the void would partially recover its shape to (p_2, V_2) . **(e)** The max $(\Delta p/p_0 \varepsilon)$ versus α . The α^* is computed to be 0.32 with dimension of mSCs ($a_1 = 500 \text{ nm}$ and $a_3 = 160 \text{ nm}$). **(f)** Durability tests of mSC patches on the back of mice in comparisons to flat, m-pillar, and commercial hydrocolloid patch. **(g)** Scratching behavior test compared with hydrocolloid patch. **(h)** Load on patch-attached skin when extra strain is applied. **(i)** Change in the adhesion strength during recycling of mSC and hydrocolloid patch on the skin. **(j)** Skin morphologies after 3-times of delaminating hydrocolloid patch (left) and mSC patch (right).

4.3.2. Bio-Compatibility, Discomfort and Tissue Inflammation

Wearable patches often cause time dependent irritation and discomfort.^[34] To quantify the effects of wear on the skin, we designed animal model studies to assess behaviors in response to patch wear. We monitored mice fitted with these wearable patches and used a video camera to monitor their behaviors in cages (Figure 4.6 a and b). A detailed description of the experiment to observe animal behavior is included in Supporting Information. Briefly, electronic patches are laminated on the back skin of each mouse. We recorded the number of scratches over 3 hours to assess the degree of irritation. To evaluate long-term wearability, we compared the durability of mSCs patches relative to m-pillar/flat patches and commercial hydrocolloid patches by affixing patches to the lower back surface of mice. The mSCs and hydrocolloid patches firmly adhered on mice skin for over 2 days, whereas the m-pillar and flat patches delaminated in 2 and 30 hours, respectively, due to weaker adhesion and mechanical interaction with skin (Figure 4.10f).

Therefore we excluded m-pillar and flat patches then compared the degree of the comfort of the mSC patches with commercial hydrocolloid patches that show good adhesion by relying on chemical adhesives. The number of scratches recorded with mSC patches is similar to the control (mice with bare back), while the number of scratches counted with commercial hydrocolloid

patches is 4 times higher (Figure 4.10g). The difference in shear forces applied to the skin (Figure 4.10h) explains scratching tendencies. The higher stiffness of the commercial hydrocolloid patches induces the higher loads/strains on the skin, which in turn give rise to high skin discomfort, while vice versa in the mSC patches. This behavior analysis agrees with FEM simulations (Figure 4.6 e and f). See Supporting Information, Figure 4.6 c-1 for more details about the relation between the patch stiffness and scratch count.

Another important aspect of electronic patches is the reusability.^[35] The mSC patch maintains its adhesion strength for ~8 cycles of reuse, whereas the hydrocolloid patch loses its adhesion force significantly after the first use, causing detachment from the skin (Figure 4.10i) and thereby difficulty to reuse electronics. Figure 4.10j shows skin conditions following three attachment/detachment cycles over the course of 1 day (dry adhesives in mSC patch and chemical adhesives in hydrocolloid patch). The top half of the frame shows bare skin without patch while the bottom half shows a skin segment under the patch. Black dotted lines show the border between two segments. The skin laminated with a hydrocolloid patch (left) undergoes some amount of abrasion and scarring that is visually observed, while skin in contact with the mSC patch (right) remains intact. Fluffs are also peeled off by the hydrocolloid patch in the regions of skin with rashes and scarring (compare images of Figure

4.7 a and b). Moreover, skin segments underneath the hydrocolloid patches exhibited an inflammatory response. This is evident in the Hematoxylin and eosin (H&E) histological stains, which show the presence of macrophages and other inflammatory cells near the dermis for the hydrocolloid patch (Figure 4.7c). The mSC did not exhibit any inflammatory responses and biocompatibility was confirmed in the human wearability experiment, in which the mSC patch was laminated on human arms for 4 days (Figure 4.7 d-f).

4.3.3 Vital Sign Monitoring, Detection of Acute Medical Conditions, and Wireless Communications

Conformal integration of ultrathin electronic sensors onboard mSC patches establishes a skin-interfaced platform for vital sign monitoring of small arterial pulse waveforms non-invasively and electrocardiographic signals with high sensitivity. For example, strain gauges integrated on mSC patch have high sensitivity to precisely detect an arterial pulse wave from the radial artery of a healthy subject without the external pressure (**Figure 4.11a top**). In contrast, strain gauges on the m-pillar and hydrocolloid patches cannot detect slight changes of small arterial pulse without external pressure (Figure 4.11a middle and bottom).^[32,36] Arterial pulse signals measured by the mSC electronic patch are sufficiently accurate to obtain clinically important information on

cardiovascular aging, i.e. to distinguish the dicrotic notch (a tiny dig between systolic and diastolic phase in the arterial pressure waveform) and the slope of the pulse (Figure 4.11b). With aging or the increase of arterial stiffness, the dicrotic notch in the arterial waveform becomes less pronounced and the slope is steeper.^[37] Figure 4.11b shows a representative example of a mSC electronics-measured arterial waveform with distinct dicrotic notch and less steep slope in a young subject (a 23-year-old male) when compared to that with less prominent notch and steep slope in an old subject (a 50-year-old male). The peak values of arterial pulse waves obtained from mSCs during daily activity of resting, eating, and exercise (Figure 4.11c) are linearly correlated with systolic blood pressure measured by a commercial blood pressure gauge at the identical time, suggesting the potential function as a blood pressure monitor (inset of Figure 4.11c).

Moreover, the real time electrocardiograms (ECG) is simultaneously measured with integrated electrodes, as shown in Figure 4.11d (detailed numbers are indicated at the top). Effective adhesiveness of mSCs to the skin enables to monitor the pulse and ECG consistently without drift or distortion during exercise as well as resting state (Figure 4.11d). Since ultra-conformal lamination of mSC electronics on the epidermis remarkably reduces far-field noises, subtle change of electrical signals originating from the heart can be

detected with high sensitivity, allowing distinct discrimination of a P wave with small amplitude of ~2.5 mV, a QRS complex, and a T wave in ECGs (Figure 4.11e). It helps to differentiate various cardiac arrhythmic diseases, most of which are diagnosed from accurate detection of a P-QRS-T wave.

Continuous monitoring of vital sign changes with mSCs can help detect acute medical conditions,^[38] thereby facilitating medical assists through wireless connections to emergency clinical service providers. In animal experimental models (Balb/c nude mouse) of acute medical conditions including hypothermia, hypertensive emergency, and massive pulmonary thromboembolism, vital signs are monitored *in-vivo* with skin-coupled mSC electronic patches. In the massive pulmonary thromboembolism models, sudden elevation of respiratory and heart rates are alarmed and recovered by immediate intravenous infusion of 50 µg heparin (Figure 4.11 f and g). In the animal experimental models of acute hypothermia induced by ethanol tap on the body, body temperature, heart rate, and respiratory rate are monitored by its simultaneous multi-recording system. The early detection of slow heart rate and depressed respiration with low body temperature following hypothermia facilitates the rapid treatment such as warming (Figure 4.12a). In the norepinephrine-induced hypertensive models, heart rates are abruptly elevated and stabilized with the subsequent administration of 100 µg propranolol (Figure

4.12 b and c).

Figure 4.11 h-j show wireless data transmission and controlled drug release through the Bluetooth unit of the custom-made smart band (Figure 4.4) in conjunction with commercial devices, such as the smartphone. The electronic patch contains essential components such as sensors, actuators, and drug-loaded nanoparticles, while all other expensive wireless, power storage, and controller units are incorporated in the smart band. This strategy allows conformal integration of the electronic patch on skin by decreasing the thickness and stiffness of the patch. Moreover, the cost and size of the patch can be reduced.

Figure 4.11h shows the multifunctional electronic patch connected to the smart band. This system transmits recorded data (vital signs and activities/tremors) wirelessly to external devices in real time (Figure 4.11i). While short-range communications occur through the Bluetooth unit in the custom-made smart band, long-range communications are achieved with a commercial smartphone (Figure 4.1d and Figure 4.4b). Therefore, biosignals including vital signs, physical activity, and tremor can be transmitted wirelessly. In emergency situations, the custom-made Labview software installed in the controller unit determines the states and signals an alarm to remote healthcare units. Moreover, Figure 4.11j shows the concept of telemedicine, the wireless

control of transdermal drug delivery via integrated iontophoresis electrodes. Using an Android application installed in a smartphone, remote medical providers can control the drug delivery rate.

The multifunctional mSC electronic patch allows highly sensitive monitoring of vital signs for long time, detection of acute medical conditions, and wireless communications from/to external devices. These functionalities are useful in preventive medicine and point-of-care clinical applications. System design strategies separating electronic patches from the smart band together with the patch re-use (Figure 4.1f) reduce the financial burden of patients. Even after 8 cycles of reuse, the electronic patch shows stable/reproducible sensing signals (Figure 4.11k).

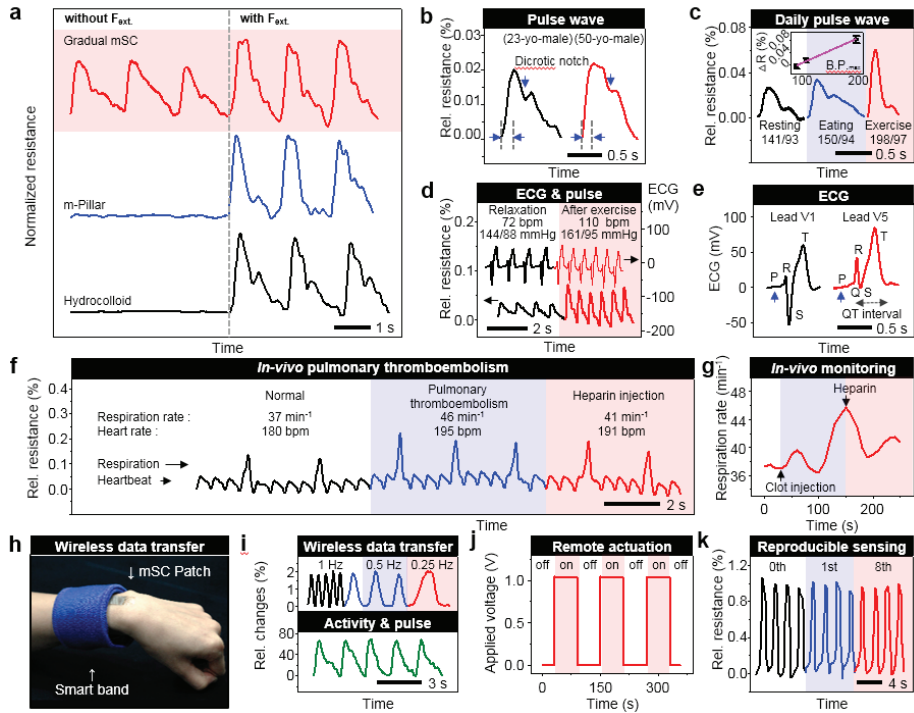


Figure 4.11. Measurement of vital signs, detection of acute medical conditions, and wireless communications. **(a)** Pulse waves measured on the radial artery with/without external pressure. Only mSC patch can record pulse waves without pressurization. **(b)** Comparison of an arterial pulse waveform between the different age groups (23-year-old male and 50-year-old male). **(c)** Changes of arterial pulse waves during daily activity. The peak intensity correlates linearly with the systolic blood pressure (inset). **(d)** Variation in vital signs due to exercises (top: ECG signals from electrodes, bottom: pulse signals from Si strain gauges). **(e)** Surface ECGs recorded on the chest. The electrical waveforms of a P-QRS-T complex are reproduced from the V1 and V5 sites, respectively. **(f, g)** Variation in respiration and heartbeats in a mouse model of

acute pulmonary thromboembolism induced by intravenous injection of massive blood clots and treated with heparin (f). Change in respiration rate at whole time range (g). **(h)** Image of wireless communication settings. The mSCs patch is connected with the smart band which involves the Bluetooth unit and the battery. **(i)** Tremor and pulse data wirelessly received from the Bluetooth system. **(j)** Remotely controlled voltage to turn iontophoresis on/off for the transdermal drug delivery. **(k)** Tested strain gauge functionality after 8 times recycling.

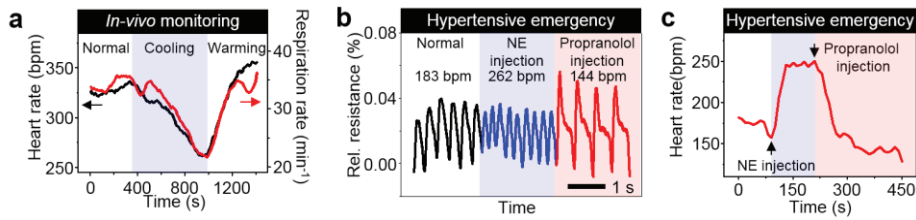


Figure 4.12. Continuous monitoring of vital signs (e.g. heartbeat and body temperature) in a mouse disease model of hypothermia induced by ethanol tap and treated with warming. (a) Change in heart rate and respiration rate at whole time range. (b, c) Continuous monitoring of heart rate in a mouse experimental model of hypertensive emergency (b), which was induced by intravenous (IV) injection of norepinephrine (NE) and was sequentially treated with IV administration of propranolol (c).

4.3.4 Control of Transdermal Drug Delivery by Iontophoresis

The integrated iontophoresis electrodes in the mSC patch control transdermal drug delivery rate.^[39] The m-SiO₂ nanoparticles (**Figure 4.13a**) were utilized as drug delivery vehicles, which prevent oxidation, denaturation, and unstimulated diffusion of drugs.^[40] Nanopores inside m-SiO₂ nanoparticles provide large surface area for drug adsorption and loading.^[41] The insets of Figure 4.13a show the confocal images of fluorescent drug (doxorubicin; red, center) loaded on m-SiO₂ carriers (green, left). The right inset shows the combined image (yellow). The system incorporates the iontophoresis approach for drug delivery, in which medications are smeared deeply under the skin by the charge repulsion between electrodes and drugs. Iontophoresis has advantages over the thermal diffusion in preventing low-temperature-burn-injury and/or thermal denaturation of drugs.

The amount of drug delivery is controlled by stimulus number of iontophoresis and thermal diffusion; 1 minute stimulus and 3 minutes break was defined as one cycle of external stimulus. As shown in Figure 4.13b, diffusion depth of the doxorubicin into Balb/c mouse skin is proportional to the number of applied stimulus. The drug penetration depth by iontophoresis is ~200 μm, which is the depth of epidermis and upper dermis, within 12 stimuli. The depth by thermal diffusion (at ~37 °C; ~12°C higher than the normal body temperature

of mouse) is much shallower ($\sim 35 \mu\text{m}$). Drug diffusion without external stimuli (control) is negligible. The confocal microscope images (red: doxorubicin) show the difference of drug diffusion depths into mouse skin at different cycles of iontophoresis (Figure 4.13c left and right for 3 and 12 cycles, respectively).

Another benefit of the mSC dry adhesives is that pharmacological agents are easily reloaded by using temporary substrates and cleaning agents.

(**Figure 4.14**) show sequential confocal microscope images of the iontophoresis electrode after loading drug (red: doxorubicin), washing the electrode after use, and reloading different dye (green: 9,10-diphenylanthracene (DPA)), respectively. These two are sequentially delivered to the mouse skin by iontophoresis stimuli (Figure 4.13d). The stimulus number of doxorubicin was doubled over that of DPA and thereby doxorubicin diffusion depth is twice of DPA.

Therapeutic effects using the mSC electronic patch are demonstrated by *in-vivo* animal experiments. The lipopolysaccharide (LPS), bacterial endotoxin, initiates inflammatory responses, inducing reactive oxygen species and various inflammatory cytokines. Drug-loaded mSC patch was laminated on the LPS-injected mouse skin and 12 cycles of iontophoresis were applied for anti-inflammatory agent (dexamethasone) diffusion. To verify the therapeutic effect, histopathological (H&E staining; Figure 4.13e), immunofluorescence

(Figure 4.13f), and western blot (Figure 4.13 g and h) analysis were employed.

As shown in Figure 4.13f, The immunofluorescence stainings of skin tissues show that the treatment of dexamethasone significantly suppresses expressions of inflammatory mediators, interleukin-1 β (IL-1 β , green) and inducible nitric oxide synthase (iNOS, red), compared with LPS-injected bare skin. The western blot data also demonstrates the reduced expression levels of IL-1 β (Figure 4.13g) and iNOS (Figure 4.13h) by the dexamethasone treatment, confirming transdermal penetration through iontophoresis.

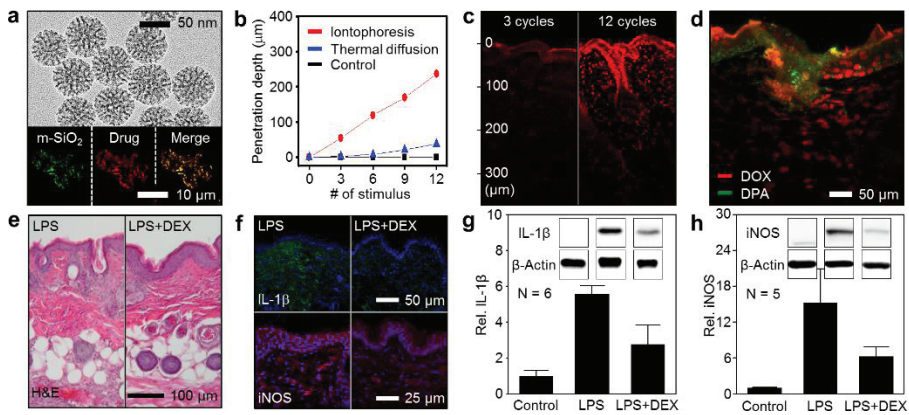


Figure 4.13. Controlled transdermal drug delivery via iontophoresis. **(a)** TEM image of drug loaded mesoporous silica nanoparticles (m-SiO₂). The inset shows unified confocal image of m-SiO₂ (green) and fluorescent drug (doxorubicin, red). **(b)** Stimulus number versus drug diffusion length into the mouse skin with different actuators (black: none, blue: thermal actuator, and red: iontophoresis electrode). **(c)** Cross-sectional fluorescence images for the drug (doxorubicin) diffusion into the mouse skin with different stimuli of iontophoresis; 3 cycles (left) and 12 cycles (right). **(d)** The cross-sectional confocal fluorescence image which demonstrates the sequentially diffused two different dyes into the mouse skin (red: doxorubicin, green: 9,10-diphenylanthracene). **(e)** The Hematoxylin and eosin (H&E) stain histology of the lipopolysaccharide (LPS)-injected mouse skins before (left) and after (right) dexamethasone (DEX) treatment. **(f)** Immunohistochemistry of interleukin-1β (IL-1β, green) and inducible nitric oxide synthase (iNOS, red) before (left) and after (right) DEX treatment. Nuclei are marked with 4',6-diamidino-2-phenylindole (DAPI, blue). **(g, h)** Western blot immunoassay of IL-1β (g) and iNOS (h). The insets show the representative band intensity due in the expressed inflammatory mediators.

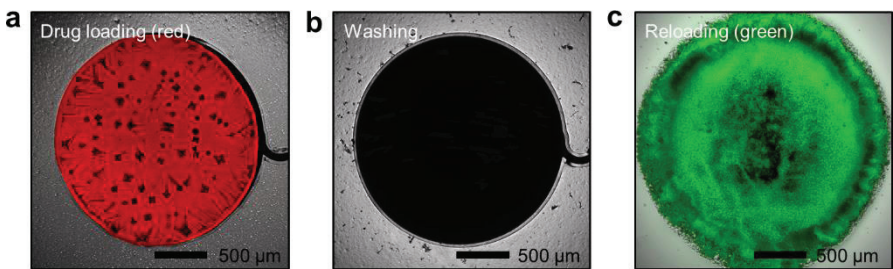


Figure 4.14. Drug reloading procedure onto the electrode of the mSC patch.

(a-c) The confocal images show that two different dyes (red: doxorubicin (a), green: DPA (c)) are successively loaded on the clean, reused electrode (b).

4.4 Conclusion

In conclusion, we developed cephalopod-inspired dry adhesives integrated with physiological sensors, drug-delivery actuators, and therapeutic nanoparticles in an ultrathin and stretchable format. The biomimetic structures enhance adhesion and comfort, limit tissue damage and inflammations, and allow sensitive biometric measurement and transdermal drug delivery by virtue of tight skin coupling. Wireless connection of the electronic patch through a Bluetooth-enabled band allows data transmission in real time and provides a path for remote diagnostics and treatments, forwards bio-inspired “smart medical skin”.

*** The contents of this chapter were published in Advanced Healthcare Materials (2016, 5, 80).**

References

- [1] K. Autumn, Y. A. Liang, S. T. Hsieh, W. Zesch, W. P. Chan, T. W. Kenny, R. Fearing, R. J. Full, *Nature* **2000**, 405, 681.
- [2] N. Huebsch, D. J. Mooney, *Nature* **2009**, 462, 426.
- [3] A. Mahdavi, L. Ferreira, C. Sundback, J. W. Nichol, E. P. Chan, D. J. D. Carter, C. J. Bettinger, S. Patanavanich, L. Chignozha, E. Ben-Joseph, A. Galakatos, H. Pryor, I. Pomerantseva, P. T. Masiakos, W. Faquin, A. Zumbuehl, S. Hong, J. Borenstein, J. Vacanti, R. Langer, J. M. Karp, *Proc. Natl. Acad. Sci. USA* **2008**, 105, 2307.
- [4] J.-Y. Sun, X. Zhao, W. R. K. Illeperuma, O. Chaudhuri, K. H. Oh, D. J. Mooney, J. J. Vlassak, Z. Suo, *Nature* **2012**, 489, 133.
- [5] S. Y. Yang, E. D. O'Cearbhail, G. C. Sisk, K. M. Park, W. K. Cho, M. Villiger, B. E. Bouma, B. Pomahac, J. M. Karp, *Nat. Commun.* **2013**, 4, 1702.
- [6] A. K. Geim, S. V. Dubonos, I. V. Grigorieva, K. S. Novoselov, A. A. Zhukov, S. Y. Shapoval, *Nat. Mater.* **2003**, 2, 461.
- [7] T.-i. Kim, H. E. Jeong, K. Y. Suh, H. H. Lee, *Adv. Mater.* **2009**, 21, 2276.
- [8] H. E. Jeong, J.-K. Lee, H. N. Kim, S. H. Moon, K. Y. Suh, *Proc. Natl. Acad. Sci. USA* **2009**, 106, 5644.
- [9] H. Yoon, H. E. Jeong, T.-i. Kim, T. J. Kang, D. Tahk, K. Char, K. Y. Suh,

Nano Today **2009**, 4, 385.

- [10] H. Lee, B. P. Lee, P. B. Messersmith, *Nature* **2007**, 448, 338.
- [11] D.-H. Kim, J. Viventi, J. J. Amsden, J. Xiao, L. Vigeland, Y.-S. Kim, J. A. Blanco, B. Panilaitis, E. S. Frechette, D. Contreras, D. L. Kaplan, F. G. Omenetto, Y. G. Huang, K.-C. Hwang, M. R. Zakin, B. Litt, J. A. Rogers, *Nat. Mater.* **2010**, 9, 511.
- [12] M. Kaltenbrunner, T. Sekitani, J. Reeder, T. Yokota, K. Kuribara, T. Tokuhara, M. Drack, R. Schwodiauer, I. Graz, S. Bauer-Gogonea, S. Bauer, T. Someya, *Nature* **2013**, 499, 458.
- [13] D.-H. Kim, N. Lu, R. Ma, Y.-S. Kim, R.-H. Kim, S. Wang, J. Wu, S. M. Won, H. Tao, A. Islam, K. J. Yu, T.-i. Kim, R. Chowdhury, M. Ying, L. Xu, M. Li, H.-J. Chung, H. Keum, M. McCormick, P. Liu, Y.-W. Zhang, F. G. Omenetto, Y. Huang, T. Coleman, J. A. Rogers, *Science* **2011**, 333, 838.
- [14] S. Lee, Y. Inoue, D. Kim, A. Reuveny, K. Kuribara, T. Yokota, J. Reeder, M. Sekino, T. Sekitani, Y. Abe, T. Someya, *Nat. Commun.* **2014**, 5, 5898.
- [15] C. Keplinger, J.-Y. Sun, C. C. Foo, P. Rothemund, G. M. Whitesides, Z. Suo, *Science* **2013**, 341, 984.
- [16] J. Kim, M. Lee, H. J. Shim, R. Ghaffari, H. R. Cho, D. Son, Y. H. Jung, M. Soh, C. Choi, S. Jung, K. Chu, D. Jeon, S.-T. Lee, J. H. Kim, S. H.

- Choi, T. Hyeon, D.-H. Kim, *Nat. Commun.* **2014**, 5, 5747.
- [17] S. Jung, J. H. Kim, J. Kim, S. Choi, J. Lee, I. Park, T. Hyeon, D.-H. Kim, *Adv. Mater.* **2014**, 26, 4825.
- [18] S. Jung, J. Lee, T. Hyeon, M. Lee, D.-H. Kim, *Adv. Mater.* **2014**, 26, 6329.
- [19] S. Lim, D. Son, J. Kim, Y. B. Lee, J.-K. Song, S. Choi, D. J. Lee, J. H. Kim, M. Lee, T. Hyeon, D.-H. Kim, *Adv. Funct. Mater.* **2015**, 25, 375.
- [20] M. Park, K. Do, J. Kim, D. Son, J. H. Koo, J. Park, J.-K. Song, J. H. Kim, M. Lee, T. Hyeon, and D.-H. Kim, *Adv. Healthcare Mater.* **2015**, 4, 992.
- [21] K. Takei, T. Takahashi, J. C. Ho, H. Ko, A. G. Gillies, P. W. Leu, R. S. Fearing, A. Javey, *Nat. Mater.* **2010**, 9, 821.
- [22] D. J. Lipomi, M. Vosgueritchian, B. C. K. Tee, S. L. Hellstrom, J. A. Lee, C. H. Fox, Z. Bao, *Nat. Nanotechnol.* **2011**, 6, 788.
- [23] D. Son, J. Lee, S. Qiao, R. Ghaffari, J. Kim, J. E. Lee, C. Song, S. J. Kim, D. J. Lee, S. W. Jun, S. Yang, M. Park, J. Shin, K. Do, M. Lee, K. Kang, C. S. Hwang, N. Lu, T. Hyeon, D.-H. Kim, *Nat. Nanotechnol.* **2014**, 9, 397.
- [24] W.-Y. Chang, Y. Wu, Y.-C. Chung, *Nano Lett.* **2014**, 14, 1546.
- [25] J. D. Eshelby, *Proc. R. Soc. A* **1957**, 241, 376.
- [26] R. H. LaMotte, S. G. Shimada, P. Sikand, *Exp. Dermatol.* **2011**, 20, 778.
- [27] S. G. Shimada, R. H. LaMotte, *Pain* **2008**, 139, 681.

- [28] W. C. M. Cramer, G. P. Toorop, *Gen. Pharmacol.* **1998**, 30, 195.
- [29] J. Polio, C. C. Sieber, E. Lerner, R. J. Groszmann, *Hepatology* **1993**, 18, 128.
- [30] M. H. Todd, J. B. Forrest, D. B. J. Cragg, *Am. Heart J.* **1983**, 105, 769.
- [31] L. Pan, Q. He, J. Liu, Y. Chen, M. Ma, L. Zhang, J. Shi, *J. Am. Chem. Soc.* **2012**, 134, 5722.
- [32] W. G. Bae, D. Kim, M. K. Kwak, L. Ha, S. M. Kang, K. Y. Suh, *Adv. Healthcare Mater.* **2013**, 2, 109.
- [33] J. D. Eshelby, *Proc. R. Soc. A* **1957**, 241, 376.
- [34] M. K. Kwak, H.-E. Jeong, K. Y. Suh, *Adv. Mater.* **2011**, 23, 3949.
- [35] K.-I. Jang, S. Y. Han, S. Xu, K. E. Mathewson, Y. Zhang, J.-W. Jeong, G.-T. Kim, R. C. Webb, J. W. Lee, T. J. Dawidczyk, R. H. Kim, Y. M. Song, W.-H. Yeo, S. Kim, H. Cheng, S. I. Rhee, J. Chung, B. Kim, H. U. Chung, D. Lee, Y. Yang, M. Cho, J. G. Gaspar, R. Carbonari, M. Fabiani, G. Gratton, Y. Huang, J. A. Rogers, *Nat. Commun.* **2014**, 5, 4779.
- [36] L. Y. Chen, B. C. K. Tee, A. L. Chortos, G. Schwartz, V. Tse, D. J. Lipomi, H.-S. P. Wong, M. V. McConnell, Z. Bao, *Nat. Commun.* **2014**, 5, 5028.
- [37] S. Laurent, J. Cockcroft, L. Van Bortel, P. Boutouyrie, C. Giannattasio, D. Hayoz, B. Pannier, C. Vlachopoulos, I. Wilkinson, H. Struijker-Boudier, *Eur. Heart. J.* **2006**, 27, 2588.

- [38] C. Pang, J. H. Koo, A. Nguyen, J. M. Caves, M.-G. Kim, A. Chortos, K. Kim, P. J. Wang, J. B.-H. Tok, Z. Bao, *Adv. Mater.* **2015**, 27, 634.
- [39] M. R. Prausnitz, R. Langer, *Nat. Biotechnol.* **2008**, 26, 1261.
- [40] J. E. Lee, N. Lee, T. Kim, J. Kim, T. Hyeon, *Accounts Chem. Res.* **2011**, 44, 893.
- [41] Y. Gao, Y. Chen, X. Ji, X. He, Q. Yin, Z. Zhang, J. Shi, Y. Li, *ACS Nano* **2011**, 5, 9788.

Bibliography

1. International Publications

- 1) **M. K. Choi**, J. Yang, K. Kang, D. C. Kim, C. Choi, C. Park, S. J. Kim, S. I. Chae, T.-H. Kim, J. H. Kim, T. Hyeon, D.-H. Kim, “Wearable Red-Green-Blue Quantum Dot Light-Emitting Diode Array using High-Resolution Intaglio Transfer Printing”, *Nature Commun.* **6**, 7149 (2015).
- 2) **M. K. Choi**, I. Park, D. C. Kim, E. Joh, O. K. Park, J. Kim, M. Kim, C. Choi, J. Yang, K. W. Cho, J.-H. Hwang, J.-M. Nam, T. Hyeon, J. H. Kim, D.-H. Kim, “Thermally Controlled, Patterned Graphene Transfer Printing for Transparent and Wearable Electronic/Opto electronic System”, *Adv. Funct. Mater.* **25**, 7109 (2015). (Cover Article).
- 3) **M. K. Choi**, O. K. Park, C. Choi, S. Qiao, R. Ghaffari, J. Kim, D. J. Lee, M. Kim, W. Hyun, S. J. Kim, H. J. Hwang, S.-H. Kwon, T. Hyeon, N. Lu, D.-H. Kim, “Cephalopod-Inspired Miniaturized Suction Cups for Smart Medical Skin” *Adv. Healthc. Mater.* **5**, 80 (2016). (**Cover Article**)

- 4) J. Yang*, M. K. Choi*, D.-H. Kim, T. Hyeon, “Designed Assembly and Integration of Colloidal Nanocrystals for Device Applications”, *Adv. Mater.* **28**, 1176 (2016). (***Equal Contributions**)
- 5) C. Choi,* M. K. Choi*, C. Choi, T. Hyeon, D.-H. Kim, “Nanomaterials-based Soft Electronics for Wearable and Implantable Healthcare Devices”, *Chem. Nano. Mater. Submitted. (*Equal Contributions)*
- 6) J. Kim, J. Lee, D. Son, M. K. Choi, D.-H. Kim, “Deformable Devices with Integrated Functional Nanomaterials for Wearable Electronics”, *Nano Convergence* **3**, 4 (2016).
- 7) J. Yang, R. Fainblat, S. G. Kwon, F. Muckel, J. H. Yu, H. Terlinden, B. H. Kim, D. Iavarone, M. K. Choi, I. Y. Kim, I. Park, H.-K. Hong, J. Lee, J. S. Son, Z. Lee, K. Kang, S.-J. Hwang, G. Bacher, T. Hyeon, “Route to the Smallest Doped Semiconductor: Mn²⁺-Doped (CdSe) 13 Clusters” *J. Am. Chem. Soc.* **137**, 12776-12779 (2015).
- 8) S. J. Kim, H. R. Cho, K. W. Cho, S. Qiao, J. S. Rhim, M. Soh, T. Kim, M. K. Choi, C. Choi, I. Park, N. S. Hwang, T. Hyeon, S. H. Choi, N. Lu, D.-

H. Kim, “Multifunctional Cell-Culture Platform for Aligned Cell Sheet Monitoring, Transfer Printing, and Therapy”, *ACS Nano* **9**, 2677-2688 (2015).

- 9) J. H. Yu, S.-H. Kwon, Z. Petrášek, O. K. Park, S. W. Jun, K. Shin, M. K. Choi, Y. I. Park, K. Park, H. B. Na, N. Lee, D. W. Lee, J. H. Kim, P. Schwille, T. Hyeon, “High-resolution three-photon biomedical imaging using doped ZnS nanocrystals”, *Nature Mater.* **12**, 359-366 (2013).
- 10) J. S. Son, K. Park, S. G. Kwon, J. Yang, M. K. Choi, J. Kim, J. H. Yu, J. Joo, T. Hyeon, “Dimension-Controlled Synthesis of CdS Nanocrystals: From 0D Quantum Dots to 2D Nanoplates”, *Small* **8**, 2394-2402 (2012).
- 11) J. S. Son, M. K. Choi, M.-K. Han, K. Park, J.-Y. Kim, S. J. Lim, M. Oh, Y. Kuk, C. Park, S.-J. Kim, T. Hyeon, “n-Type nanostructured thermoelectric materials prepared from chemically synthesized ultrathin Bi₂Te₃ nanoplates”, *Nano Lett.* **12**, 640-647 (2012).
- 12) M. K. Choi, J.-H. Kim, H. Yoon, D. Tahk, S. Seo, K. Shin, H. H Lee, “Efficiency Improvement of Organic Solar Cells by Tuning Hole Transport

Layer with Germanium Oxide”, *J. Nanosci. Nanotech.* **12**, 623-628 (2012).

13) **M. K. Choi**, H. Yoon, K. Lee, K. Shin, “Simple fabrication of asymmetric high-aspect-ratio polymer nanopillars by reusable AAO templates”,

Langmuir **27**, 2132-2137 (2011).

14) S.-J. Choi, **M. K. Choi**, D. Tahk, H. Yoon, “Fabrication of a hierarchical structure by oxygen plasma etching of a photocured microstructure containing a silicon moiety”, *J. Mater. Chem.* **21**, 14936-14940 (2011).

15) H. Yoon, **M. K. Choi**, K. Y. Suh, K. Char, “Self-modulating polymer resist patterns in pressure-assisted capillary force lithography”, *J. Colloid. Interface. Sci.* **346**, 476-482 (2010).

16) H. Yoon, H. Woo, **M. K. Choi**, K. Y. Suh, K. Char, “Face selection in one-step bending of janus nanopillars”, *Langmuir* **26**, 9198-9201 (2010).

17) D. Tahk, T.-i. Kim, H. Yoon, **M. K. Choi**, K. Shin, K. Y. Suh, “Fabrication of antireflection and antifogging polymer sheet by partial photopolymerization and dry etching”, *Langmuir* **26**, 2240-2243 (2010).

2. International Conferences

- 1) **Moon Kee Choi** and Dae-Hyeong Kim, “Flexible and stretchable electronics for mapping and therapy in cardiac electrophysiology” *2012 MRS Fall Meeting*, Boston, 2012.
- 2) Dae-Hyeong Kim (Invited talk, presented on behalf of Dae-Hyeong Kim by **Moon Kee Choi**), “Flexible and stretchable electronics and applications for biomedical devices” *ENGE 2012*, Jeju Island, Korea, 2012.
- 3) **Moon Kee Choi** and Dae-Hyeong Kim, “High resolution, wearable quantum dot LEDs using intaglio transfer printing technique” *IUPAC-2015 (poster)*, Busan, Korea, Aug. 7-13, 2015.
- 4) **Moon Kee Choi** and Dae-Hyeong Kim, “Wearable high-resolution quantum dot LED array using intaglio transfer printing.” *The 9th International Conference on Advanced Materials and Devices (poster)*, Jeju Island, Korea, Dec. 7-9, 2015.
- 5) **Moon Kee Choi** and Dae-Hyeong Kim, “Wearable high resolution

quantum dot LEDs using intaglio transfer printing.” *The 2016 MRS Spring Meeting*, Pheonix, U.S.A., Mar. 27- April, 26, 2016.

6) **Moon Kee Choi**, Dong Chan Kim, and Dae-Hyeong Kim, “High resolution, wearable red-green-blue quantum dot LED array using intaglio transfer printing” *The 9th International Conference on Quantum Dots*, Korea, May, 22-27, 2016.

7) **Moon Kee Choi** and Dae-Hyeong Kim, “High resolution, wearable quantum dot LEDs using intaglio transfer printing”, *The 20th International Vacuum Congress*, Busan, Korea, Aug. 21-26, 2016.

3. Domestic Conference

1) **Moon Kee Choi** and Dae-Hyeong Kim, “Noble intaglio transfer printing for high resolution ultrathin, wearable quantum dot LED array” *The 2015 Korean Institute of Chemical Engineers Fall Meeting*, Ilsan, Korea, 2016.

2) **Moon Kee Choi** and Dae-Hyeong Kim, “Graphene based transparent, wearable softbioelectronics using thermally controlled transfer printing technique” *The 2016 Korean Institute of Chemical Engineers Spring*

Meeting, Busan, Korea, Apr. 27-29, 2016.

4. Awards

1) 2014 KBSI Exhibition Prize for Bioimaging

Korea Basic Science Institute, Dec. 22, 2014

2) Outstanding Research Award – Best oral presentation

The Korean Institute of Chemical Engineers, Korea, Apr. 27-29, 2016

3) QD 2016 JACS Awards

The 9th International Conference on Quantum Dots, Korea, May, 22-27, 2016.

4) Outstanding Research Award

Dongjin Semichem & Chemical and Biological Engineering, Seoul National University, Korea, Jun. 17, 2016.

요 약 (국 문 초 록)

웨어러블 발광소자와 바이오 센서를 위한 새로운 소프트리소그래피 기술

최근 헬스케어 관련 웨어러블 전자/광전자 소자들에 대한 관심이 많아지고 있다. 기존의 딱딱한 기판에서 벗어나 휘어지고 늘어날 수 있는 소자를 만들기 위해 다양한 나노물질들을 접목시켜 성능을 향상시키고자 하는 연구들이 진행되고 있다. 본 논문에서는 다양한 전자소자들이 접적된 웨어러블 소자에 나노물질들을 원하는 곳에 접적하기 위해 전극, 활성물질, 패치 등 요소별 맞춤형 소프트리소그래피 기법들을 다루고 이를 웨어러블 발광소자와 바이오센서 시스템에 적용하였다.

첫째로, 피부에 붙일 수 있는 고해상도 디스플레이를 구현하기 위해 양자점 나노입자들을 정확한 위치에 패턴 크기 변화 없이 정렬할 수 있는 음각 인쇄 기술을 개발하였다. 이를 이용하여 수 마이크로의 해상도를 갖는 삼원색 픽셀 기반의 초박막 광학소자를 만들고, 고성능의 백색광 다이오드와 초박막 웨어러블 양자점 디스플레이를 최초로 구현하였다.

둘째로, 고온-저온 열처리 방식을 통해 투명 소자의 재료로

각광받고 있는 그래핀의 패턴 전사기법과 그를 이용한 투명 소자 시스템을 소개한다. 본 논문에서 소개하는 그래핀 기반 전자소자 시스템은 열처리 전사 기법을 통해 전극, 체온을 모니터링 하는 센서, 약물전달을 위한 히터와 국소 약물 주입이 가능한 나노입자를 담지한 이온주입 전극 등을 모두 그래핀을 사용하여 투명 전자소자를 구현한다. 이는 향후 심미성을 높여줄 수 있는 차세대 투명 전자소자 시스템을 제시한다.

마지막으로 피부 부착형 전자소자들이 외부 자극이나 마찰에 의해 떨어지지 않도록 패치에 나노패턴을 부가하여 강한 접착력을 가지면서 피부에 자극이 없고 재사용이 가능한 전자패치를 소개한다. 높은 접착력 덕분에 장기간 생체신호를 정밀하게 진단할 수 있으며 스마트밴드와 연계하여 실시간으로 데이터를 전송하여 피드백 치료가 가능하게 하는 접적 시스템 기술을 제시하였다.

주요어: 비전통적 패터닝, 입을 수 있는 전자소자, 늘릴 수 있는 전자소자, 양자점 나노입자 발광 소자, 그래핀 전자 소자, 건식 접착제, 바이오센서

학번: 2010-24105